STUDIES ON SEISMIC BEHAVIOR OF CONCRETE GRAVITY DAMS

by

WILLIAM JAMES YONEDA

B.Sc., The University of British Columbia, 2001

A THESIS SUBMITTED IN PARTIAL FULFILMENT OF
THE REQUIREMENTS FOR THE DEGREE OF

MASTER OF APPLIED SCIENCE

in

THE FACULTY OF GRADUATE STUDIES

(Civil Engineering)

THE UNIVERSITY OF BRITISH COLUMBIA

May 2005

Abstract

This Master's thesis presents three independent studies related to the safety of concrete gravity dams.

1. Dam-Gate Hydrodynamic Interaction Study
2. Damping Study
3. Shear Key Study

The three studies are self-contained, presented independently in Chapters 2 – 4 of this thesis. Work on this thesis started in winter 2002. The analytical work was completed in summer 2004. This thesis was written as part of the Professional Partnership Program with the University of British Columbia and British Columbia Hydro.

A modal analysis of a 2DOF simplified model representing a portion of an existing gravity dam structure was performed. The main purposes of this study were to evaluate the effect of dam-gate interaction on the hydrodynamic loads and to evaluate the effect of varying the natural frequency of the gate. It was found that the modal interaction between the dam and gate structures caused variation in the hydrodynamic loads acting on the gate and upstream face of the dam. One of the recommendations for retrofitting the gates is to decrease the natural frequency of the gate to below the natural frequency of the dam. This essentially increases the flexibility of the gate system and reduces the amount of hydrodynamic loads generated on the gate and upstream surface of the dam.

An analytical study to test the Half-Power Bandwidth method of estimating damping in concrete gravity dams was performed successfully. The objectives of this study were to test this method of evaluating structural damping and to recommend a reasonable estimate of structural damping in concrete gravity dams. The damping values computed by this method were found to be much lower than expected (less than 2%) and therefore, unrepresentative of the damping that is likely believed to be present in the concrete gravity dams analyzed in this study (approximately 5 – 10%).

An exploratory study involving the finite-element modeling of a shear key system was performed. The stress patterns that developed in the finite element model under applied horizontal load were similar to those exhibited in the early stages of the cracking sequence presented by Bakhoum (1991). In order to model the later stages of the cracking sequence, it would be necessary to implement non-linear material models that are capable of modeling loading beyond the linear range to failure.

Table of Contents

List of Figures

List of Tables

Acknowledgments

This thesis was completed as part of the Professional Partnership Program between the University of British Columbia and BCHydro. First, the author acknowledges Dr. Carlos E. Ventura at the UBC Department of Civil Engineering for his continuous guidance and support throughout the completion of this thesis. The author acknowledges Dr. David Dowdell at BCHydro for his technical and moral support, insight, and imagination throughout the completion of this thesis. The author acknowledges Mr. Benedict Fan at BCHydro for his leadership in the Dam Safety Division at BCHydro. The author also acknowledges all of the engineers and technical support staff at the Dam Safety Division of BCHydro for providing a pleasant and productive work environment during the two summer work terms in 2002 and 2003.

Chapter 1

Introduction

1.0 INTRODUCTION

Concrete gravity dams are a key component of hydroelectric generation systems. In areas prone to seismic activity, the structural stability of these dams is of great importance to the population at risk in potential inundation zones downstream of the structure and to the consumers of the energy generated by the system instability during or following a major earthquake could potentially lead to the discharge of the reservoir, resulting in mass flooding in the downstream area and beyond.

This thesis presents three independent studies regarding the safety of dam structures.

- Chapter 2: Dam-Gate Hydrodynamic Interaction Study
- Chapter 3: Damping Study
- Chapter 4: Shear key Study

These three studies are self-contained, each having its own objectives and scope of work, main body, conclusions and recommendations.

1.1 THE DAM SAFETY STUDIES

The three studies presented in this thesis relate to different aspects of dam safety. The Dam-Gate Hydrodynamic Interaction Study focuses on the effects of varying gate stiffness on the hydrodynamic loads generated in dam structures during earthquakes. The Damping Study focuses on the structural damping, or the ability of a structure to dissipate energy, during an earthquake. The Shear Key Study focuses on shear forces generated along the interfaces between dam monoliths during an earthquake.

The dam-gate hydrodynamic study and the shear key study were case studies applied to the Ruskin Dam. The damping study was more general but intended to provide guidance in the analysis of structures similar to Ruskin Dam.

1.1.1 Dam-Gate Hydrodynamic Interaction Study

During an earthquake, there are two primary sources of added stress to the upstream face of concrete dams:

1. Acceleration of the mass of the dam
2. Change in water pressure

The acceleration of the mass of the dam is the standard inertia load, which is generated with or without the presence of a reservoir. The change in water pressure is the driving force behind hydrodynamic loads, which are generated when an external force transfers pressure waves from a body of water to an adjacent structure. In dam structures, the hydrodynamic loads are pressures on the upstream surface of the dam; ie. the surface in direct contact with the reservoir. These loads contribute significantly to the overall set of external forces acting towards failure of the dam and discharge of the reservoir.

In current engineering practice, two methods are commonly used to estimate the hydrodynamic loads in dam structures – the Zangar method [16] and the Westergaard method [15]. In a paper by Kolkman [12], the author presents a method of formulating hydrodynamic loads by means of a finite difference matrix, by which the hydrodynamic loads are calculated based on the level of excitation along the upstream surface of the dam. In spillway dam structures, the gates are submerged and generally respond at natural frequencies different from those of the dam. According to Kolkman, this results in a different hydrodynamic load distribution along the gate structures. A study was undertaken to test the effects of this dam-gate interaction on the formulation of hydrodynamic loads.

This study is presented in Chapter 2 of this thesis, and is titled, "Dam-Gate Hydrodynamic Interaction Study". This study presents a new method of formulating the hydrodynamic loads generated on spillway gates, based on the modal interaction of the dam-gate system.

1.1.2 Damping Study

Structural damping in concrete gravity dams refers to the amount of energy the dam is capable of dissipating prior to experiencing damage. Various approaches have been taken to estimate a reasonable level of structural damping in concrete gravity dam structures. These damping values ranged from as low as 2% to as high as 20%. A study was undertaken to test the Half-Power Bandwidth Method of estimating damping in structures, given the time history response records from various concrete gravity dams in North America and Japan.

This study is entitled, “Damping Study”, and is presented in Chapter 3 of this thesis.

1.1.3 Shear Key Study

In general, concrete monolith dams consist of several monoliths aligned in a row. Shear keys are located at the interfaces between monolith blocks to prevent the blocks from displacing past one another. In a load sharing study, conducted by the author in collaboration with engineers in the Dam Safety section of BC Hydro in summer 2002, a finite element analysis of Ruskin Dam was performed to determine the amount of shear stress between dam blocks. It was found that excitation of the dam at the Design Basis Earthquake (DBE) level generated significant stresses at the interfaces between dam blocks; the maximum stresses were generated near the abutments, where the effective area of the shear keys is minimal. As such, an exploratory study was undertaken to investigate the failure mechanism of the shear keys.

This study is entitled, “Shear Key Study”, and is presented in Chapter 4 of this thesis. This study presents an investigation into the failure mechanism of shear keys and the process of modeling the shear keys using finite element software.

1.2 THE RUSKIN DAM

The primary dam considered in these studies is the Ruskin Dam, a concrete gravity dam constructed from 1929-1930 in a region of relatively high seismicity in British Columbia. The upstream face of the dam is vertical and the downstream face has approximately a 2:3 incline. The dam is approximately 58m tall and 125m wide at the crest. There are seven spillways, each housing steel radial gates approximately 10m (33ft) wide. The gates are anchored to 8 concrete piers approximately 2.1m (7ft) wide. There is reinforced concrete roadway deck spanning the crest atop the spillways.

The maximum water level of the reservoir is approximately 49m above the base; 7.9m above the ogee crest. Although the water level experiences seasonal variation, the maximum water level was selected as the worst-case scenario.

The Design Basis Earthquake (DBE) at the dam site at the time of this study has a peak ground acceleration of 0.22 g and a peak spectral acceleration of 0.54g.

Figure 1-1 shows an aerial view photograph of the downstream side of the Ruskin Dam. Figure 1-2 shows an elevation view schematic of the upstream surface. Figure 1-3 shows a typical cross section near the center of the dam.

1.3 OBJECTIVES

The main objectives of the studies presented in this thesis are:

Dam-Gate Hydrodynamic Interaction Study:

1. to evaluate the effect of dam-gate interaction on the hydrodynamic loads
2. to evaluate the effect of varying the natural frequency of the gate

Damping Study:

1. to test an analytical method of estimating damping, given ground motion time history records for two sensor locations (base and remote) on various concrete gravity dam structures
2. to use the results from these tests to recommend a reasonable estimate for damping of concrete gravity dam structures

Shear Key Study:

1. to investigate the process of modeling and testing the shear keys using the LS-DYNA finite element software [S1]
2. to identify the load path, stress concentrations, and failure patterns in the shear keys under monotonic, cyclic, and seismic loading.

1.4 SCOPE OF WORK

In order to achieve the abovementioned goals, the following tasks were carried out:

Dam-Gate Hydrodynamic Interaction Study:

1. two classical methods of formulating hydrodynamic loads on dam structures (Westergaard, Zangar) were reviewed to provide a basis for comparison.
2. a procedure based on the Kolkman Method, which incorporates dam-gate interaction was used to formulate hydrodynamic loads.
3. a case study of Ruskin Dam was performed. This involved creating a simplified 2-degree-of-freedom model, which was used to perform a modal

analysis by which the hydrodynamic loads were calculated.

Damping Study:

1. An extensive numerical analysis was performed on time history records from the dams listed in Section 3.1 to produce Frequency Response Function plots.
2. The Half-Power Bandwidth Method was used to approximate the structural damping at each peak in the FRF plots.

Shear Key Study:

1. The LS-DYNA software program [S1] was used to generate a series of finite element models.
2. A sensitivity analysis was performed to refine the shear key model, testing various parameters including geometry, contact elements, and material models.
3. The finite element models were subjected to monotonic loading in order to identify the load path, stress concentrations, and failure patterns in the shear keys.

FIGURE 1-1: Ruskin Dam

FIGURE 1-2: Ruskin Dam: Upstream View

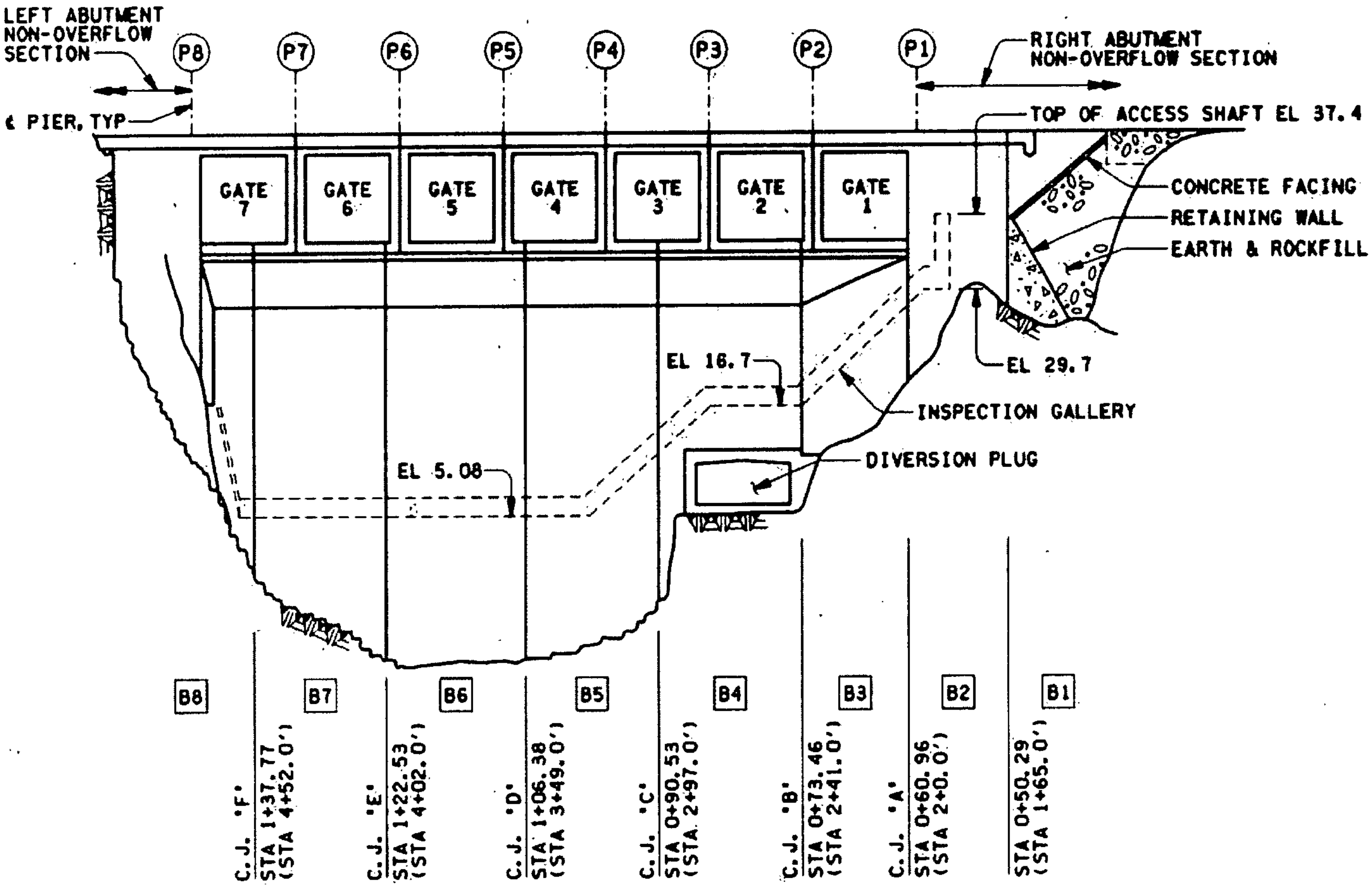

FIGURE 1-3: Ruskin Dam: Cross Section

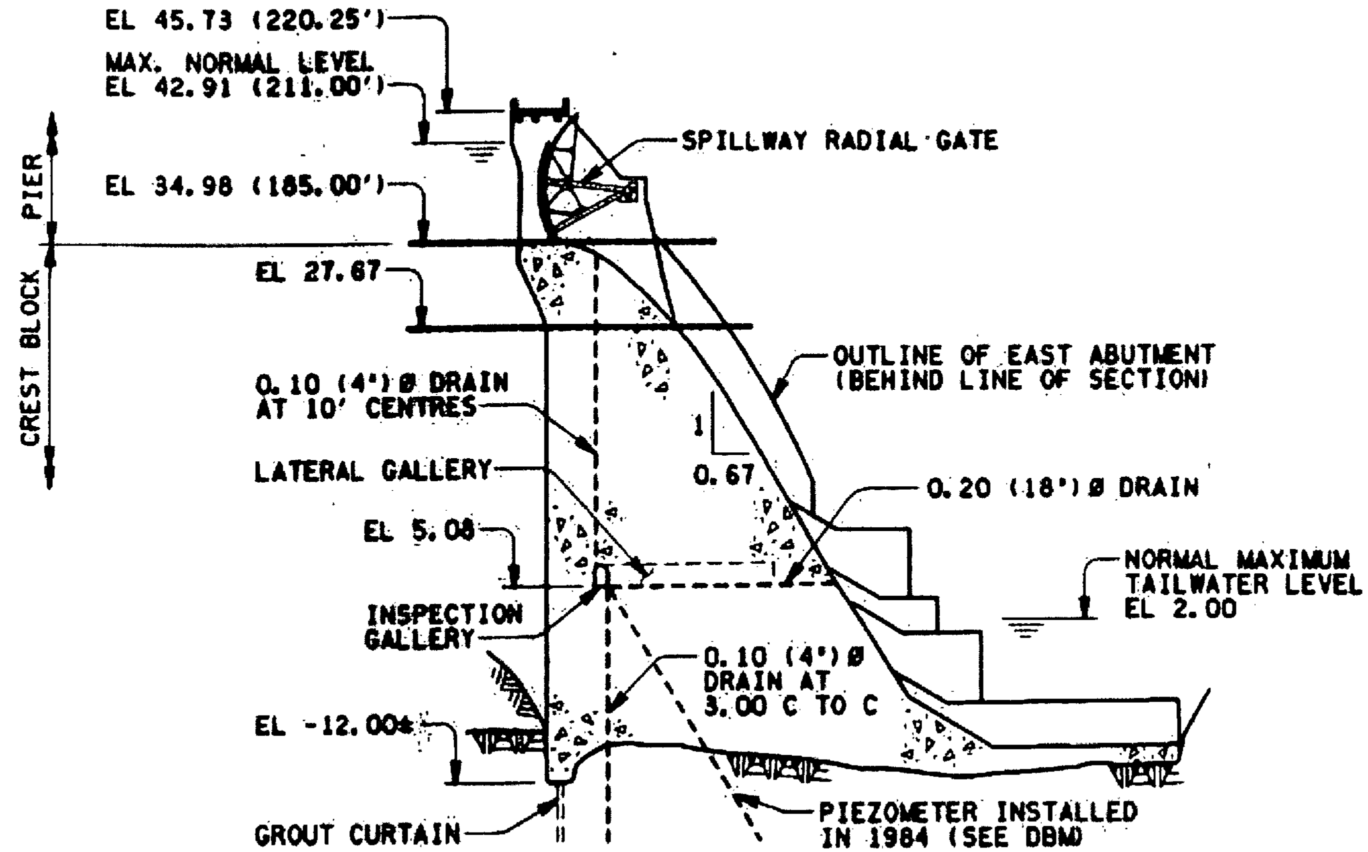

Chapter 2

Dam-Gate Hydrodynamic Interaction Study

2.0 INTRODUCTION

There are two primary sources of added stress to the upstream face of concrete dams during an earthquake:

1. Acceleration of the mass of the dam
2. Changes in water pressure

Hydrodynamic loads are forces induced on a structure at an interface with a body of water, when an external force forces the structure to oscillate against the inertial force of the water body. In dam structures, the hydrodynamic pressures act predominantly on the upstream surface of the dam; ie. the surface in direct contact with the reservoir. These loads contribute significantly to the overall set of external forces acting on dam structures. On structures such as gates, hydrodynamic loads may dominate the seismic loading.

In the current state of practice, hydrodynamic loads on dam structures are usually calculated using one of two general methods: one presented by Westergaard [15]; the other by Zangar [16]. However, both of these methods approximate hydrodynamic loads for the "rigid body" case, and do not take into account the flexibility of the structure. In a paper by P.A. Kolkman [12] entitled, "A Simple Scheme for Calculating the Added Mass of Hydraulic Gates", the author presents a simple spreadsheet solution to the hydrodynamic loads on a flexible body. Similar to Westergaard and Zangar, this method is based on an incompressible fluid subjected to vibrations.

Using the Kolkman method as a basis for calculating hydrodynamic pressures, the study aims to evaluate the contribution of flexible spillway gates to the load experienced by the gates and the structure. In a case study of Ruskin Dam, a simplified two degree-of-freedom model was used to analyze this dam-gate interaction and to obtain hydrodynamic pressures for the entire upstream face of the dam.

2.1 BACKGROUND INFORMATION

Including the method presented by Kolkman, there were three methods considered for the calculation of hydrodynamic loads on dam structures:

1. The Zangar Method
2. The Westergaard Method
3. The Kolkman Method

2.1.1 The Westergaard Method

In the paper by Westergaard titled, "Water Pressures on Dams During Earthquakes" [15], the author presents two methods for calculating hydrodynamic pressures on the vertical upstream surfaces of concrete dams. The first formula, which consists of a series of sine functions, solves the differential equation for unit rigid body acceleration of a rigid dam structure with a vertical dam-reservoir interface. The second is a parabolic simplification of the first formula.

The Westergaard formulation of hydrodynamic loads begins with the equations of motion of water. These equations are based on the theory of elasticity of solids without shear stresses for elements of volume $dxdydz$. For the formulations outlined below, x is the motion in the upstream-downstream direction, y is the motion in the vertical direction, and z is the motion in the cross-valley (parallel to dam surface) direction.

Since the formulation assumes planar motions parallel to the xy plane, the calculations relating the dz dimension are neglected. Starting with the basic finite-element equations of 2-D motion of the solid described above:

$$\frac{\partial \sigma}{\partial x} = \frac{w}{g}\frac{\partial^2 \xi}{\partial t^2} \qquad (2-1a)$$

$$\frac{\partial \sigma}{\partial y} = \frac{w}{g}\frac{\partial^2 \eta}{\partial t^2} \qquad (2-1b)$$

Where ξ and η are the displacements of a particle of the water element in the x and y directions, respectively, and σ is the stress induced in the water by the dynamic response. The resulting volumetric strain, ε, and stress, σ, are given by:

$$\varepsilon = \frac{\partial \xi}{\partial x} + \frac{\partial \eta}{\partial y} \qquad (2-2a)$$

$$\sigma = k\left(\frac{\partial \xi}{\partial x} + \frac{\partial \eta}{\partial y}\right) \qquad (2-2b)$$

Where k is the bulk modulus of water. These equations hold true for relatively small vibratory motions induced by earthquake ground motion. For the case of both horizontal and vertical motions acting on the water, a solution is desired that satisfies the above equations and the following boundary conditions.

$$\sigma = 0, \text{ when } y = 0$$
$$\eta = 0, \text{ when } y = h$$
$$\xi = -\frac{\alpha g T^2}{4\pi^2}\cos\frac{2\pi t}{T}, \text{ when } x = 0$$
$$\lim_{x\to\infty} \sigma = 0$$

Westergaard presents the following solution for ξ and η, given the criteria above and assuming the dam has a simple harmonic response to the earthquake with period T and magnitude of acceleration αg:

$$\xi = -\frac{\alpha g T^2}{\pi^2} \cos\frac{2\pi t}{T} \sum_{1,3,5\ldots}^{n} \frac{1}{n} e^{-q_n} \sin\frac{n\pi y}{2h} \qquad (2-3a)$$

$$\eta = -\frac{\alpha g T^2}{\pi^2} \cos\frac{2\pi t}{T} \sum_{1,3,5\ldots}^{n} \frac{1}{n c_n} e^{-q_n} \cos\frac{n\pi y}{2h} \qquad (2-3b)$$

Where:

$$c_n = \sqrt{1 - \frac{16 w h^2}{n^2 g k T^2}}$$

$$q_n = \frac{n\pi c_n x}{2h}$$

The resulting solution for the stress in the water, σ, is given by:

$$\sigma = -\frac{8\alpha w h}{\pi^2} \cos\frac{2\pi t}{T} \sum_{1,3,5\ldots}^{n} \frac{1}{n^2 c_n} e^{-q_n} \sin\frac{n\pi y}{2h} \qquad (2-4)$$

The hydrodynamic pressures, p, are derived from the stress equation for the times of peak response, $t = 0, T, 2T, \ldots$

$$p = \frac{8\alpha w h}{\pi^2} \sum_{1,3,5\ldots}^{n} \frac{1}{n^2 c_n} \sin\frac{n\pi y}{2h} \qquad (2-5)$$

By inspection the maximum pressure, p_0, occurs at the bottom of the reservoir, where $y = h$.

$$p_0 = \frac{8\alpha wh}{\pi^2} \sum_{1,3,5\ldots}^{n} \frac{-(1)^{\frac{n-1}{2}}}{n^2 c_n} \qquad (2-6)$$

Since this formula is dependent on there being a simple harmonic excitation of period, T, Westergaard presented a simpler formula for the hydrodynamic pressure distribution based on the shape of the first equation. This formula represents the hydrodynamic load as an added mass that is subjected to the earthquake acceleration.

$$p = C\alpha\sqrt{hy} \qquad (2-7)$$

Where C is a variable that remains fairly constant around the 0.027 ton/ft^2 range. Westergaard calculated C as 0.026 ton/ft^2 for dams of height less than 310 ft and 0.028 ton/ft^2 for dams of height greater than 540 ft. Given this, the thickness of the body of water considered to move with the dam during the earthquake, b, is given by the following formula:

$$b = \frac{7}{8}\sqrt{hy} \qquad (2-8)$$

This formula can be used to calculate an approximate distribution of hydrodynamic added masses along the height of the dam, y, given the total height of the water level, h.

2.1.2 The Zangar Method

In the paper by Zangar titled, "Hydrodynamic Pressures on Dams Due to Horizontal Earthquake Effects" [16], the author presents a method for calculating hydrodynamic pressures on dam structures with upstream surfaces of varying slope. The hydrodynamic pressures for a dam structure with a vertical upstream surface is evaluated by the following equation:

$$P(y) = hawC \qquad (2-9)$$

Where h is the vertical distance from the water level to the dam base, a is the peak ground acceleration in g's, and w is the density of water $\left(62.4 lb/ft^3\right)$. The Zangar coefficient, C, is given by the following equation:

$$C = \left(\frac{C_m}{2}\right)\left[\left(\frac{y}{h}\right)\left(2-\left(\frac{y}{h}\right)\right)+\sqrt{\left(\frac{y}{h}\right)\left(2-\left(\frac{y}{h}\right)\right)}\right] \qquad (2-10)$$

Where y is the vertical distance from the water level to the location on the dam surface and the shape constant $C_m = 0.735$ for a vertical upstream dam surface.

It is common practice to use the Zangar added masses in a dynamic analysis resulting in hydrodynamic pressures that are similar to those determined by scaling the Zangar hydrodynamic pressures by amplification factors. The amplification factors relate the peak acceleration of a point on the surface of the dam structure to the free-field peak ground acceleration. By combining formulae 2-9 and 2-10, an approximate distribution of hydrodynamic added masses along the height of the dam, y, can be calculated, given the total height of the water level, h.

2.1.3 The Kolkman Method

The method presented by Kolkman [12] is simple because it employs an iterative relaxation method to solve the differential equation for the potential function of the vibration of a fluid. Simplified formulas result by using a square grid of finite difference points. The intended use of the Kolkman method is to calculate added masses based on the division of the calculated pressures by the accelerations of the moving boundary; in this case, this boundary is the dam-reservoir interface. However, since it is desired to determine the hydrodynamic pressures rather than added masses, the Kolkman method was slightly modified to achieve these results.

The Kolkman procedure is as follows:

1. Establish a grid with square elements (20 x 28 = 51m x 71m)

2. Create a spreadsheet with a grid of cells containing the value of the fluid potential, Φ. Input formulae as per Kolkman in each cell to calculate the fluid potential according to the values contained in neighboring cells.

Interior Cells:

$$\Phi(i,j) = \left(\Phi(i+1,j) + \Phi(i-1,j) + \Phi(i,j+1) + \Phi(i,j-1)\right)/4 \qquad (2-11a)$$

Dam Interface:

$$\Phi(1,j) = (\Phi(1,j+1) + \Phi(1,j-1) + \Phi(2,j) + V(j))/3 \qquad (2-11b)$$

Foundation Interface:

$$\Phi(i,1) = (\Phi(i-1,1) + \Phi(i+1,1) + \Phi(i,2))/3 \qquad (2-11c)$$

Reservoir Surface:

$$\Phi(1,n) = (\Phi(i-1,n) + \Phi(i+1,n) + \Phi(i,n-1))/5 \qquad (2-11d)$$

Reservoir Vertical:

$$\Phi(m,j) = (\Phi(m,j+1) + \Phi(m,j-1) + \Phi(m-1,j))/5 \qquad (2-11e)$$

Dam-Foundation Corner:

$$\Phi(1,1) = (\Phi(1,2) + \Phi(2,1) + V(1))/2 \qquad (2-11f)$$

Dam-Surface Corner:

$$\Phi(1,n) = (\Phi(1,n-1) + \Phi(2,n) + V(n))/4 \qquad (2-11g)$$

Foundation-Reservoir Vertical Corner:

$$\Phi(m,1) = (\Phi(m-1,1) + \Phi(m,2))/4 \qquad (2-11h)$$

Surface-Reservoir Vertical Corner:

$$\Phi(m,n) = (\Phi(m-1,n) + \Phi(m,n-1))/6 \qquad (2-11i)$$

NB: It is necessary to change the calculation style of the spreadsheet from "iterative" to "manual" to prevent circular references. It is also necessary to provide a suitable convergence criterion for the iteration process.

3. Define the velocity at the dam-reservoir interface, V(j), and lump its values at the cells along the selected boundary.

4. Iterate on the above formulae until convergence is met.

5. Evaluate the hydrodynamic pressures at the upstream surface from the fluid potentials obtained.

In the case of earthquake excitation of a dam structure, step 3 in this process is complicated by the fact that many vibration modes contribute to the overall response and hence should be considered. In addition to the vibration modes, the rigid body mode, arising from the variable transformation and representing the earthquake motion of the base, needs to be considered. In this study, only one dam mode is considered in addition to the rigid body mode to estimate the envelope of the absolute accelerations. Therefore, it is necessary to modify the method presented by Kolkman in order to accommodate the analysis criteria for Ruskin Dam.

2.1.4 Modified Kolkman Method

During a work internship at BC Hydro in summer 2003, the author incorporated modifications to the Kolkman method to allow for estimation of the hydrodynamic pressures given input accelerations. The following example will demonstrate that it is possible to apply such modifications to the Kolkman method without compromising the integrity of the results.

Example: Dam-Surface Corner

Given the continuity equation for the Dam-Surface corner element in the Kolkman grid:

$$\sum \Delta q = \Delta q_L + \Delta q_U + \Delta q_R + \Delta q_D = 0 \tag{2-12a}$$

where:

$$\begin{aligned} \Delta q_L &= V_L \Delta L - 2\Phi \\ \Delta q_U &= -2\Phi \\ \Delta q_R &= \Phi_R - \Phi \\ \Delta q_D &= \Phi_D - \Phi \end{aligned} \tag{2-12b}$$

It follows that:

$$\Phi = \frac{(V(y)\Delta L + \Phi_R + \Phi_D)}{6} \tag{2-12c}$$

Multiplying both sides by $i\omega\rho$ yields:

$$i\omega\rho\Phi = \frac{i\omega\rho V(y)\Delta L + i\omega\rho\,(\Phi_R + \Phi_D)}{6} \tag{2-12d}$$

Since the pressure, $P = i\omega\rho\Phi$, and the input acceleration, $A(y) = i\omega V(y)$, this expression simplifies further to:

$$P(y) = \frac{\rho A(y)\Delta L + P_R + P_D}{6} \tag{2-12e}$$

The pressures for the remaining elements in the Kolkman grid are formulated in a similar manner. Since the pressures are independent of the frequency term, $i\omega$, it is possible to interpret the fluid potential functions Φ directly as pressures P, provided the input accelerations are used in place of the input velocities.

Modal combinations of pressures are obtained by applying modal combination techniques on the above pressure distributions. However, the resulting pressures may not be reliable, as they represent envelope values that do not necessarily occur simultaneously. The pressures used in the modified Kolkman method were obtained using the Square Root Sum of Squares (SRSS) combination of the modal accelerations.

$$\ddot{x}_{SRSS} = SRSS\lfloor \ddot{x}_g, c_1\phi_1(h), c_2\phi_2(h), \ldots \rfloor \tag{2-13}$$

where $\ddot{x}_g$ is the peak ground acceleration, or rigid-body mode acceleration, $c_1, c_2, \ldots$ represent modal combination factors and $\phi_1, \phi_2, \ldots$ represent the mode shapes in the relative coordinate system. Each mode is associated with a response frequency, $i\omega_1, i\omega_2, \ldots$ and the earthquake motion is also associated with a characteristic frequency $i\omega_g$. For each mode, the input velocity at the dam-reservoir interface is defined by the following set of equations:

$$\begin{aligned} v_0(h) &= \ddot{x}_g / i\omega_g \\ v_1(h) &= c_1\phi_1(h)/i\omega_1 \\ v_2(h) &= c_2\phi_2(h)/i\omega_2 \\ &\vdots \end{aligned} \tag{2-14}$$

where the velocities are proportional to the potential functions. The potential functions are solved individually and the pressures are extracted by taking the first derivative with respect to time, such that:

$$\begin{aligned} p_0(h) &= \rho i \omega_g \Phi_0(x=0,h) \\ p_1(h) &= \rho i \omega_1 \Phi_1(x=0,h) \\ p_2(h) &= \rho i \omega_2 \Phi_2(x=0,h) \\ &\vdots \end{aligned} \qquad (2-15)$$

By inspection, the frequency terms cancel out, making it possible to interpret the fluid potential functions directly as pressures if acceleration components are used instead of velocities. A similar effect can be obtained by setting $\omega = 1$ for all modes.

2.1.5 Zangar-Kolkman Comparison

During a work internship at BC Hydro in summer 2003, the author performed a complementary study to compare the hydrodynamic pressures of the modified Kolkman Method to the Zangar Method. The purpose of this study was to provide supporting evidence that the Kolkman Method yields similar results to those of the Zangar Method. Both the Kolkman and Zangar pressures were calculated along a vertical dam-reservoir interface for the rigid body mode. Figure 2-1 shows the hydrodynamic pressure distributions for Zangar, Kolkman with a 70m long reservoir, and Kolkman with a 140m long reservoir.

By inspection, the shape of the Kolkman pressure distribution corresponds to that of the Zangar pressure distribution. By doubling the length of the reservoir, the

Kolkman pressures were found to asymptotically approach the Zangar pressures. However, the difference between the 70m reservoir and the 140m reservoir was found to be negligible (less than 2%), suggesting that for large reservoir lengths, the hydrodynamic pressures have relatively low sensitivity to variation of the length parameter. Conversely, for shorter reservoir lengths, the hydrodynamic pressures will be lower, with a higher sensitivity to the reservoir length.

2.2 METHODOLOGY

The first part of this study involved creating a simplified two degree-of-freedom model to represent the dam-gate system of Ruskin Dam.

The next step was to formulate the equations of motion of this 2-DOF system, using principles of energy conservation.

The next step was to perform a modal analysis on the 2-DOF model.

1. Formulate the composite mass matrix, $[m^*]$
2. Formulate the stiffness matrix, $[k]$
3. Determine the eigenvectors, λ_1 and λ_2, by solving the characteristic equation, $\det[[k]-[\lambda][m^*]]=0$
4. Calculate the modal participation factors, Γ_1 and Γ_2
5. Determine the spectral accelerations, SA_1 and SA_2 from the Uniform Hazard Response Spectrum. It was first necessary to adjust the UHRS from the absolute frame of reference to the relative frame of reference.
6. Calculate the modal accelerations, A_1 and A_2
7. Combine the modal accelerations to obtain the absolute acceleration of the dam-reservoir interface.
8. Using the absolute acceleration of the dam-reservoir interface, apply the Kolkman Method to calculate the hydrodynamic loads.

2.2.1 2-DOF Model

To take the calculation of hydrodynamic pressures one step further, the gate flexibility was also considered. To do so, a simplified two degree-of-freedom model was created as an approximate representation of how the dam-gate system will respond to an earthquake excitation. The conceptual model, shown in Figure 2-2, included two degrees of freedom, one representing the response of the dam and one representing the response of the gate. The degree of freedom associated with the dam response was assumed to have a mode shape consistent with that suggested by Chopra and Tan [5] for lower spillway structures, exhibited in Figure 2-3. For simplicity, it was assumed that the gate degree of freedom was connected to the top of the dam structure. Each gate of Ruskin Dam was modeled separately, to account for varying seismic parameters (ie. seismic amplification) and dam geometry (ie. height of the dam section).

Initial estimates of gate pressures computed by superimposing the expected gate deformations over the response of the dam indicated that pressures higher than amplified Zangar pressures were possible with realistic gate deflection levels. However, this assumed superposition is an unrealistic assessment as it neglects the interaction between the dam and gate structures. Due to the potential high cost of retrofit to the gates and possible need for additional pier retrofit, it was appropriate to examine the nature of this dam-gate interaction. With this understanding, it was then possible to provide more realistic gate loads for the assessment of the gate structures.

As the current investigation into the seismic withstand capacity of the gates was at a conceptual level, it was decided that a sophisticated analysis was not necessary. As such, the 2-DOF model presented in this section is the simplest possible model necessary to evaluate the dam-gate interaction. This model was complex enough to represent the response of the dam and gate, but simple enough to be implemented in a spreadsheet. During this preliminary design phase of the study, it was recognized that the need for refining the dam-gate interaction study with more sophisticated analysis techniques would be reassessed if the results from the simplified analysis indicate sufficient benefit for doing so.

2.2.1.1 Assumptions

For this entire study, a 10% damping value was assumed. The spectral accelerations used in the analysis were extracted from a Uniform Hazard Response Spectra for the case of 10% damping and 1/10000 annual exceedence frequency (AEF). However, this UHRS was in the absolute frame of reference, and therefore engineering judgment was used to transform the spectral acceleration curves to the absolute frame of reference; this will be discussed later in this section. The first mode shape recommended by Chopra and Tan [5] for low dam structures was used to represent the deflected shape of the dam structure. The two degrees of freedom were represented as generalized lumped masses, based on formulae presented by Fenves and Chopra [7]. These generalized masses were dependent on the Chopra mode shape, and the formulae will be presented later in this section.

The Kolkman Method assumes the water is an incompressible fluid. It is well known that issues pertaining to compressibility of the water influence the hydrodynamic loads on dam structures.

It is assumed that each dam-gate section analyzed in this chapter has the same natural frequency of the entire dam, 7.1Hz, which was computed from a finite-element analysis.

2.2.2 Formulation of the Equations of Motion

In order to determine the mass and stiffness matrices to be used in the modal analysis, it was first necessary to formulate the equations of motion. Assuming that the total energy of the system consists of potential and kinetic energy, the equation of motion was formulated by computing partial derivatives of these quantities. Figure 2-2 shows the simplified dam model and the locations of the referenced degrees of freedom.

2.2.2.1 Boundary Conditions

The first step in formulating the equations of motion is to establish a set of boundary conditions by which the model is governed:

$$
\begin{aligned}
&u_g'(t) = u_d(H,t) + u_g(t) \\
&u_d(0,t) = 0 \\
&u_d(H,t) = \alpha\psi_1(H)u_{d0}(t)
\end{aligned}
\tag{2-16}
$$

where $u_g(t)$ is the response of the gate degree of freedom relative to the dam at height H and time t, $u_g^{\prime}(t)$ is the absolute response of the gate degree of freedom at time t, $u_d(z,t)$ is the absolute response of the dam degree of freedom at height z (elevation above ground) and time t, $u_{d0}(t)$ is the displacement response of the generalized dam variable at time t, α is the geometric amplification factor relating the spectral acceleration to the modal acceleration determined in a previous 3-D finite-element modal analysis, and $\psi_1(z)$ is the Chopra mode shape at height z.

Further simplification of these boundary conditions leads to:

$$\begin{aligned} u_g^{\prime}(t) &= u_{d0}(t)\alpha\psi_1(H)+u_g(t) \\ u_d(z,t) &= u_{d0}(t)\alpha\psi_1(z) \end{aligned} \qquad (2-17)$$

2.2.2.2 Geometric Amplification

The geometric amplification factor, α, is shown in Figure 2-2 as the ratio of the displacement of the generalized dam mass and the displacement at the top of the structure where the gate is connected. This geometric amplification factor was computed as the ratio of the spectral acceleration at the dam frequency (7.1 Hz) to the acceleration extracted from the 3-D finite element modal analysis. Since the spectral acceleration is combined with the rigid body mode acceleration, it is necessary to remove the rigid body mode component of the spectral acceleration from the formulation of α.

$$\alpha = \frac{\sqrt{[(AF)(PGA)]^2 - A_{RBM}{}^2}}{SA} \qquad (2-18)$$

where AF is the modal amplification factor, A_{RBM} is the rigid body mode acceleration, and SA is the spectral acceleration.

2.2.2.3 Derivation of the Equations of Motion using Energy Methods

In order to formulate the equations of motion for this 2DOF system, the first step is to solve the energy equation of the system. A prior assumption to this was that all the energy in the system is in the form of kinetic or potential energy.

The Kinetic Energy equation of the system:

$$T = \int_0^H \frac{1}{2} m_d(z)\dot{u}_d(z,t)^2\,dz + \frac{1}{2} m_g \dot{u}_g{}'(t)^2$$

$$T = \frac{1}{2}\int_0^H m_d(z)[\dot{u}_{d0}(t)\alpha\psi_1(z)]^2\,dz + \frac{1}{2} m_g\left[u_{d0}(t)\alpha\psi_1(H) + u_g(t)\right]^2 \qquad (2-19)$$

The Potential Energy equation of the system:

$$V = \int_0^H \frac{1}{2} k_d(z)u_d(z,t)^2\,dz + \frac{1}{2} k_g u_g(t)^2$$

$$V = \frac{1}{2}\int_0^H k_d(z)[u_{d0}(t)\alpha\psi_1(z)]^2\,dz + \frac{1}{2} k_g u_g(t)^2 \qquad (2-20)$$

2.2.2.4 Generalization of Parameters

One critical assumption in this study is that the dam degree of freedom behaves like a generalized SDOF system, with distributed mass and stiffness. For the case of an infinitely rigid and rigidly attached gate, the dam-gate system essentially behaves like a generalized SDOF system. According to Chopra and Tan [5], given an assumed shape function, structures with distributed mass and stiffness can be simplified to a SDOF system with generalized mass and stiffness that are lumped at the location of the generalized response variable. In the case of this 2DOF model, that generalized response variable is located at the dam's geometric centroid, which varies depending on which gate is being analyzed.

In this study, the assumed shape function is that suggested by Chopra and Tan with regards to low spillway structures (less than 91m in total height, including monolith and piers). The generalized mass and stiffness are as follows:

$$\widetilde{m} = \int_0^H m_d(z)\left[\psi_1(z)\right]^2 dz \qquad (2-21a)$$

$$\widetilde{k} = \int_0^H EI_d(z)\left[\psi_1''(z)\right]^2 dz \qquad (2-21b)$$

Table 2-1 summarizes the total and generalized masses for the dam degree-of-freedom of each dam-gate section. In general, the generalized mass is less than the total mass, due to the $\left[\psi_1(z)\right]^2$ term in the integration, which amplifies the effective mass at the top of the structure while practically eliminating the mass at the base. For the internal gate sections, the effective mass at the top of the structure (pier and deck) is amplified by up to 7 times (pier and deck at Gate 4, 691 tonnes amplified to 5026 tonnes).

TABLE 2-1: Summary of Total Mass and Generalized Mass

Summary of Total Mass and Generalized Mass for 40-ft Gate + Pier Sections

		Gate 1	Gate 2	Gate 3	Gate 4	Gate 5	Gate 6	Gate 7
Dam	Total Mass	1903.2	4587.9	17815.7	23405.4	23405.4	21809.1	9508.8
Dam	Generalized Mass	47.1	507.0	6914.7	14617.0	13593.4	6975.7	1151.2
		2.5%	11.1%	38.8%	62.5%	58.1%	32.0%	12.1%
Pier + Deck	Total Mass	691.4	691.4	691.4	691.4	691.4	691.4	691.4
Pier + Deck	Generalized Mass	615.5	1404.4	3289.2	5026.3	4674.4	2160.6	1154.1
		89.0%	203.1%	475.7%	726.9%	676.0%	312.5%	166.9%
Total	Total Mass	2594.6	5279.3	18507.1	24096.9	24096.9	22500.5	10200.2
Total	Generalized Mass	662.6	1911.4	10203.8	19643.3	18267.8	9136.2	2305.3
		25.5%	36.2%	55.1%	81.5%	75.8%	40.6%	22.6%

*All mass units in tonnes

2.2.2.5 Equations of Motion

For simplicity, damping terms were neglected, and the equation of motion of the model was formulated by taking partial integrals of the energy terms:

$$\frac{d}{dt}\left[\frac{\partial T}{\partial \dot{u}_{d0}}+\frac{\partial T}{\partial \dot{u}_g}\right]+\left[\frac{\partial V}{\partial u_{d0}}+\frac{\partial V}{\partial u_g}\right]=[m][\ddot{u}]+[k][u]=-[m][L]\ddot{u}_0-F_{ext}$$

$$\begin{bmatrix} m_{11} & m_{12} \\ m_{21} & m_{22} \end{bmatrix}\begin{bmatrix} \ddot{u}_{d0} \\ \ddot{u}_g \end{bmatrix}+\begin{bmatrix} k_{11} & k_{12} \\ k_{21} & k_{22} \end{bmatrix}\begin{bmatrix} u_{d0} \\ u_g \end{bmatrix}=-\begin{bmatrix} m_{11} & m_{12} \\ m_{21} & m_{22} \end{bmatrix}\begin{bmatrix} L_1 \\ L_2 \end{bmatrix}\ddot{u}_0-F_{ext} \qquad (2-22)$$

Where the mass matrix term m_{ij} is the effective mass at degree of freedom j for a unit displacement of degree of freedom i, and the general stiffness term k_{ij} is the effective stiffness at degree of freedom j for a unit displacement of degree of freedom i. On the right side of the equation, the L_k term is the modal expansion factor for degree of freedom k and the F_{ext} term is the sum of the external forces acting on the system. The partial derivatives are expanded as follows:

$$\frac{d}{dt}\frac{\partial T}{\partial \dot{u}_{d0}}=\alpha^2\ddot{u}_{d0}\int_0^H m_d(z)[\psi_1(z)]^2\,dz=\alpha^2\tilde{m}_d\ddot{u}_{d0}$$

$$\frac{d}{dt}\frac{\partial T}{\partial \dot{u}_g}=m_g\ddot{u}_g$$

$$\frac{\partial V}{\partial u_{d0}}=\alpha^2 u_{d0}\int_0^H k_d(z)[\psi_1(z)]^2\,dz+k_g(u_g-\alpha u_{d0})(-\alpha)=\alpha^2\tilde{k}_d * u_{d0}+k_g(u_g-\alpha u_{d0})(-\alpha)$$

$$\frac{\partial V}{\partial u_g}=k_g(u_g-\alpha u_{d0})$$

Where the $\tilde{k}_d *$ denotes a variation in the generalized stiffness. In the modal analysis, this parameter is calibrated by setting the dam frequency based on the

3-D modal analysis results (7.1 Hz). This leads to the equation of motion for the 2DOF model:

$$\begin{bmatrix} \alpha^2 \tilde{m}_d & 0 \\ 0 & m_g \end{bmatrix} \begin{bmatrix} \ddot{u}_{d0} \\ \ddot{u}_g \end{bmatrix} + \begin{bmatrix} \alpha^2 \tilde{k}_d * & -\alpha k_g \\ -\alpha k_g & k_g \end{bmatrix} \begin{bmatrix} u_{d0} \\ u_g \end{bmatrix} = -\begin{bmatrix} \alpha^2 \tilde{m}_d & 0 \\ 0 & m_g \end{bmatrix} \begin{bmatrix} L_1 \\ L_2 \end{bmatrix} \ddot{u}_0 - F_{ext} \qquad (2-23a)$$

or:

$$[m][\ddot{u}] + [k][u] = -[m][L]\ddot{u}_0 - F_{ext} \qquad (2-23b)$$

In this particular case, the F_{ext} term is critical, as it represents the hydrodynamic loads induced by the system. The mass and stiffness matrices have also been defined:

$$m = \begin{bmatrix} \alpha^2 \tilde{m}_d & 0 \\ 0 & m_g \end{bmatrix} \qquad (2-24a)$$

$$k = \begin{bmatrix} \alpha^2 \tilde{k}_d * & -\alpha k_g \\ -\alpha k_g & k_g \end{bmatrix} \qquad (2-24b)$$

Given the shape vectors ψ_1 and ψ_2, which represent the unit virtual displacement of the dam and gate degrees of freedom, respectively, and the hydrodynamic pressures, P_0, P_1, and P_2, generated for the unit displacement of the ground, dam DOF, and gate DOF, respectively, the external forces, F_{ext}, can be calculated as follows:

$$F_{ext} = \left(\int P_0 \ddot{u}_0 \psi_1 dz + \int P_0 \ddot{u}_0 \psi_2 dz\right) + \left(\int P_1 \ddot{u}_{d0} \psi_1 dz + \int P_1 \ddot{u}_{d0} \psi_2 dz\right) + \left(\int P_2 \ddot{u}_g \psi_1 dz + \int P_2 \ddot{u}_g \psi_2 dz\right) \qquad (2-25)$$

For example, each term on the right side of the equation $\int P_i \ddot{u}_i \psi_j dz$ is the integral of the forces $P_i \ddot{u}_i$ generated by a unit acceleration of mode i subjected to a virtual displacement ψ_j at degree of freedom j, over the height of the dam. Further simplification of this equation yields:

$$F_{ext} = \begin{bmatrix} \int P_1 \psi_1 dz & \int P_1 \psi_1 dz \\ \int P_1 \psi_2 dz & \int P_1 \psi_2 dz \end{bmatrix} \begin{bmatrix} \ddot{u}_{d0} \\ \ddot{u}_g \end{bmatrix} + \begin{bmatrix} \int P_0 \psi_1 dz \\ \int P_0 \psi_2 dz \end{bmatrix} \ddot{u}_0 \qquad (2-26a)$$

$$F_{ext} = \begin{bmatrix} \mu_{d1} & \mu_{g1} \\ \mu_{d2} & \mu_{g2} \end{bmatrix} \begin{bmatrix} \ddot{u}_{d0} \\ \ddot{u}_g \end{bmatrix} + \begin{bmatrix} \int P_0 \psi_1 dz \\ \int P_0 \psi_2 dz \end{bmatrix} \ddot{u}_0 \qquad (2-26b)$$

Herein, the hydrodynamic mass matrix, μ, has been defined:

$$\mu = \begin{bmatrix} \mu_{d1} & \mu_{g1} \\ \mu_{d2} & \mu_{g2} \end{bmatrix} \qquad (2-27)$$

Subsequently, the total mass matrix, m^*, can be expressed as a sum of the original mass matrix, m, and the hydrodynamic mass matrix, μ:

$$m^* = \begin{bmatrix} \alpha^2 \tilde{m}_d & 0 \\ 0 & m_g \end{bmatrix} + \begin{bmatrix} \mu_{d1} & \mu_{g1} \\ \mu_{d2} & \mu_{g2} \end{bmatrix} = \begin{bmatrix} \alpha^2 \tilde{m}_d + \mu_{d1} & \mu_{g1} \\ \mu_{d2} & m_g + \mu_{g2} \end{bmatrix} \qquad (2-28)$$

Now, the equation of motion can be rewritten in its standard form:

$$[m^*][\ddot{u}]+[k][u]=-[m^*][L^*]\ddot{u}_0 \qquad (2-29)$$

where:

$$[m^*][L^*]=[m][L]+\begin{bmatrix}\int P_0\psi_1 dz\\ \int P_0\psi_2 dz\end{bmatrix}\xrightarrow{solving}[L^*]=[m^*]^{-1}\left[[m][L]+\begin{bmatrix}\mu_{01}\\ \mu_{02}\end{bmatrix}\right] \qquad (2-30)$$

where L^* is the new modal expansion factor for the 2DOF model.

2.2.3 2DOF Modal Analysis

A 2DOF modal analysis was performed in order to calculate the modal accelerations of the generalized response variables. The first step in this iterative procedure was to calibrate the model to the rigid-gate case, for which the gate was assigned a large frequency value, characteristic of a large stiffness to mass ratio. The purpose of calibrating the model was to check the geometric amplification factor, α. The calibrated model yielded reasonable results, as the total hydrodynamic force on the gate was approximately equal to the Kolkman rigid-gate case.

The next step was to perform 2-DOF modal analyses while gradually introducing gate flexibility by decreasing the gate frequency. This process was performed on all seven dam-gate sections. Figure 2-4 shows a sample of the 2-DOF modal analysis worksheet used to carry out the calculations. This worksheet is explained in Appendix A.

2.2.3.1 Mass Matrix

As stated earlier, the mass matrix used in the 2DOF modal analysis, $[m^*]$, consists of a structural mass component, $[m]$, and a hydrodynamic mass component, $[\mu]$. This composite mass matrix has the form:

$$m^* = \begin{bmatrix} \alpha^2 \tilde{m}_d + \mu_{d1} & \mu_{g1} \\ \mu_{d2} & m_g + \mu_{g2} \end{bmatrix} \qquad (2-31)$$

From this equation, the mass of each spillway gate, m_g, is approximately 30.5 tonnes. Table 2-1 summarizes the values of $\tilde{m}_d$, the generalized masses of each dam-gate segment. The generalized mass for each dam-gate section is calculated by integrating the product of the distributed mass and the square of the Chopra mode shape over the height of the dam. Since the height varies from block to block, the generalized mass also varies, as shown in the summarized results. For Gate 4, the generalized mass, $\alpha^2 \tilde{m}_d$, was calculated to be 19643 tonnes.

The hydrodynamic added masses are calculated by virtual work of hydrodynamic pressures due to unit displacements of the degrees of freedom. Initially, the hydrodynamic added mass matrix was not perfectly symmetric. In order to alleviate this, the non-symmetric values, μ_{g1} and μ_{d2}, were interpolated to achieve symmetry, in order to avoid complexity in the modal analysis. To demonstrate this, the added masses for Gate 4, expressed in tones, were altered as shown below:

$$\begin{matrix} \mu_{d1} = 9425 \\ \mu_{g1} = 502 \\ \mu_{d2} = 512 \\ \mu_{g2} = 209 \end{matrix} \rightarrow \begin{matrix} \mu_{d1} = 9425 \\ \mu_{g1} = 507 \\ \mu_{d2} = 507 \\ \mu_{g2} = 209 \end{matrix} \rightarrow [\mu] = \begin{bmatrix} 9425 & 507 \\ 507 & 209 \end{bmatrix}$$

The composite mass matrix for Gate 4 in tonnes was then computed as:

$$m^* = \begin{bmatrix} 29068 & 507 \\ 507 & 239 \end{bmatrix}$$

2.2.3.2 Stiffness Matrix

As stated earlier, the stiffness matrix used in the 2DOF modal analysis, $[k]$, has the form:

$$k = \begin{bmatrix} \alpha^2 \tilde{k}_d^* & -\alpha k_g \\ -\alpha k_g & k_g \end{bmatrix} \tag{2-24b}$$

Since it would be very difficult to accurately calculate or measure the stiffness of the dam-gate section, the stiffnesses, $\tilde{k}_d$ and k_g, were back-calculated from the mass and natural frequency parameters for the dam and gate.

For the gate, a finite-element modal analysis was performed on the gates with hydrodynamic loads, yielding a natural frequency, f_g^*, of 7.4 Hz. This model was based on the self-weight and just the diagonal term of the hydrodynamic added mass matrix pertaining to the gate, μ_{g2}; ie. the added mass on the gate due to a virtual unit displacement of the gate DOF. However, the hydrodynamic added mass due to the virtual displacement of the dam, μ_{g1}, was not incorporated. As such, in order to calculate the stiffness of the gate, it was first necessary to adjust the frequency to include this additional hydrodynamic added mass term. For Gate 4:

$$f_g{}^* = \frac{1}{2\pi}\sqrt{\frac{k_g}{m_{g1} + \mu_{g2}}} = 7.4Hz$$
$$k_g = [2\pi(7.4Hz)]^2(30.5 + 209) = 0.52 \times 10^6 \ kN/m$$

Where $f_g{}^* = 7.4Hz$ is the frequency that was calculated using a finite element model of the gate with added mass, and k_g is the stiffness of the dam-gate section based on the frequency provided.

For the dam, a previous finite-element model yielded a natural frequency, f_d, of 7.1 Hz. Since this frequency is representative of the first vibration mode of the entire dam model, it is assumed that each dam-gate section behaves similar to the entire dam and that 3-D effects are neglected. It follows that the generalized stiffness of the dam is calculated as follows:

$$f_d = \frac{1}{2\pi}\sqrt{\frac{k_d}{m_{d1} + \mu_{d1} + \mu_{d2}}} = 7.1Hz$$
$$k_d = [2\pi(7.1Hz)]^2(19643 + 9425 + 507) = 58.9 \times 10^6 \ kN/m$$

Where k_d is the stiffness of the dam-gate section based on the frequency provided. Accordingly, the stiffness matrix for Gate 4 was then computed as:

$$k = \begin{bmatrix} 0.52 & -1.66 \\ -1.66 & 64.2 \end{bmatrix} \times 10^6 \; kN/m$$

2.2.3.3 2DOF Modal Analysis

The characteristic equation was used to formulate the natural frequencies (eigenvalues) and mode shapes (eigenvectors). Then, the participation factors were calculated using formulae presented by Chopra [4]. Finally, the modal accelerations were calculated, based on spectral acceleration values extracted from the UHRS for Ruskin Dam.

The characteristic equation:

$$\det[[k]-[\lambda][m^*]] = 0 \qquad (2-27)$$

Solve the eigenvalues, λ_1 and λ_2, then replace back into the formal solution to solve the eigenvectors:

$$[[k]-\lambda_1[m^*]]\phi_1 = 0 \qquad (2-28a)$$

$$[[k]-\lambda_2[m^*]]\phi_2 = 0 \qquad (2-28b)$$

Where ϕ_1 and ϕ_2 are the eigenvectors representing the mode shapes for modes 1 and 2, respectively. Given the eigenvectors, the next step is to calculate the modal participation factors:

$$\Gamma_1 = \frac{\phi_1^T m * L *}{\phi_1^T m * \phi_1} \qquad (2-29a)$$

$$\Gamma_2 = \frac{\phi_2^T m * L *}{\phi_2^T m * \phi_2} \qquad (2-29b)$$

Then, given the spectral accelerations from the UHRS, the modal accelerations for the two degrees of freedom can be computed:

$$[A_1] = SA_1 \Gamma_1 [\phi_1] \qquad (2-30a)$$

$$[A_2] = SA_2 \Gamma_2 [\phi_2] \qquad (2-30b)$$

2.2.3.4 Combination of Modal Accelerations

Given the peak ground acceleration and the two modal accelerations from the 2DOF modal analysis, the next step is to combine the accelerations to obtain the combined absolute acceleration of the dam-reservoir interface. It was proven that the resulting pressures were identical regardless of whether the accelerations were combined before or after they were input into the Kolkman spreadsheet.

2.2.3.5 Adjusting the Uniform Hazard Response Spectra

Similar to the seismic response of a structure, the dam responds to earthquake vibrations by means of a "rigid body" motion superimposed with the modal response to the earthquake vibrations. The rigid body mode results from the transformation of co-ordinates from an absolute frame of reference to a reference frame that moves relative to the earthquake. This transformation of co-ordinates is necessary in the formulation of the equations of motion, allowing for the direct input of acceleration data to obtain the hydrodynamic pressures.

Since the UHRS for Ruskin Dam was provided in the absolute frame of reference (ie. Spectral acceleration = PGA for period of 0 sec), it was necessary to modify it so it would comply with the conditions of the relative frame of reference. This modification was required for consistency with the rest of the modal analysis, which was carried out in the relative frame of reference. The difference between the two frames of reference is the rigid body mode, which is incorporated into the modal combination later in the analysis. The criteria for this modification were:

1. SA = 0 at T = 0 sec
2. SA $\rightarrow$ PGA as T $\rightarrow \infty$
3. SA_{max} is preserved after the modification

Figure 2-5 shows the co-ordinate transformation of the UHRS from the absolute frame of reference to the relative frame of reference. The upper plot shows the boundary conditions satisfied by the coordinate transfer. The bottom plot shows the same curves within the period range of interest for this study. The rigid body mode is combined with the relative modes later in the process, to extract the combined absolute accelerations.

2.2.3.6 Applying the Kolkman Method

The acceleration values for each degree of freedom from the 2DOF modal analysis were used to calculate the accelerations at the evenly-spaced node locations along the dam elevation for each of the two modes. Using the Chopra mode shape as a basis, the rigid body mode accelerations and relative accelerations were then input into the Kolkman spreadsheet, in order to calculate the hydrodynamic pressures along the dam-reservoir interface.

The pressures are then integrated over the surface area of the gate to obtain the hydrodynamic loads on each of the seven gates. These loads are then compared to the loads due to Zangar and Amplified Zangar hydrodynamic pressures to evaluate the feasibility of continuing this study.

2.3 DISCUSSION OF RESULTS

Figure 2-6 summarizes the effect of varying the gate frequency parameter on the hydrodynamic loads for Gate 4. This plot shows the total hydrodynamic load on the gate for various frequencies. The frequencies were expressed as the Period Ratio between gate period T_g and dam period T_d, given a constant dam period of 0.14s and a varying gate period. For the rigid gate case $(f_g >> 0)$, the total gate force is equal to that calculated for the rigid-gate Kolkman case; approximately 10400 kN. The total gate force increases with decrease in gate frequency until close to resonance with the dam frequency $(f_g = 7.4Hz)$, where it reaches a maximum of approximately 16100 kN, or approximately 74% of the Amplified Zangar total gate force. Decreasing the gate frequency beyond the resonant frequency results in a decrease in the total gate force. The total gate force decreases below the rigid-gate Kolkman force at $f_g = 3.94Hz$, and asymptotically approaches a value well below the rigid-gate Kolkman force. The remaining gates experience similar results to those shown for Gate 4.

Figure 2-6 also shows the variation of peak acceleration of the dam and the gate at the water level. For the rigid gate case, the accelerations are 26.5 m/s^2 for both the dam and the gate. As the gate frequency decreases to the resonant condition, the dam acceleration decreases to approximately 19 m/s^2 and the gate acceleration increases to approximately 69 m/s^2. As the gate frequency decreases beyond the resonance frequency, the dam acceleration gradually increases and the gate acceleration gradually decreases to a value less than the fixed gate acceleration. This indicates a larger participation of the second vibration mode as the gate frequency approaches the dam frequency.

Figure 2-7 summarizes the total hydrodynamic force on all the gates. The total force on the gates vary from approximately 5000 kN at Gate 1 near the right abutment, to approximately 16000 kN at Gate 4 near the center of the crest, to approximately 8000 kN at Gate 7 near the left abutment. The total force on each gate exceeds the rigid-gate Kolkman force but does not exceed the Amplified Zangar force.

2.4 CONCLUSIONS

A modal analysis of a 2DOF simplified model representing a portion of a gravity dam structure was successfully carried out. The main purposes of this study were to evaluate the effect of dam-gate interaction on the hydrodynamic loads and to evaluate the effect of varying the natural frequency of the gate. The following can be concluded from this study.

2.4.1 Regarding the Modified Kolkman Method

- The method presented by Kolkman is useful for considering the dam-gate-reservoir interaction in the formulation of hydrodynamic loads. Conversely, the methods presented by Westergaard and Zangar do not consider the relative response of the gate to the dam.
- The hydrodynamic loads formulated by this method are consistent with those formulated by the Zangar method. This was verified by formulating the hydrodynamic loads for the case of an infinitely rigid dam structure.
- When subjected to dynamic excitation, the dam-gate interaction changed the distribution of hydrodynamic loads along the upstream face of the dam.

2.4.2 Regarding the Effect of Dam-Gate Interaction on Hydrodynamic Loads

- It was necessary to consider the rigid body mode in estimating the effect of Dam-Gate interaction on the resulting hydrodynamic loads.
- The amplified Zangar hydrodynamic loads (computed by using added

mass) are much higher than those computed by using the rigid gate Kolkman Method.

- Dam-Gate interaction, when the gate frequency was set similar to the dam frequency, resulted in hydrodynamic loads higher than those observed for the Kolkman Rigid Gate scenario but lower than those computed using Amplified Zangar.

2.4.3 Regarding the Effect of Varying the Natural Frequency of the Gate

- The hydrodynamic loads for the extreme rigidity case were equal to those computed for the Kolkman Rigid Gate case.
- The peak hydrodynamic load occurred at resonance, when the gate frequency was equal to the dam frequency $(f_g \cong f_d)$.
- As the frequency was shifted towards extreme flexibility, the hydrodynamic load asymptotically approached a value less than that computed for the Kolkman Rigid Gate case.
- For the case of the actual gate frequency $(f_g \cong 7.4Hz)$, the total hydrodynamic load was approximately halfway between of the Amplified Zangar and the Rigid-Gate Kolkman hydrodynamic loads.
- It is possible to decrease the hydrodynamic loads on the gates by decreasing the natural frequency of the gate to beyond the natural frequency of the dam; ie. by increasing the flexibility of the gate system.
- Amplified accelerations of the gate were associated with a reduction of accelerations in the body of the dam.

In the current state of practice, the Amplified Zangar hydrodynamic masses attached to the upstream face of the dam are typically used in structural analyses. However, this process does not incorporate gate flexibility and it was unknown whether the resulting hydrodynamic pressures would be conservative or non-conservative in terms of design. For this study, the flexibility of the gate has a significant effect on the hydrodynamic forces experienced on the upstream face of the dam. Using a simplified 2-DOF model of a 40-ft wide section of a gravity dam, results were obtained that support this statement.

It was found that the hydrodynamic pressures determined by the 2-DOF modal analysis were substantially lower than those presented by the Amplified Zangar method. This suggests a possibility to reduce the cost of the retrofit work due to reduced design loads. However, there were a number of assumptions and simplifications made during this study that may have compromised the accuracy of the results. It is recommended to carry out a more refined study to improve the accuracy and reliability of the results.

It was also found that the hydrodynamic force on the gates could be reduced by decreasing the natural frequency of the gates beyond the resonance frequency of the dam. While softening the gates has been determined to reduce the total effective hydrodynamic loads, its value as a potential retrofit measure needs further investigation.

2.5 RECOMMENDATIONS

The results of this study are supportive of the Kolkman Method of determining hydrodynamic loads accounting for dam-gate-reservoir interaction. However, before implementing this method in practice, it is necessary to improve the precision of the model and analysis. Some recommendations for future work on this topic are:

1. Analysis using a more detailed full-scale 3-D model of a dam, to account for load sharing between dam blocks and the 3-D effects on the hydrodynamic loads.
2. More detailed computational analysis by means of Finite-Element Analysis software. This would entail an expansion of the 2DOF model to a more complex MDOF model.

FIGURE 2-1: Kolkman-Zangar Comparison

Kolkman - Simple Scheme for Calculating the Added Mass of Hydraulic Gates

Node Spacing 2.26 m

PGA 0.54 g

Zangar Scheme for Calculating the Added Mass of Hydraulic Gates

for WL = 42.9 m

h_{max} = 163.1 ft

a = 0.54 g

w = 62.4 lb/ft^3

C_m = 0.735

C = $(C_m/2)[(y/h)(2 - (y/h)) + [(y/h)(2 - (y/h))]^{1/2}]$

		Reservoir Vertical at 70 m		Reservoir Vertical at 140 m	
Elevation (m)	Height of Water y (ft)	Zangar Hydrodynamic Pressure (kPa)	Kolkman Hydrodynamic Pressure (kPa)	Zangar Hydrodynamic Pressure (kPa)	Kolkman Hydrodynamic Pressure (kPa)
42.91	**0.0**	**0.0**	**0.0**	**0.0**	**0.0**
41.78	**3.7**	**24.9**	**15.7**	**24.9**	**15.9**
39.52	**11.1**	**48.0**	**39.6**	**48.0**	**40.0**
37.26	**18.5**	**65.7**	**59.1**	**65.7**	**59.7**
35.00	**26.0**	**80.9**	**75.6**	**80.9**	**76.6**
32.74	33.4	94.4	90.1	94.4	91.3
30.48	40.8	106.5	102.8	106.5	104.3
28.22	48.2	117.6	114.2	117.6	115.9
25.96	55.6	127.8	124.3	127.8	126.2
23.70	63.0	137.0	133.4	137.0	135.6
21.44	70.4	145.4	141.6	145.4	143.9
19.18	77.9	153.1	148.9	153.1	151.4
16.92	85.3	160.1	155.4	160.1	158.1
14.66	92.7	166.3	161.2	166.3	164.1
12.40	100.1	171.9	166.3	171.9	169.4
10.14	107.5	176.8	170.7	176.8	174.0
7.88	114.9	181.1	174.6	181.1	177.9
5.62	122.3	184.8	177.8	184.8	181.3
3.36	129.8	187.8	180.5	187.8	184.1
1.10	137.2	190.2	182.6	190.2	186.3
-1.16	144.6	192.0	184.2	192.0	187.9
-3.42	152.0	193.2	185.3	193.2	189.0
-5.68	159.4	193.8	185.8	193.8	189.6

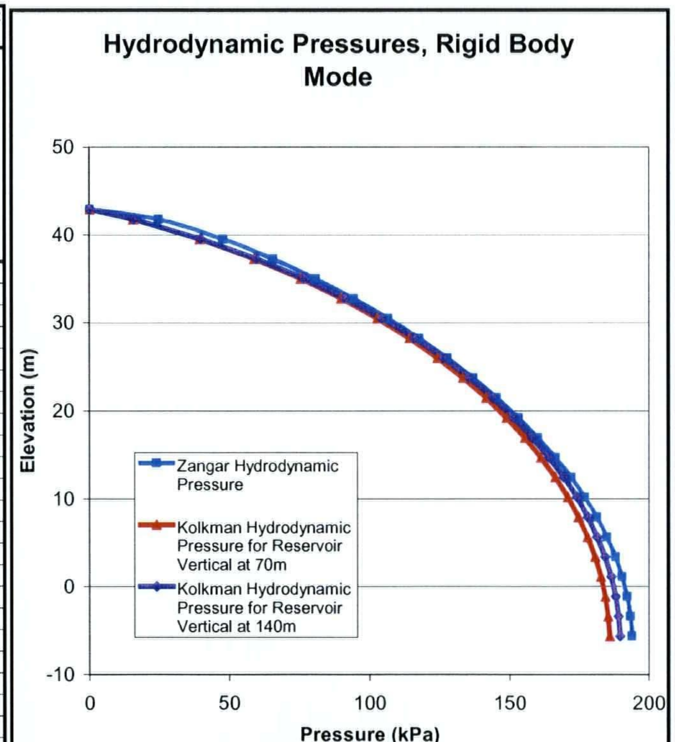

FIGURE 2-2: Conceptual 2-DOF Model

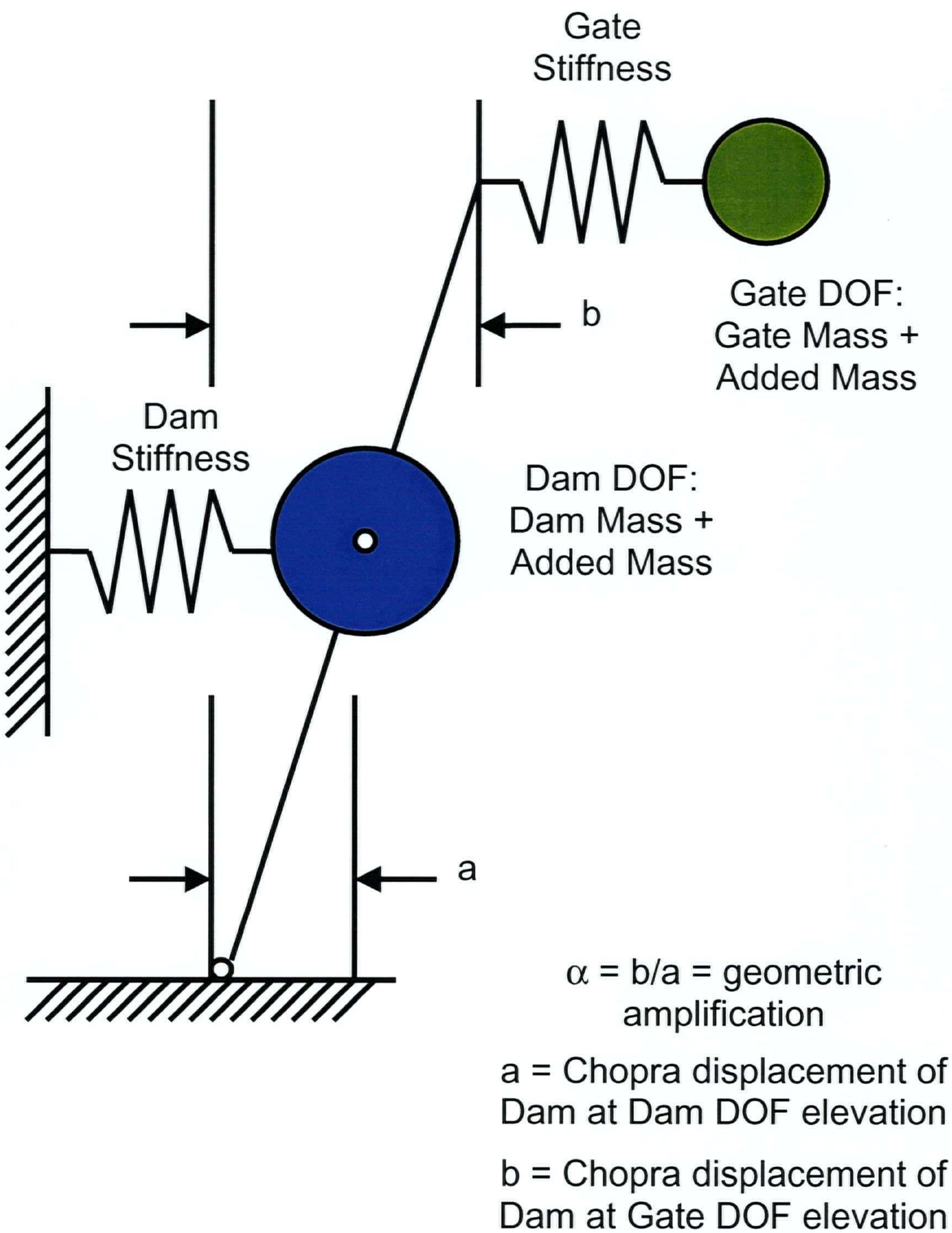

FIGURE 2-3: Chopra Recommended Mode Shape for Gated Spillways of Lower Concrete Monolith Dams

Elevation, z	Chopra Mode Shape
1.00	1.000
0.95	0.914
0.90	0.825
0.85	0.738
0.80	0.654
0.75	0.574
0.70	0.499
0.65	0.440
0.60	0.386
0.55	0.334
0.50	0.285
0.45	0.239
0.40	0.197
0.35	0.160
0.30	0.126
0.25	0.096
0.20	0.070
0.15	0.048
0.10	0.030
0.05	0.015
0.00	0.000

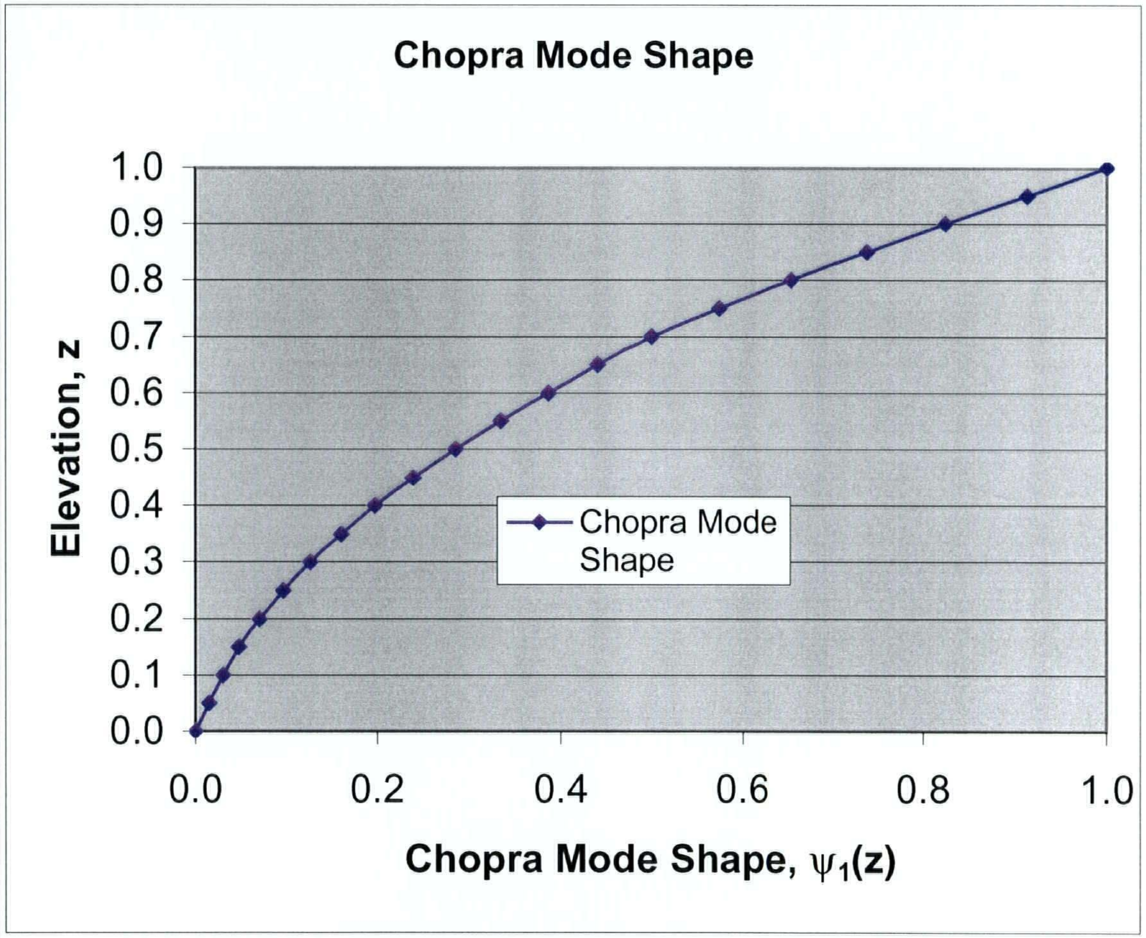

FIGURE 2-4: 2DOF Modal Analysis Worksheet, Gate 4, 7.4 Hz

2DOF Gate Hydrodynamic
10% Critical Damping
Basic Information

Evaluation of Added mass due to movement of dam and gate

DOF 1

DOF 2

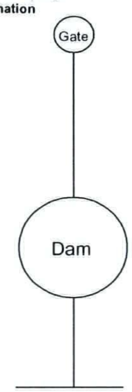

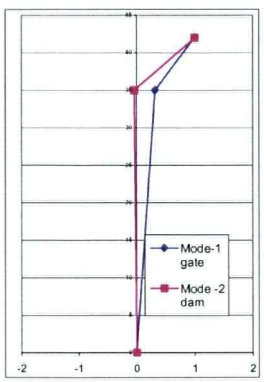

Elevation	Mode 1	Mode 2
42	1.000	1.000
35	0.088	-0.092
0	0	0

Geometric Amplification 1 1

Gate Mass: m_{g1} 30.5 tonne
Gate Stiffness: k_g 5.18E+05 kN/m

Gate Hydrodynamic Mass: μ_{g1} 208.93 tonne μ_{g2} 507.07
Gate Frequency: without added mass 20.75 Hz with added mass 4.19064400

Dam Mass: m_{d1} 19643.3 tonne
Dam Stiffness: k_d 5.89.E+07 kN/m

Dam Hydrodynamic Mass: μ_{d1} 9425.01 tonne μ_{d2} 507.07
Dam Frequency: without added mass 8.71 Hz with added mass 7.1000

Mass Matrix: $[m+\mu]$ $\begin{vmatrix} 239.4 & 507.1 \\ 507.1 & 29068.3 \end{vmatrix}$

Stiffness Matrix: $[k]$ $\begin{vmatrix} 5.175E+05 & -1.663E+06 \\ -1.663E+06 & 6.420E+07 \end{vmatrix}$ $[m+\mu]^{-1}$ 0.004337575 -7.5665E-05

$\det[k - \omega_n^2 m] = 0$

$(k_{11} - \omega_n^2 m_{11})(k_{22} - \omega_n^2 m_{22}) - (k_{12} - \omega_n^2 m_{12}) * (k_{21}.\omega_n^2 m_{21}) = 0$

$a\lambda 2 + b\lambda + c = 0$

a	6.70E+06	detM
b	-3.21E+10	cross determinant
c	3.05E+13	detK

$\lambda_1 = (-b - (b^2 - 4ac)^{1/2})/2a$

$\lambda_2 = (-b + (b^2 - 4ac)^{1/2})/2a$

Modal Expansion Factor, L

L $\begin{vmatrix} 1.00 \\ 1.00 \end{vmatrix}$ $= \alpha$ $= 1$

$[\mu_0]$ 643.2 10780.0

$[m]$ 30.5 0.0

$[m][L]+[\mu]$ 673.68 30423.32

$[L^*]$ 0.62 1.04

Frequencies: **Mode 1** λ_1 1304 rad/sec^2 ω1 5.75 Hz
Mode 2 λ_2 3.49E+03 rad/sec^2 ω2 9.40 Hz

Mode Shapes:

Mode 1 $[k - \lambda_1 m]$ $\begin{vmatrix} 2.05E+05 & -2.32E+06 \\ -2.32E+06 & 2.63E+07 \end{vmatrix}$ -8.84E-02 -8.84E-02

Determinant 0.00E+00

Eigenvectc ϕ_1 1.000 0.088

1	0.088	239.4
		507.1
1	0.088	239.4
		507.1

Mode 2 $[k - \lambda_2 m]$ $\begin{vmatrix} -3.17E+05 & -3.43E+06 \\ -3.43E+06 & -3.71E+07 \end{vmatrix}$ 9.24E-02 9.24E-02

Determinant -2.15E-02

Eigenvectc ϕ_2 1.000 -0.092

1	-0.092	239.4
		507.1
1	-0.092	239.4
		507.1

Participation Factors:

	f_n			$L^* = \phi_n^T mL$	$M = \phi_n^T m\phi_n$
Mode 1	5.75	Γ_1	6.047	3362.3	556.0
Mode 2	9.40	Γ_2	-5.43	-2137.3	393.8

Spectral Accelerations:

	f_n	P_n					
Mode 1	5.75	0.174	SA_1	0.910 g	8.93 m/sec^2	SV_1	0.247 m/sec
Mode 2	9.40	0.106	SA_2	0.730 g	7.16 m/sec^2	SV_2	0.121 m/sec
			PGA	0.540 g	5.30 m/sec^2		

Response Quantities:

	Displacements			Accelerations		
Mode 1	D_{g1}	0.0414	m	A_{g1}	54.0	m/sec^2
	D_{d1}	0.0037	m	A_{d1}	4.77	m/sec^2
Mode 2	D_{g2}	-0.0111	m	A_{g2}	-38.9	m/sec^2
	D_{d2}	0.0010	m	A_{d2}	3.6	m/sec^2

Use these values to find mode-1 and mode-
could scale and add from dam only and gat

FIGURE 2-5: Modified UHRS Curve, 10% Damping

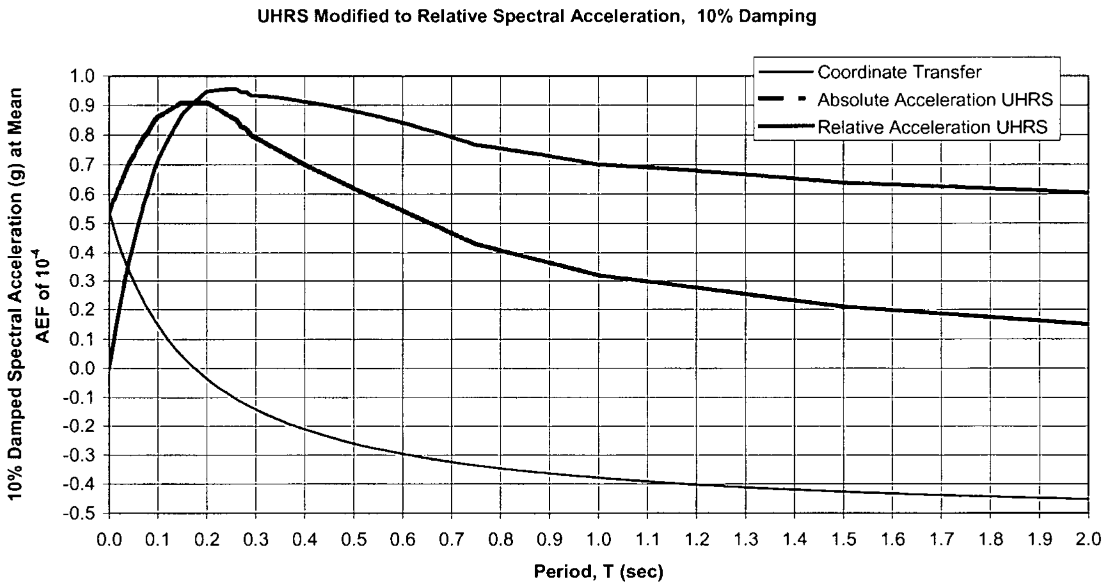

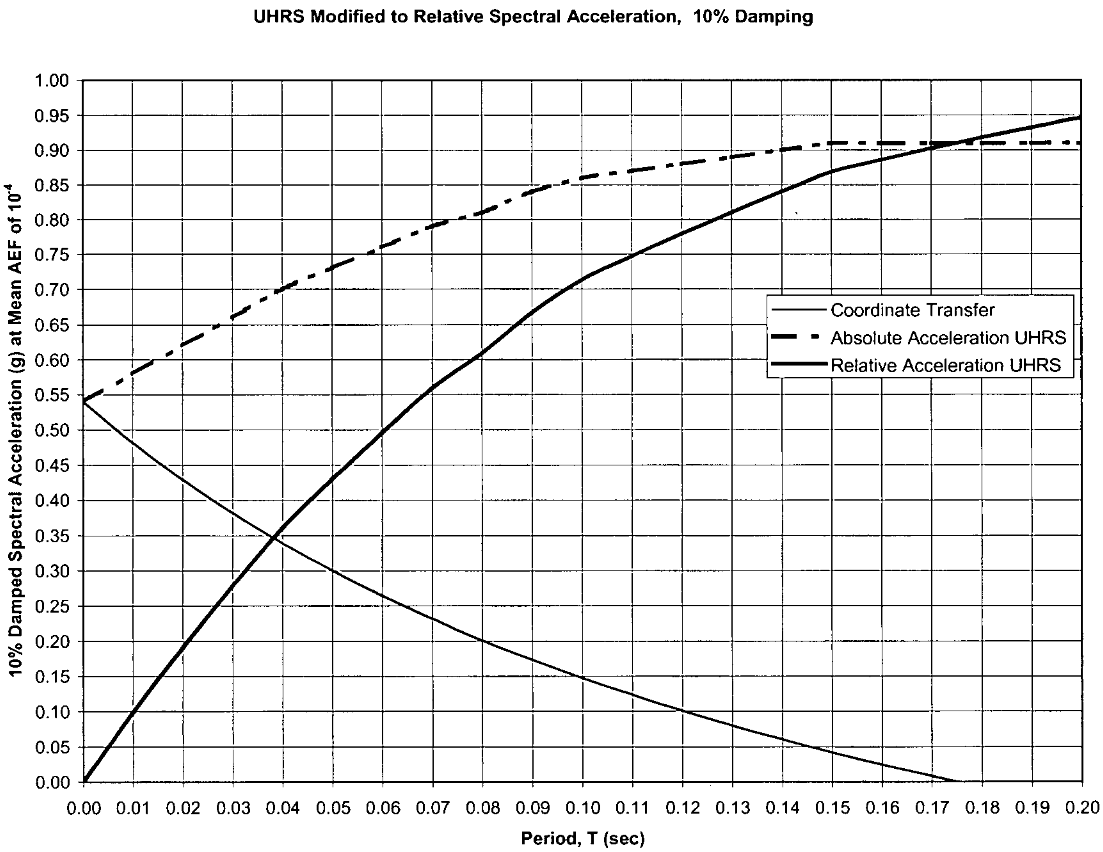

FIGURE 2-6: Effect of Varying Gate Frequency on Hydrodynamic Forces on Gate 4

Total Hydrodynamic Force on Gate 4
Considering the Effect of Varying Gate Stiffness, Constant Added Mass

Gate Mass, m_{g1} (tonnes)	Gate Added Mass due to Gate Motion, m_{gg} (tonnes)	Gate Added Mass due to Dam Motion, m_{gd} (tonnes)	Generalized Gate Stiffness, k_g (kN/m)	Gate Frequency, f_g (Hz)	Gate Period, T_g (sec)	Generalized Dam Mass, m_{d1} (tonnes)	Dam Added Mass due to Dam Motion, m_{dd} (tonnes)	Dam Added Mass due to Gate Motion, m_{dg} (tonnes)	Dam Stiffness, k_d (kN/m)	Dam Frequency, f_d (Hz)	Dam Period, T_d (sec)	Period Ratio	Acceleration of Pier at Water Level (42.91m)	Acceleration of Gate at Water Level (42.91m)	Total Force on Gate, F (kN)	Scaled Total Force on Gate, F* (kN)	Amplified Zangar Force on Gate (kN)	Kolkman Rigid Gate Force (kN)
30	209	507	2.95E+12	17659	5.66E-05	19643	9425	507	5.9E+07	7.10	0.14	**0.00**	26.51	26.51	**10398**	**11025**	**21685**	**11025**
30	209	507	2946903	17.66	0.06	19643	9425	507	5.9E+07	7.10	0.14	**0.40**	25.44	34.01	**11560**	**12257**	**21685**	**11025**
30	209	507	1443982	12.36	0.08	19643	9425	507	5.9E+07	7.10	0.14	**0.57**	24.05	42.31	**12834**	**13608**	**21685**	**11025**
30	209	507	736725	8.83	0.11	19643	9425	507	5.9E+07	7.10	0.14	**0.80**	21.52	57.97	**15180**	**16096**	**21685**	**11025**
30	**209**	**507**	**517520**	**7.40**	**0.14**	**19643**	**9425**	**507**	**5.9E+07**	**7.10**	**0.14**	**0.96**	**19.90**	**66.73**	**16099**	**17070**	**21685**	**11025**
30	209	507	471504	7.06	0.14	19643	9425	507	5.9E+07	7.10	0.14	**1.01**	19.67	68.12	**16098**	**17069**	**21685**	**11025**
30	209	507	265221	5.30	0.19	19643	9425	507	5.9E+07	7.10	0.14	**1.34**	22.13	66.17	**14155**	**15009**	**21685**	**11025**
30	209	507	117876	3.53	0.28	19643	9425	507	5.9E+07	7.10	0.14	**2.01**	25.96	47.42	**9666**	**10249**	**21685**	**11025**
30	209	507	29469	1.77	0.57	19643	9425	507	5.9E+07	7.10	0.14	**4.02**	27.38	33.82	**7055**	**7480**	**21685**	**11025**
30	209	507	3	0.02	56.63	19643	9425	507	5.9E+07	7.10	0.14	**402.08**	27.61	23.86	**5132**	**5442**	**21685**	**11025**

Total Force on Gate 4, 10% Damping, 0.54g PGA

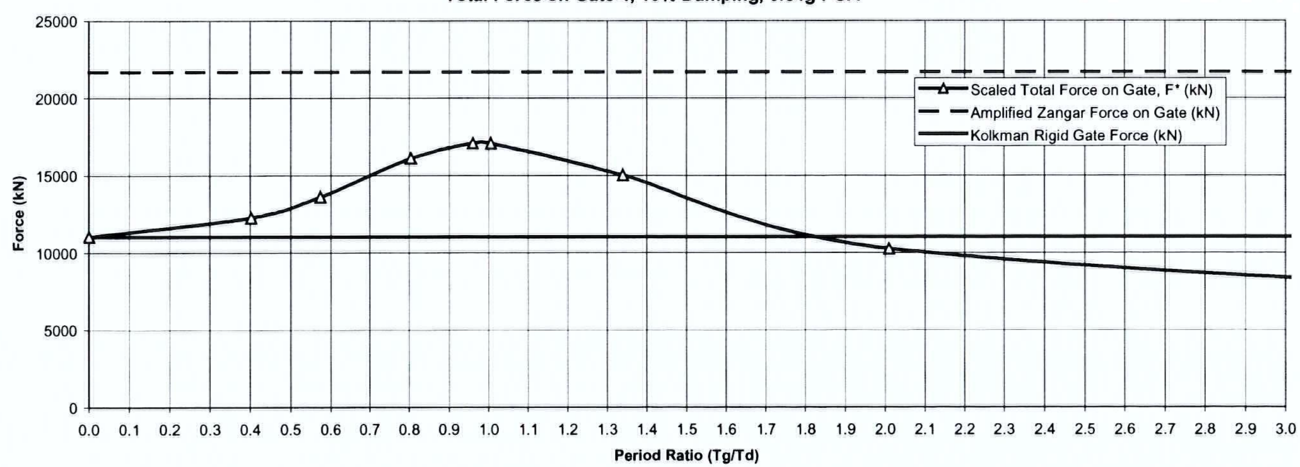

FIGURE 2-7: Summary of Hydrodynamic Gate Forces

	Gate 1	Gate 2	Gate 3	Gate 4	Gate 5	Gate 6	Gate 7
Kolkman 7.4Hz Gate Force (kN)	5074	7088	12867	16138	15821	13077	8296
Amplified Zangar Force on Gate (kN)	6024	9768	16948	21685	20912	15582	9419
Kolkman Rigid Gate Force (kN)	3632	5304	8727	10971	10607	8120	5241

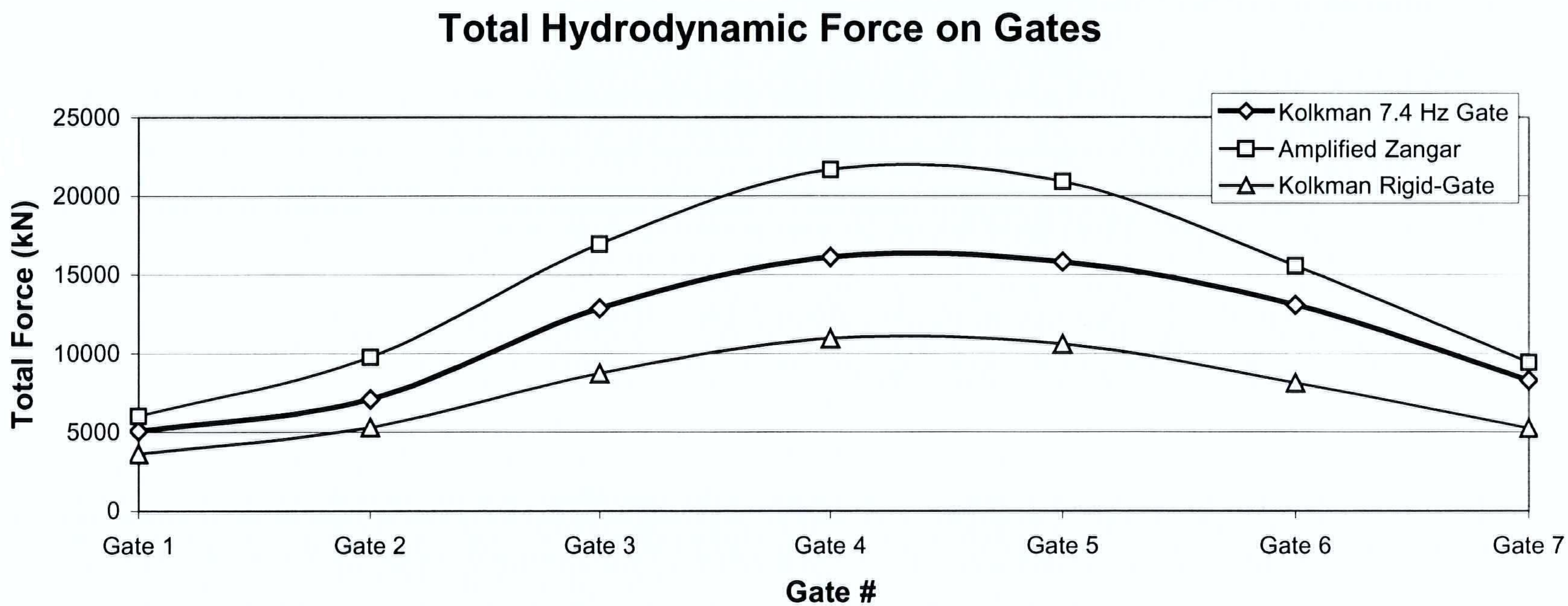

Chapter 3

Damping Study

3.0 INTRODUCTION

Structural damping is the capacity of a structure to absorb energy imposed on it by external forces, such as earthquake ground motions. In projects involving structures for which no structural damping value is provided, the damping value is assumed based on past experience and experimental results. In complex structural systems such as concrete gravity dams, it is beyond the scope of engineering to accurately compute structural damping. However, numerous attempts of providing reasonable estimates have been made.

The fundamental modal damping recommended by Chopra and Tan [4] is determined based on components of damping for the structure, reservoir and foundation in the following formula:

$$\zeta = \frac{1}{R_r} \frac{1}{\left(R_f\right)^3} \left(\zeta_1 + \zeta_r + \zeta_f\right) \qquad (3-1)$$

Where ζ_1 is the damping ratio of the dam on rigid foundation rock; ζ_r is the added damping ratio associated with the reservoir, a function of the reservoir bottom wave reflection coefficient; ζ_f is the added damping ratio associated with the dam/foundation interaction; R_r is the period modification ratio of the reservoir, a function of the reservoir depth and the modulus of the dam concrete;

R_f is the period modification ratio of the foundation flexibility, a function of the foundation flexibility and the hysteretic damping coefficient of the foundation material.

In a previous study of Ruskin Dam done for BCHydro in 1991 [17], a damping value of 10% was chosen after comparing damping recommended by Chopra for a number of possible combinations of structural parameters. PHC engineers calculated 16% damping using assumed parameters and noted that the damping value is sensitive to the foundation modulus and could be as low as 11%. PHC settled on 10% damping as a conservative assessment.

In the literature review for this topic, it was found that S. Okamoto, in his textbook titled, "Introduction to Earthquake Engineering" [14], states that damping values for dams in large earthquakes are likely to range from 10% to 20%.

In a very extensive paper by John Hall [8], the author describes the response of the Pacoima Dam in California to a near field earthquake. Data analysis indicates that damping in the order of 10% of critical is necessary to explain the motions experienced. Forced vibration tests indicated damping of 7.3% and 9.8% in closely spaced modes, symmetrical and anti-symmetrical, respectively. The bulk of U.S. and Chinese experience reports damping values ranging from 0.7% to about 5% based on shaker tests of existing structures. Japanese experience with actual earthquake data at Naramata Dam reported 8% to 10%

damping, while for Tsukabaru Dam, damping was reported to be greater than 10%. Other than that, the vast majority of damping results reported are within the range of 2% to 5%.

Based on these findings, the damping of concrete gravity dams could range anywhere from less than 1% to 20%. This lack of conclusive evidence makes it desirable to further investigate this topic. This study will test the Half-Power Bandwidth Method of estimating damping, using time history records obtained from real concrete gravity dam structures subjected to actual seismic ground motions.

3.1 BACKGROUND INFORMATION

3.1.1 Time History Records

There were two main criteria for selecting appropriate time histories for this damping study:

1. The structure is a concrete gravity dam structure
2. There are at least two coherent time history records, one at a "base" location (preferably at or near the dam base) and one at a "remote" location (preferably at or near the center crest)

It was also desirable to have strong ground motions (PGA > 0.1g), capable of causing significant amplification at the crest elevation.

For North American dams, several time history databases were searched, but only two structures satisfying the above criteria were found:

1. Detroit Dam, Oregon: 1993 Scotts Mills Earthquake
2. Lower Crystal Springs Dam, California: 1989 Loma Prieta Earthquake

Upon completion of the analyses of the North American dams, it was concluded that the ground motions were not representative of a theoretical Design Basis Earthquake, and it was deemed necessary to expand the study. Time history records for dams having experienced significant ground motions were found in a database compiled by the Japanese Commission on Large Dams (JCOLD) entitled, "Acceleration Records on Dam Foundations, No. 2" (2002). Due to the large amount of records found in this database, only those exhibiting the largest peak ground accelerations and peak response accelerations at the crest were extracted for this study:

1. Chiya Dam, Okayama Prefecture: 2000 Tottori Earthquake
2. Kashou Dam, Tottori Pref.: 2000 Tottori Earthquake
3. Ameyama Dam, Aichi Pref.: 1997 Aichi Earthquake
4. Takase Dam, Okayama Pref.: 2000 Tottori Earthquake
5. Tsuruda Dam, Kyushu: 1997 Kagoshima Earthquake
6. Sugesawa Dam, Chugoku: 1989 Tottori Earthquake
7. Hitokura Dam: 1995 Kobe Earthquake

Figure 3-1 shows the locations of these dams. Table 3-1 below summarizes the Peak Ground Acceleration, Peak Crest Response, and Amplification for each of the 9 dams considered.

TABLE 3-1: Summary of Peak Dam Responses

#	Dam Name	Peak Ground Acceleration (g)	Peak Response at Crest (g)	Amplification
1	Detroit Dam	0.026	0.150	5.8
2	Lower Crystal Springs Dam	0.052	0.070	1.3
3	Chiya Dam	0.073	0.546	7.5
4	Kashou Dam	0.538	2.091	3.9
5	Ameyama Dam	0.176	0.307	1.7
6	Takase Dam	0.108	0.377	3.5
7	Tsuruda Dam	0.158	0.723	4.6
8	Sugesawa Dam	0.037	0.204	5.5
9	Hitokura Dam	0.187	0.491	2.6

3.1.1.1 Detroit Dam

The Detroit Dam is a concrete gravity dam structure located in Detroit, Oregon. Time history records were available for the 1993 Scotts Mills Earthquake at the "Gallery Level 1" (Base) and "Gallery Level 7" (Remote) locations. The upstream-downstream Peak Ground Accelerations at the base and remote locations were 0.026g and 0.15g, respectively, indicating an amplification factor of about 6 between these locations.

3.1.1.2 Lower Crystal Springs Dam

The Lower Crystal Springs Dam is a concrete gravity dam structure located near San Mateo, California. Time history records were available for the 1989 Loma Prieta Earthquake at the "Dam Base" (Base), "Crest, Left 1/3 Length", and "Crest, Right 1/4 Length" (Remote) locations. Since the record from the center crest location was unavailable, two analyses were performed using the two available records corresponding to locations adjacent to the center crest. The upstream-downstream Peak Ground Accelerations at the base and remote locations were 0.052g and 0.07g (0.072g for Crest, Left 1/3 Length, and 0.069g for Crest, Right 1/4 Length), respectively, indicating an amplification factor of about 1.3 between the base and crest level locations.

3.1.1.3 Chiya Dam

The Chiya Dam is a concrete gravity dam structure located in Japan's Okayama prefecture. It is a local government dam monitored by the Ministry of Land, Infrastructure, and Transport. Time history records were available for the 2000 Tottori Earthquake at the foundation (Base) and center crest (Remote) locations. The upstream-downstream Peak Ground Accelerations at the base and remote locations were 0.073g and 0.546g, respectively, indicating an amplification factor of about 7.4 between these locations. Figure 3-2a shows the time history records for the Chiya Dam.

3.1.1.4 Kashou Dam

The Kashou Dam is a concrete gravity dam structure located in Japan's Tottori prefecture. It is a local government dam monitored by the Ministry of Land, Infrastructure, and Transport. Time history records were available for the 2000 Tottori Earthquake at the foundation (Base) and center crest (Remote) locations. The upstream-downstream Peak Ground Accelerations at the base and remote locations were 0.538g and 2.091g, respectively, indicating an amplification factor of about 3.9 between these locations. Figure 3-2b shows the time history records for the Kashou Dam.

3.1.1.5 Ameyama Dam

The Ameyama Dam is a concrete gravity dam structure located in Japan's Aichi prefecture. It is a local government dam monitored by the Ministry of Land, Infrastructure, and Transport. Time history records were available for the 1997 Aichi Earthquake at the foundation (Base) and center crest (Remote) locations. The upstream-downstream Peak Ground Accelerations at the base and remote locations were 0.176g and 0.307g, respectively, indicating an amplification factor of about 1.7 between these locations. Figure 3-2c shows the time history records for the Ameyama Dam.

3.1.1.6 Takase Dam

The Takase Dam is a concrete gravity dam structure located in Japan's Okayama prefecture. It was constructed in 1979 and is the second tallest dam structure in Japan at 577 ft. It is a local government dam monitored by the Ministry of Land, Infrastructure, and Transport. Time history records were available for the 2000 Tottori Earthquake at the foundation (Base) and center crest (Remote) locations. The upstream-downstream Peak Ground Accelerations at the base and remote locations were 0.108g and 0.377g, respectively, indicating an amplification factor of about 3.5 between these locations. Figure 3-2d shows the time history records for the Takase Dam.

3.1.1.7 Tsuruda Dam

The Tsuruda Dam is a concrete gravity dam structure located in Kyushu, Japan. It is a central government dam monitored by the Ministry of Land, Infrastructure, and Transport. Time history records were available for the 1997 Kagoshima Earthquake at the foundation (Base) and center crest (Remote) locations. The upstream-downstream Peak Ground Accelerations at the base and remote locations were 0.158g and 0.723g, respectively, indicating an amplification factor of about 4.6 between these locations. Figure 3-2e shows the time history records for the Tsuruda Dam.

3.1.1.8 Sugesawa Dam

The Sugesawa Dam is a concrete gravity dam structure located in Chugoku, Japan. It is a central government dam monitored by the Ministry of Land, Infrastructure, and Transport. Time history records were available for the 1989 Tottori Earthquake at the foundation (Base) and center crest (Remote) locations. The upstream-downstream Peak Ground Accelerations at the base and remote locations were 0.037g and 0.204g, respectively, indicating an amplification factor of about 5.6 between these locations. Figure 3-2f shows the time history records for the Sugesawa Dam.

3.1.1.9 Hitokura Dam

The Hitokura Dam is a concrete gravity dam structure located in Japan's Hyogo prefecture. It was constructed in 1982 by the Water Resources Development Public Corporation at the juncture of the Tajirigawa River and Hitokura-Orojigawa River. Time history records were available for the 1995 Kobe Earthquake at the foundation (Base) and center crest (Remote) locations. The upstream-downstream Peak Ground Accelerations at the base and remote locations were 0.187g and 0.491g, respectively, indicating an amplification factor of about 2.6 between these locations. Figure 3-2g shows the time history records for the Hitokura Dam.

3.1.2 Application of Half-Power Bandwidth Method to Complex Structures

In a Master's of Applied Science thesis by Mark Bakhtavar [3], the author provides experimental results that support the applicability of the Half-Power Bandwidth Method to multiple-degree-of-freedom (MDOF) systems such as multi-story high-rise structures. Bakhtavar used the signal processing program ME'scope [S2] to evaluate the vibration properties of the various buildings selected for data analysis. Given the input and response time history records, the ME'scope program evaluates the natural freuquencies, mode shapes and damping values. To verify the accuracy of the ME'scope results, Bakhtavar used the structural analysis program SAP90 [S3] to generate a 3D model with mass and stiffness properties representative of one of the structures analyzed in his study.

3.1.2.1 Background Information

The structure analyzed was a 6-story office building in Los Angeles, subjected to the 1994 Northridge Earthquake. Figure 3-3 shows the SAP90 model used in this study, a 6-story 3-D rigid frame with mass and stiffness properties that were selected such that its fundamental frequency was close to that of the actual structure. A mass eccentricity of 2.5–5.0% was assigned at each floor to allow for some degree of coupling between modes in different directions. The actual ground motion record at this building during the 1994 Northridge earthquake was used for a linear time history analysis of the model. The response time history records of the second, third and roof levels of the building were used by

ME'scope to determine the vibration properties of the system. A damping value of 5% was applied to all modes.

3.1.2.2 Calibration Results

Table 3-2 below shows the comparison between the SAP90 model results and the ME'scope results.

TABLE 3-2: Comparison of the Vibration Properties of the SAP90 Model and the Values Estimated Based on the Output Time Histories Using ME'scope

	SAP90 Model	ME'scope Analysis		ME'scope Analysis
Mode #	Frequency (Hz)	Frequency (Hz)	% Difference	Estimated Damping (%)
1	0.792	0.798	0.8%	4.59
2	0.864	0.861	0.3%	3.27
3	1.279	1.278	0.1%	3.05
4	2.169	2.178	0.4%	4.33
5	2.557	2.563	0.2%	4.10
6	3.467	3.369	2.9%	0.68
7	3.927	3.949	0.6%	4.02
8	4.226	4.239	0.3%	3.87
9	5.211	5.213	0.0%	3.32
10	5.887	5.822	1.1%	4.40
11	6.188	6.015	2.9%	3.20
12	6.900	6.907	0.1%	4.35
13	7.741	7.735	0.1%	3.08
14	8.407	7.897	6.5%	5.08
15	8.624	8.508	1.4%	2.03
16	8.850	8.768	0.9%	3.68
17	10.819	10.793	0.2%	3.10
18	13.215	13.184	0.2%	0.13

The results of this comparison show good agreement between the natural frequencies estimated by ME'scope and those calculated for the SAP90 model; the error was less than 3% for all but one of the frequencies. There was a much larger discrepancy in the estimated damping values; on average, the Half-Power Bandwidth damping values from the ME'scope results were about 2% less. This suggests that the reliability of the damping values estimated for strong motion data in this research is fairly reasonable. Accordingly, it is reasonable to apply the Half-Power Bandwidth Method to time history records from complex structural systems, such as the dam structures considered in this study.

3.2 METHODOLOGY

The Half-Power Bandwidth Method is used to approximate structural damping, given time history records from two different locations on a structure. In this study, this method was used to test the assumption of 10% damping. The damping value is an estimate of the energy dissipation due to all contributing resistant forces including the foundation, reservoir, and the structure itself.

First, cross spectrum analyses were performed on the compiled time history records for the dams discussed in Section 3.1. Second, the Half-Power Bandwidth damping values were computed from the Frequency Response Spectrum plots extracted from the cross spectrum analyses. Third, a sensitivity analysis was performed on some of the parameters used in the cross spectrum analysis to gain a better understanding of the calculations involved in this process.

3.2.1 MathCAD Spreadsheet Calculations

A MathCAD spreadsheet developed by C.E. Ventura was used to perform the spectral analysis calculations for the Half-Power Bandwidth Method (see Appendix B). Page 1 of the spreadsheet summarizes the time history records used in the analysis.

The sampling rate, sr, is the number of data points per second for the given record. The time step, Δ, is the reciprocal of the sampling rate, $1/sr$. The duration of the entire time history record, T, is given by:

$$T = \Delta(Nr - 1) \tag{3-3}$$

Where Nr is the number of data points in the record. The time history records for the base and remote sensor locations are represented by BA and RA, respectively. These are plotted at the bottom of page 1 with respect to time. The start and stop times of the record are adjusted based on the characteristics of the actual record. The start time is not $t = 0$ in cases for which the record does not experience significant excitation until a certain time, T_1.

Page 2 summarizes the portions of the record to be included in the analysis. A preliminary calculation of power spectra of the two raw time history records is presented at the bottom of Page 2. The input parameters for this calculation were the number of overlapping segments, nos, the overlapping factor, of, and the smooth factor, sm. By trial and error, it was determined that setting $nos = 2$ and $of = 0.99$ yielded optimal results; ie. the power spectrum was calculated for 2 overlapping segments, each encompassing 99% of the selected portion of the entire record. At first, a smooth factor of $sm = 3$ was used to produce a smoother FRF plot, from which the peaks could be identified. Later, a smooth factor of $sm = 1$ was used to extract a more realistic representation of the FRF plot.

3.2.2 The Half-Power Bandwidth Method

The Half-Power Bandwidth Method is a procedure used to approximate damping in structures with relatively low damping. For harmonic motions, there is one defined natural frequency which can be identified directly from the time history records. Since earthquake ground motions are transient, the natural frequencies cannot be determined directly from the input records. In order to solve this problem, the Fourier Transforms of the time history records of the ground motion and response of the system are used.

For SDOF systems subjected to harmonic excitation, the Half-Power Bandwidth damping is computed as follows:

$$\zeta_{HPBW} = \frac{f_b - f_a}{2f_n} \qquad (3-2)$$

Where f_a and f_b are the forcing frequencies on either side of the resonant frequency, f_n, on the Frequency Response Factor (FRF) plot, for which the amplitude of the FRF curve is equal to $\frac{FRF_{\max}}{\sqrt{2}}$. By inspection,

$$FRF_{\max} = FRF(f = f_n) \qquad (3-3)$$

The FRF, expressed as a function of frequency, is computed by performing a Fourier Transform of the power spectra of the time histories for the base and remote locations. The MathCAD spreadsheet presented in Section 3.2.1 was used to perform these calculations (see Appendix B).

The structures being analyzed in this study are not SDOF systems, nor are the ground motions harmonic. Therefore, it was necessary to justify the use of the Half-Power Bandwidth Method for estimating the damping in these complex structural systems. This justification, which was presented in Section 3.1.2, supports the applicability of the Half-Power Bandwidth Method to multiple-degree-of-freedom (MDOF) systems such as multi-story high-rise structures.

3.2.3 Sensitivity of MathCAD Analysis Parameters

For the records from the two dams in North America, a sensitivity analysis was performed to evaluate the effect of varying the smoothing factor, sm, and the portion of the record to be analyzed. Three different segments of the record were analyzed to check if any differences in the resulting FRF plots could be identified:

1. Entire Record: The entire record from t = 0
2. Forced Vibration: The portion of the record with significant ground motion
3. Free Vibration: The portion of the record from the end of significant ground motion

The purpose of this analysis was to test whether peaks in the FRF plots could be attributed to specific portions of the records. It was hypothesized that provided the ground motion was sufficient, the natural frequency of the system would appear in the Free Vibration component of the record. This behavior is expected because during the Forced Vibration component of the Record, the ground motion itself may interfere with the reactions at the base and remote accelerogram sensors. During the Free Vibration component, there is minimal interference and the sensors are more able to capture the natural damped vibration of the system.

3.3 DISCUSSION OF RESULTS

The North American dams were tested first. The Half-Power Bandwidth damping values of these records were found to be much lower than the original prediction of 10%. The Detroit Dam was found to have a Half-Power Bandwidth damping ranging from 0.2% to 1.2%. The Lower Crystal Springs Dam was found to have a Half-Power Bandwidth damping ranging from 0.1% to 0.6%. Some possible reasons for these low damping values are listed below:

1. The ground motions for the records were not strong enough to trigger inelastic response of the gravity dam system. As a result, the amount of energy dissipation, or damping, was minimal.
2. The peaks in the FRF plots were identified visually, because they were narrow, sharp, and easily identifiable by the human eye. For systems with 10% structural damping, the corresponding peaks in the FRF plots would have to be shorter and broader, in order to yield Half-Power Bandwidth damping values in the range of 10%. As a result, many of the true peaks may have gone undetected, since these peaks were too short to be easily identified in the FRF plot.
3. The Half-Power Bandwidth Method is useful for approximating natural frequencies and damping values for SDOF systems, but a more advanced analysis is required for systems as complex as gravity dams.

Since statements 2 and 3 question the reliability of the methodology used, it was decided to first test whether statement 1 was correct. To test whether the ground motions were not strong enough to trigger inelastic response of the gravity dam system, additional time history records from seven Japanese dams, each experiencing significant ground motions, were analyzed in the same manner as the Detroit Dam and Lower Crystal Springs Dam.

3.3.1 Detroit Dam

The Detroit Dam was found to have Half-Power Bandwidth damping values ranging from 0.2% to 1.2%. Table 3-3 summarizes the Half-Power Bandwidth damping values computed from the peaks identified on the FRF curves for the Detroit Dam time history records. This figure also shows a comparison of the values computed for the entire record to those calculated for the forced and free vibration components of the record. Figure 3-4a presents this comparison graphically, showing the plots for the three portions of the record within a set frequency range $(4.5Hz \leq f \leq 10Hz)$ within which the fundamental frequency of the structure is expected to be found. Certain peaks within this frequency range were identified as potential natural frequencies for the structure. Table 3-4 summarizes the agreement of the peaks in the FRF plot for the entire record with the Free and Forced Vibration components of the record.

TABLE 3-3: Detroit Dam – Half-Power Bandwidth Damping Summary

Mathcad File - Acceleration	detroit dam - 93sm - acc usds entire.mcd		
Raw Data Type	Corr. Accelerogram Data	Orientation:	US/DS
Station No.	2133A	Epicentral Distance (km):	45
Earthquake Name:	Scotts Mills	ML:	5.6
Earthquake Date + Time:	March 25, 1993, 01:34 PM PST	MS:	5.4

Station 1 - Base	**Gallery Level 1**		**Gallery Level 1**		**Gallery Level 1**		
Station 2 - Remote	**Gallery Level 7**		**Gallery Level 7**		**Gallery Level 7**		
Portion of Record	Entire		Free		Forced		
Start Time	4		10		4		
Stop Time	31.54		31.54		10		
Duration	27.54		21.54		6		
# Points	5509		4309		1201		
Time Interval (sec)	0.005		0.005		0.005		
No of Overlapping Segments,	2		2		2		
Overlapping Factor, of (0<of<1)	0.99		0.99		0.99		
Smoothing Factor, sm	**1**		**1**		**1**		
No. of Hanning Coefficients, NB	40		40		40		
Type of Record	Acceleration Time History		Acceleration Time History		Acceleration Time History		
Frequency	**Dominant Frequency**	**Peak FRF Value**	**Dominant Frequency**	**Peak FRF Value**	**Dominant Frequency**	**Peak FRF Value**	
f (Hz)	**f (Hz)**	**FRF_{max}**	**f (Hz)**	**FRF_{max}**	**f (Hz)**	**FRF_{max}**	**Best Estimate of Damping, ζ_1**
4.5					4.54	4.6	
4.6	4.63	8.2					
4.7							
4.8							
4.9							
5.0							
5.1			5.07	8.7			
5.2							
5.3	5.25	6.0	5.29	7.2			
5.4	5.35	5.8					
5.5			5.47	9.8			
5.6	5.57	8.7			5.57	7.6	
5.7							
5.8	5.77	6.5	5.82	16.7			
5.9	5.92	5.2	5.91	9.2			
6.0					6.04	5.2	
6.1	6.11	7.0	6.09	15.1			
6.2			6.20	14.2			
6.3			6.31	15.4			
6.4							
6.5	6.49	21.1					
6.6	6.60	48.5	6.62	53.1			
6.7	6.68	30.1					
6.8	**6.79**	**327.1**	**6.80**	**18.6**	**6.75**	**32.3**	**0.32%**
6.9	6.93	86.1	6.93	17.7			
7.0	7.01	11.0					
7.1			7.08	13.4			
7.2	7.15	10.1	7.27	29.4	7.22	6.5	
7.3			7.35	7.0			
7.4	7.36	7.3					
7.5			7.50	13.5			
7.6	7.55	10.6	7.64	9.6	7.60	8.3	
7.7	7.67	16.3					
7.8	7.77	4.8	7.83	7.9			
7.9	7.89	4.4					
8.0							
8.1							
8.2							
8.3	8.32	8.3	8.30	13.4			
8.4							
8.5							
8.6	8.58	6.7	8.58	17.3			
8.7	8.66	12.8					
8.8	8.77	10.7	8.81	8.8			
8.9	8.88	14.6					
9.0	8.99	13.4	9.04	7.6	8.97	6.4	
9.1			9.15	9.0			
9.2							
9.3							
9.4			9.38	14.0			
9.5	9.53	22.1	9.49	7.8	9.51	6.0	
9.6			9.61	6.9			
9.7							
9.8							
9.9							

TABLE 3-4: Detroit Dam: Agreement of Time History Record Components

f (Hz)	ζ_{HPBW}	Agreement with Free Vibration Component	Agreement with Forced Vibration Component
4.62	0.93%	No	No
5.57	1.15%	Yes	Not Clear
6.09	0.93%	Yes	No
6.49	0.40%	Not Clear	Not Clear
6.60	0.25%	Yes	Not Clear
6.68	0.44%	Not Clear	Not Clear
6.79	**0.17%**	**Yes**	**Not Clear**
6.93	0.17%	Yes	Not Clear
7.01	0.21%	No	Not Clear

Although the FRF plots for the Free and Forced Vibration components of the record are less clear, the peaks of the FRF plot for the entire record have a better fit to the FRF plot for the Free Vibration component. This may suggest that the Half-Power Bandwidth damping is more dependent on the Free Vibration component of the time history record.

The best estimate natural frequency for the Detroit Dam was selected as 6.79 Hz, which corresponds to the maximum peak Acceleration FRF result within the set frequency domain. The corresponding Half-Power Bandwidth damping value is 0.17%. This damping value is relatively low, due to the sharp, narrow shape of the Acceleration FRF curve at this point.

TABLE 3-5a: Lower Crystal Springs Dam, Right 1/4 Length Point – Half-Power Bandwidth Damping Summary

Mathcad File - Acceleration	lower crystal springs - 89lp - acc usds entire.mcd		
Raw Data Type	Corr. Accelerogram Data	Orientation:	US/DS
Station No.	58233	Epicentral	18
Earthquake Name:	Loma Prieta	ML:	7
Earthquake Date + Time:	October 17, 1989, 05:04 PM PST	MS:	7.1

Station 1 - Base	**Dam Base**		**Dam Base**		**Dam Base**		
Station 2 - Remote	**Crest, Right 1/4 - Length**		**Crest, Right 1/4 - Length**		**Crest, Right 1/4 - Length**		
Portion of Record	Entire		Free		Forced		
Start Time	6		22		6		
Stop Time	39.98		39.98		21.98		
Duration	33.98		17.98		15.98		
# Points	1700		900		800		
Time Interval (sec)	0.02		0.02		0.02		
No of Overlapping Segments,	2		2		2		
Overlapping Factor, of (0<of<1)	0.99		0.99		0.99		
Smoothing Factor, sm	1		1		1		
No. of Hanning Coefficients, NB	40		40		40		
Type of Record	Acceleration Time History		Acceleration Time History		Acceleration Time History		
Frequency	**Dominant Frequency**	**Peak FRF Value**	**Dominant Frequency**	**Peak FRF Value**	**Dominant Frequency**	**Peak FRF Value**	
f (Hz)	**f (Hz)**	**FRF_{max}**	**f (Hz)**	**FRF_{max}**	**f (Hz)**	**FRF_{max}**	**Best Estimate of Damping, ζ_1**
4.5							
4.6							
4.7							
4.8							
4.9							
5.0							
5.1	5.12	3.1					
5.2							
5.3							
5.4	5.38	7.6			5.37	4.4	
5.5							
5.6			5.56	7.8			
5.7							
5.8							
5.9							
6.0							
6.1	6.07	6.7					
6.2							
6.3							
6.4					6.44	3.9	
6.5			6.49	5.9			
6.6					6.65	3.7	
6.7	6.65	5.4					
6.8							
6.9					6.89	5.4	
7.0							
7.1			7.14	6.5			
7.2							
7.3							
7.4							
7.5	7.49	8.6			7.51	10.9	
7.6							
7.7			7.72	4.4			
7.8					7.85	6.9	
7.9							
8.0	**7.92**	**11.9**	**7.98**	**15.5**			**0.27%**
8.1			8.09	10.3			
8.2							
8.3			8.31	10.3	8.34	27.6	
8.4	8.41	11.7					
8.5							
8.6			8.58	11.0			
8.7	8.68	11.5			8.72	17.5	
8.8			8.79	3.2			
8.9	8.89	27.4			8.92	15.9	
9.0	8.98	16.1	9.04	9.4			
9.1	9.07	16.9					
9.2	9.28	17.2					
9.3	9.36	21.6	9.26	7.4			
9.4	9.42	61.9			9.36	13.6	
9.5	9.54	19.6			9.55	28.8	
9.6	9.66	20.6					
9.7	9.74	7.4	9.71	4.8	9.74	7.0	
9.8							
9.9	9.87	24.5					

TABLE 3-5b: Lower Crystal Springs Dam, Left 1/3 Length Point – Half-Power Bandwidth Damping Summary

Mathcad File - Acceleration	lower crystal springs - 89lp - acc usds entire.mcd		
Raw Data Type	Corr. Accelerogram Data	Orientation:	US/DS
Station No.	58233	Epicentral	18
Earthquake Name:	Loma Prieta	ML:	7
Earthquake Date + Time:	October 17, 1989, 05:04 PM PST	MS:	7.1

Station 1 - Base	Dam Base		Dam Base		Dam Base		
Station 2 - Remote	Crest, Left 1/3 - Length		Crest, Left 1/3 - Length		Crest, Left 1/3 - Length		
Portion of Record	Entire		Free		Forced		
Start Time	6		22		6		
Stop Time	39.98		39.98		21.98		
Duration	33.98		17.98		15.98		
# Points	1700		900		800		
Time Interval (sec)	0.02		0.02		0.02		
No of Overlapping Segments,	2		2		2		
Overlapping Factor, of (0<of<1)	0.99		0.99		0.99		
Smoothing Factor, sm	1		1		1		
No. of Hanning Coefficients, NB	40		40		40		
Type of Record	Acceleration Time History		Acceleration Time History		Acceleration Time History		
Frequency	**Dominant Frequency**	**Peak FRF Value**	**Dominant Frequency**	**Peak FRF Value**	**Dominant Frequency**	**Peak FRF Value**	
f (Hz)	**f (Hz)**	**FRF_{max}**	**f (Hz)**	**FRF_{max}**	**f (Hz)**	**FRF_{max}**	**Best Estimate of Damping, ζ_1**
4.5							
4.6					4.55	4.1	
4.7							
4.8							
4.9							
5.0	4.99	3.3	4.96	4.5	4.99	3.7	
5.1							
5.2							
5.3							
5.4	5.37	3.2					
5.5							
5.6			5.56	6.1			
5.7							
5.8			5.78	4.0			
5.9							
6.0							
6.1	6.07	8.1			6.07	4.5	
6.2							
6.3							
6.4	6.41	3.7			6.41	3.7	
6.5			6.47	10.8			
6.6	6.64	4.8			6.64	4.0	
6.7							
6.8	6.80	4.5					
6.9							
7.0	6.99	3.9					
7.1			7.13	6.2			
7.2							
7.3	7.31	8.3					
7.4							
7.5	7.46	4.9			7.52	8.5	
7.6	7.55	6.7					
7.7							
7.8					7.85	7.5	
7.9	7.90	7.2					
8.0	**8.03**	**12.0**	**7.98**	**13.1**			**0.28%**
8.1			8.09	6.7			
8.2							
8.3	8.32	12.1	8.32	9.7	8.35	19.9	
8.4	8.41	24.1					
8.5							
8.6	8.58	10.2	8.59	10.6	8.61	11.6	
8.7	8.70	10.0			8.72	19.0	
8.8			8.81	5.5			
8.9	8.89	38.2			8.90	19.3	
9.0	8.98	13.6	9.03	6.5			
9.1	9.07	16.0					
9.2							
9.3	9.27	20.0			9.32	17.5	
9.4	9.36	23.4	9.44	5.1			
9.5	9.42	67.7					
9.6	9.54	24.7			9.55	34.0	
9.7	9.66	39.3			9.73	16.2	
9.8	9.74	16.8					
9.9	9.87	31.2					

3.3.2 Lower Crystal Springs Dam

The Lower Crystal Springs Dam was found to have Half-Power Bandwidth damping values ranging from 0.1% to 0.6%. Tables 3-5a and 3-5b summarize the Half-Power Bandwidth damping values computed from the peaks identified on the FRF curves for the Lower Crystal Springs Dam time history records, using the "Crest, Right 1/4 Length" and "Crest, Left 1/3 Length" points, respectively. These figures also show a comparison of the values computed for the entire record to those calculated for the forced and free vibration components of the record. Figures 3-5a and 3-5b present the comparisons graphically, showing the plots for the three portions of the record within a set frequency range $(4.5Hz \leq f \leq 10Hz)$ within which the fundamental frequency of the structure is expected to be found. Certain peaks within this frequency range were identified as potential natural frequencies for the structure. Tables 3-6a and 3-6b below summarize the agreement of the peaks in the FRF plot for the entire record with the Free and Forced Vibration components of the record.

TABLE 3-6a: Lower Crystal Springs Dam – Crest, Right 1/4 Length Point: Agreement of Time History Record Components

f (Hz)	ζ_{HPBW}	Agreement with Free Vibration Component	Agreement with Forced Vibration Component
5.38	0.24%	Yes	Yes
6.07	0.25%	Not Clear	Yes
7.49	0.59%	No	Yes
7.92	**0.30%**	**Yes**	**Yes**
8.41	0.22%	No	Yes
8.68	0.20%	No	Yes
8.89	0.15%	No	Yes
8.98	0.21%	No	Yes
9.07	0.13%	Yes	No

TABLE 3-6b: Lower Crystal Springs Dam – Crest, Left 1/3 Length Point: Agreement of Time History Record Components

f (Hz)	ζ_{HPBW}	Agreement with Free Vibration Component	Agreement with Forced Vibration Component
6.07	0.21%	Yes	Yes
7.31	0.21%	No	Yes
7.55	0.36%	Yes	Yes
7.90	0.18%	No	Not Clear
8.03	**0.16%**	**No**	**Yes**
8.32	0.14%	Yes	Yes
8.41	0.13%	No	No
8.58	0.28%	Yes	Yes
8.70	0.56%	No	Not Clear

For the Lower Crystal Springs Dam records, the peaks of the FRF plot for the entire record do not fit to either the Free or Forced Vibration components. However, there are certain frequencies at which there is good agreement between the plots, and indicate the possibility of these being natural frequencies of the system.

Figure 3-5c shows the FRF plots for the Crest-Right and Crest-Left time history analyses. The two FRF plots are very similar in that most of the peaks are duplicated in both plots. This is as expected, since both sensor locations are adjacent to each other, on either side of the center crest. Table 3-7 below summarizes the Half-Power Bandwidth damping values for the FRF peaks for the Crest-Right and Crest-Left time history records.

The best estimate natural frequency for the Lower Crystal Springs Dam was selected as 8.00 Hz, which corresponds to one peak which was apparent in both the Crest-Left and Crest-Right Acceleration FRF plots. The corresponding Half-Power Bandwidth damping value is approximately 0.28%. This damping value is relatively low, due to the sharp, narrow shape of the Acceleration FRF curve at this point.

TABLE 3-7: Lower Crystal Springs Dam: Comparison of Half-Power Bandwidth Damping Values for Crest-Right and Crest-Left Components

f (Hz)	ζ_{HPBW} for Crest, Right 1/4 Length Point	ζ_{HPBW} for Crest, Left 1/3 Length Point	Difference
5.38	0.25%	0.61%	0.36%
6.75	0.31%	0.37%	0.05%
6.90	0.14%	0.25%	0.11%
6.97	0.50%	0.62%	0.12%
7.28	0.27%	0.30%	0.03%
7.48	0.11%	0.11%	0.00%
7.91	**0.16%**	**0.29%**	**0.12%**
8.89	0.10%	0.09%	0.00%
8.97	0.12%	0.12%	0.00%
9.42	0.15%	0.13%	0.02%
9.55	0.12%	0.11%	0.01%
9.60	0.15%	0.12%	0.03%

3.3.3 Sensitivity of Smoothing Factor

The smoothing factor, sm, was used primarily for identifying peaks on the FRF plots. Figure 3-4b presents a comparison of two FRF plots for the Detroit Dam records; one having $sm = 3$, the other having $sm = 1$. By inspection, the FRF curve for $sm = 3$ is much smoother than for $sm = 1$, with peaks that are less sharp. Also, it was found that the Half-Power Bandwidth damping values were in the order of 3 times larger than those for $sm = 1$. This was probably the direct effect of the smoothing factor creating shorter and broader peaks in the FRF plots. Table 3-8 below summarizes the ratio of mean Half-Power Bandwidth damping values for $sm = 3$ and $sm = 1$.

TABLE 3-8: Effects of Varying Smoothing Factor

#	Dam Record	$(\zeta_{HPBW})_{avg}$ for sm=1	$(\zeta_{HPBW})_{avg}$ for sm=3	Ratio
1	Detroit Dam	0.5%	1.1%	2.2
2a	Lower Crystal Springs Dam – Right	0.2%	0.6%	3.9
2b	Lower Crystal Springs Dam – Left	0.2%	0.5%	2.3
3	Chiya Dam	0.3%	0.7%	2.3
4	Kashou Dam	1.0%	N/A	N/A
5	Ameyama Dam	0.3%	0.8%	2.4
6	Takase Dam	0.2%	0.4%	2.2
7	Tsuruda Dam	0.6%	0.7%	1.1
8	Sugesawa Dam	0.5%	N/A	N/A
9	Hitokura Dam	1.4%	2.1%	1.5

3.4 CONCLUSIONS

An analytical study involving the Half-Power Bandwidth method of estimating damping in concrete gravity dams was performed successfully. The objectives of this study were to test this method of evaluating structural damping and to recommend a reasonable estimate of structural damping in concrete gravity dams. The conclusions that can be made from this study are as follows.

3.4.1 Regarding the Cross Spectrum Analysis

- The MathCAD worksheet employed mathematically sound formulae to perform the cross spectrum computations for the subsequent analyses in study.
- The peaks in the FRF plots were identified visually. As a result, only those peaks exhibiting sharp, narrow characteristics could be identified. It is possible that many peaks were undetected, due to their shape (short and broad) and location in the FRF plots. Such peaks are expected to have larger damping values when formulated by the Half-Power Bandwidth Method.

3.4.2 Regarding the Half-Power Bandwidth Method

- The Half-Power Bandwidth Method is a mathematical procedure used to calculate damping for SDOF damped systems subjected to harmonic excitation. It is unknown whether this method is applicable to a structural system with the complexity of a concrete gravity dam.

- The damping values computed by the Half-Power Bandwidth Method were found to be much lower than expected (less than 2%) and therefore, unrepresentative of the actual damping present in the concrete gravity dams analyzed in this study.

3.4.3 Regarding the Estimated Damping Values

- The estimated damping values calculated by the Half-Power Bandwidth Method were lower than the expected value of 5-10%. Due to relatively low Peak Ground Accelerations for the time history records (PGA < 0.2g for all dams except for Kashou), this result is as expected. It was concluded that damping exhibited by a structure is proportional to the level of ground excitation during an earthquake, and that 10% damping is possible in structures subjected to larger Peak Ground Accelerations (PGA > 1g).
- There were problems associated with the identification of natural frequencies, or peaks in the FRF plots, since the only peaks selected for analysis were tall, sharp peaks, representative of components of the structure with little or no damping. Alternatively, the shorter, broader peaks did not extend past the upper envelope of the FRF plots, and therefore were not easily identifiable.

3.5 RECOMMENDATIONS

There is a wide variety of work that could be done in continuation of this study. Some recommendations for future work on this topic are:

1. Investigation into other methods of calculating or approximating damping for complex structural systems (MDOF).
2. More detailed numerical analysis to allow for easier identification of natural frequencies in the FRF plots.
3. Complementary structural analysis (Finite Element Modeling) to provide additional verification of the damping formulation methods. This would require creating a 3D model given some initial damping value, applying a ground motion, analyzing the responses of the base and crest locations, plotting the FRF, identifying possible natural frequencies, estimating the damping, and comparing the resulting damping with the damping initially entered in the model.

FIGURE 3-1: Location of Japanese Dams

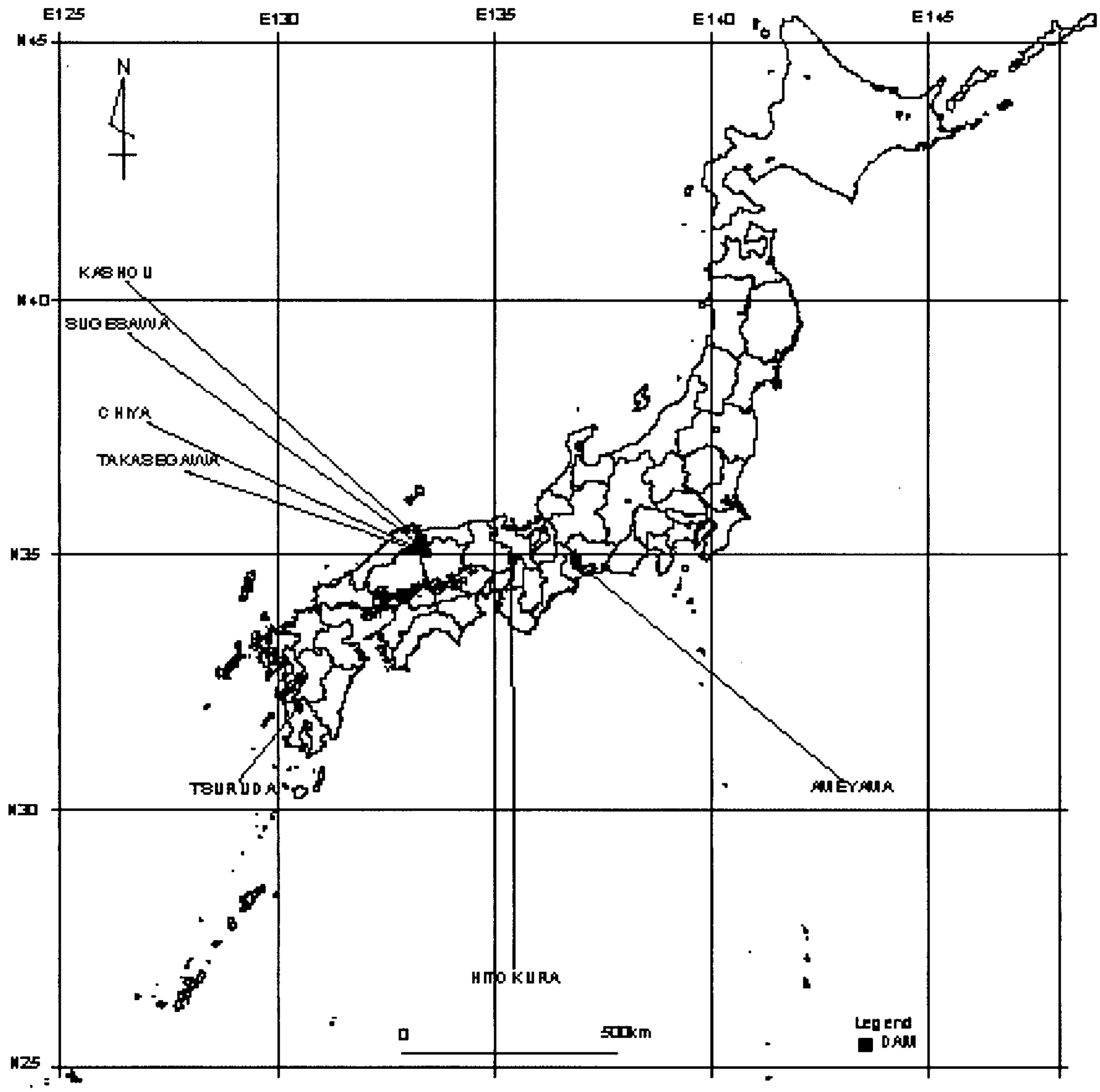

FIGURE 3-2a: Chiya Dam – Recorded Motions at Crest (T1) and Foundation (F1)

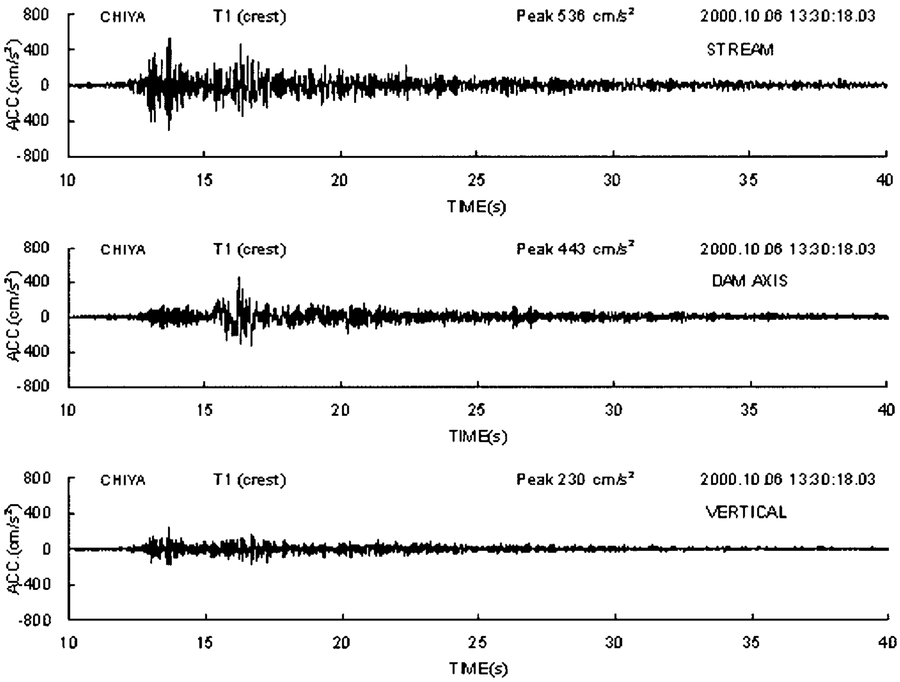

No29 CHIYA (2000.10.06 13:30:18.03WESTERN TOTTORI PREF)

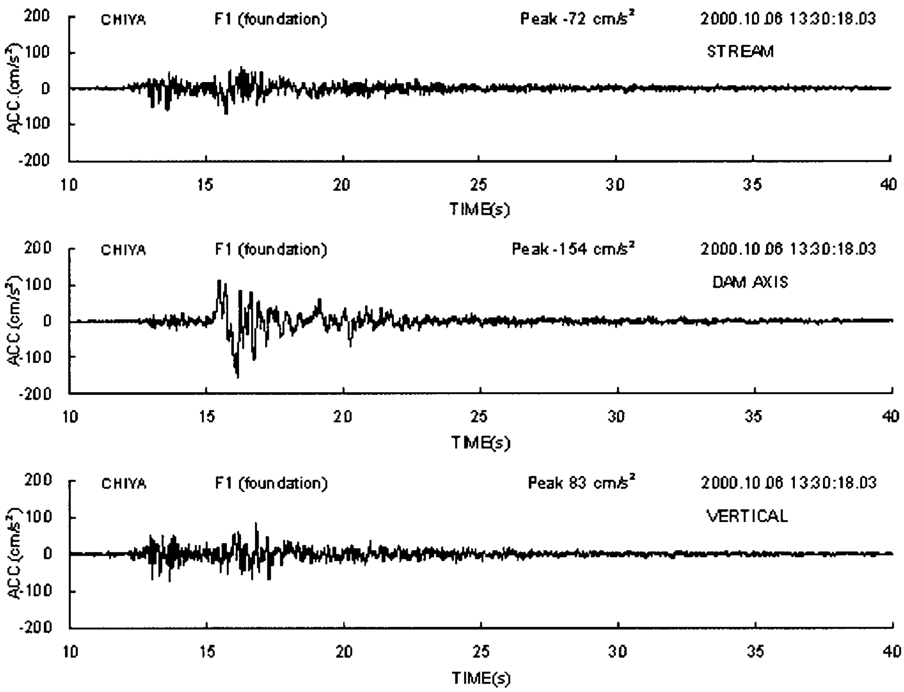

No30 CHIYA (2000.10.06 13:30:18.03WESTERN TOTTORI PREF)

FIGURE 3-2b: Kashou Dam – Recorded Motions at Crest (T1) and Foundation (F1)

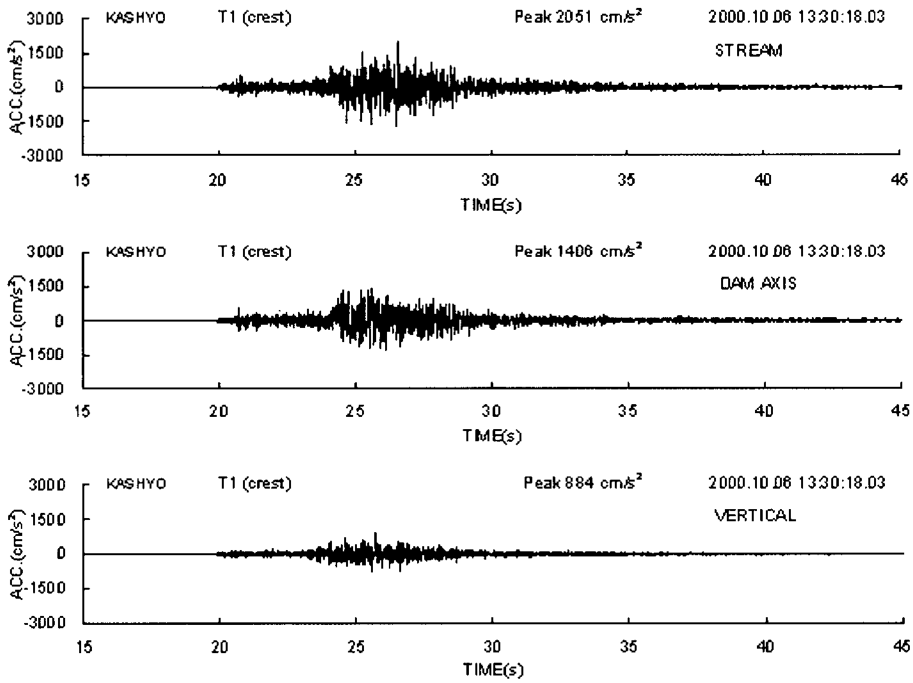

No.27 KASHYO (2000.10.06 13:30:18.03WESTERN TOTTORI PREF)

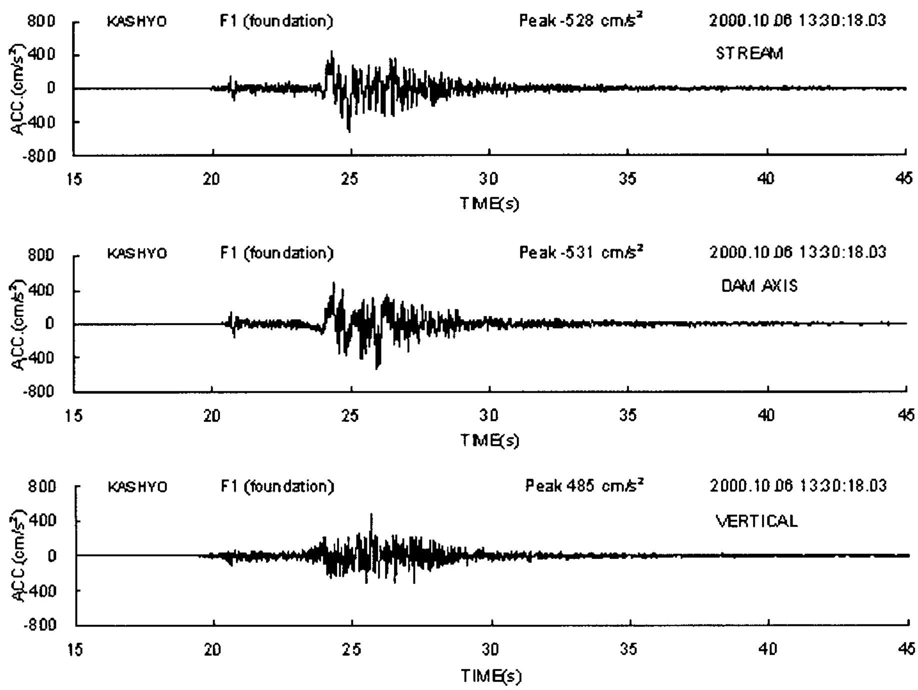

No.28 KASHYO (2000.10.06 13:30:18.03WESTERN TOTTORI PREF)

FIGURE 3-2c: Ameyama Dam – Recorded Motions at Crest (T1) and Foundation (F1)

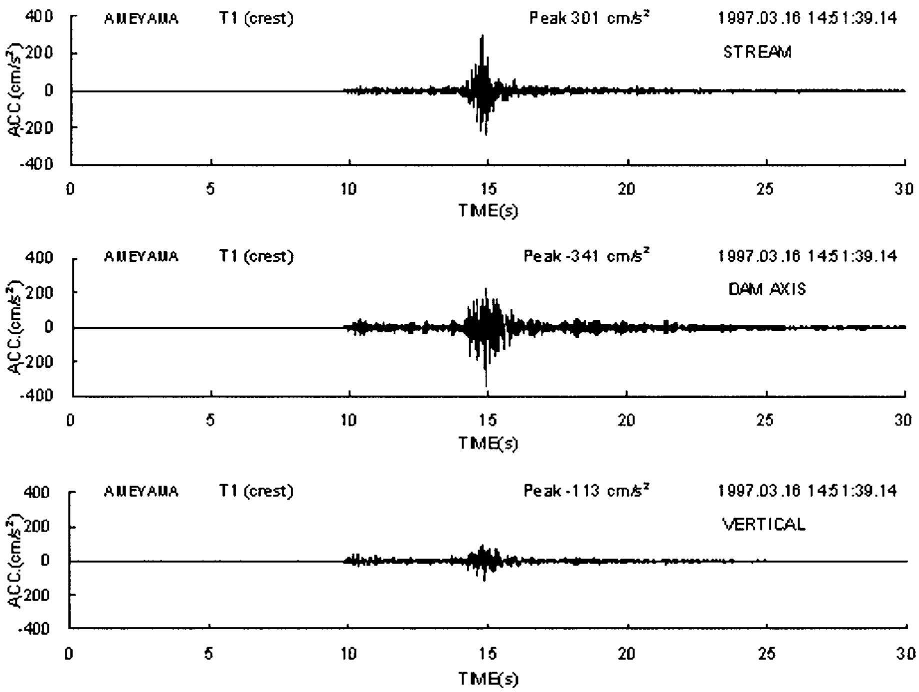

No.17 AMEYAMA (1997.03.16 14:51:39.14 NE AICHI PREF)

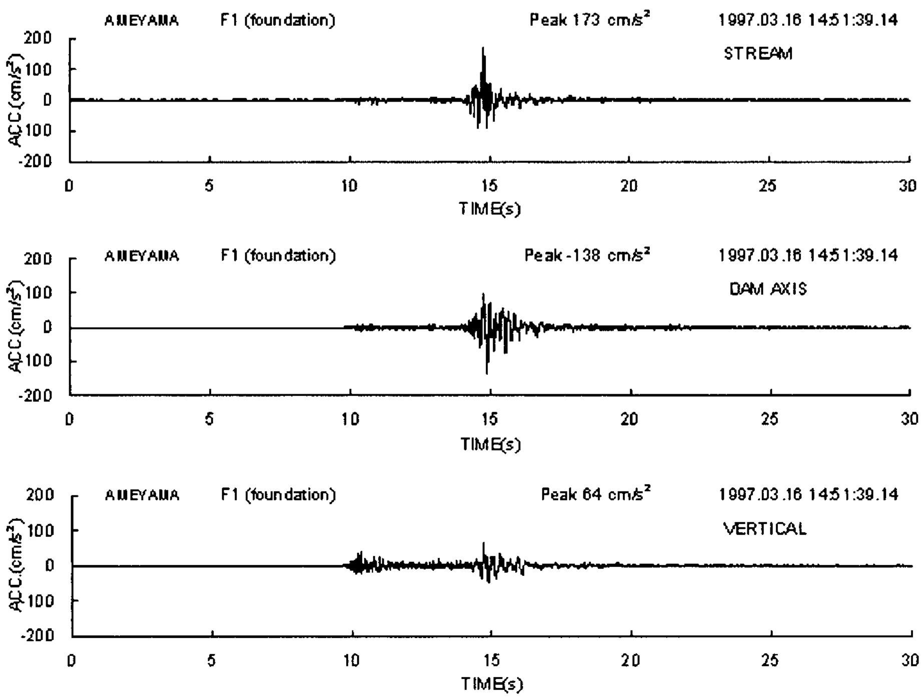

No.18 AMEYAMA (1997.03.16 14:51:39.14 NE AICHI PREF)

FIGURE 3-2d: Takase Dam – Recorded Motions at Crest (T1) and Foundation (F1)

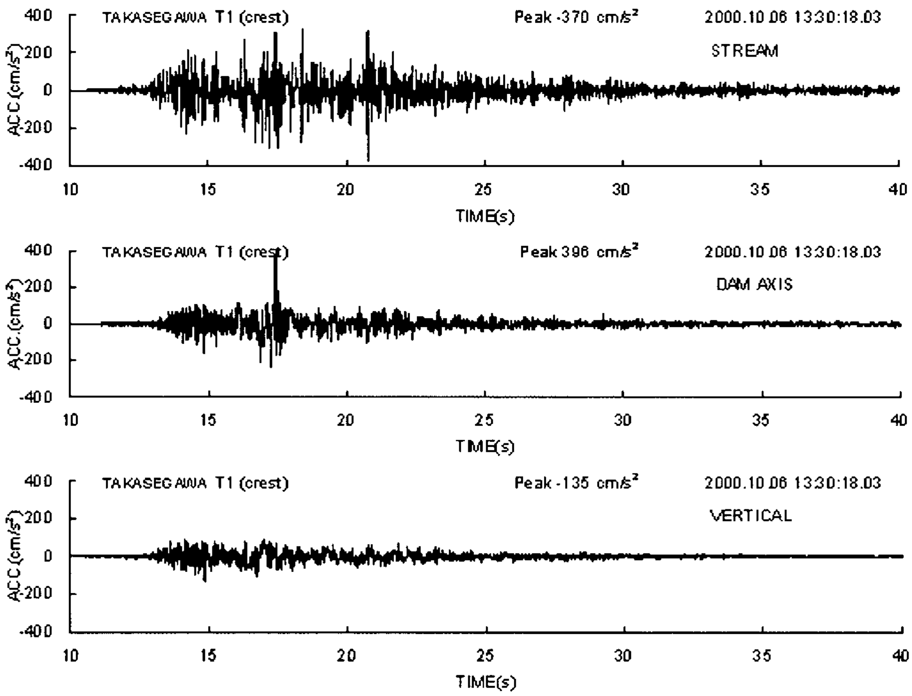

No.29 TAKASEGAWA (2000.10.06 13:30:18.03 WESTERN TOTTORI PREF)

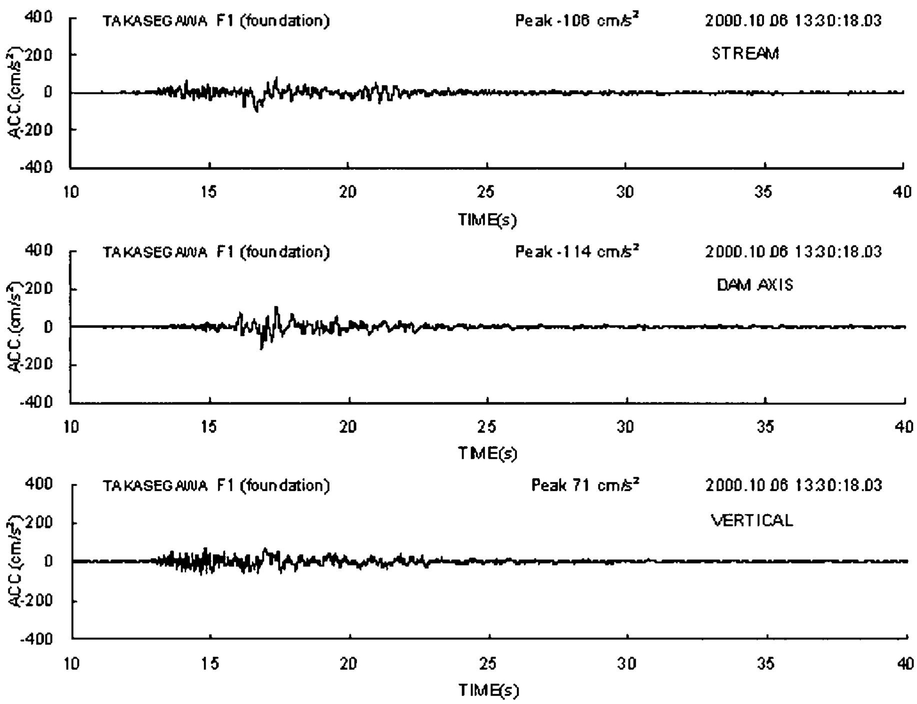

No.30 TAKASEGAWA (2000.10.06 13:30:18.03 WESTERN TOTTORI PREF)

FIGURE 3-2e: Tsuruda Dam – Recorded Motions at Crest (T1) and Foundation (F1)

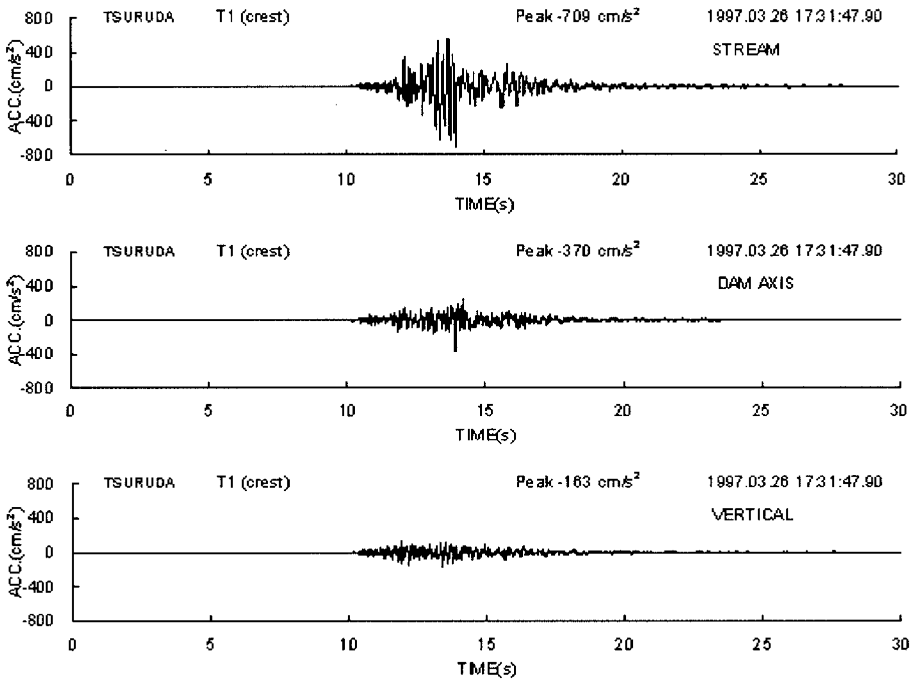

No.19 TSURUDA (1997.03.26 17:31:47.90 NW KAGOSHIMA PREF)

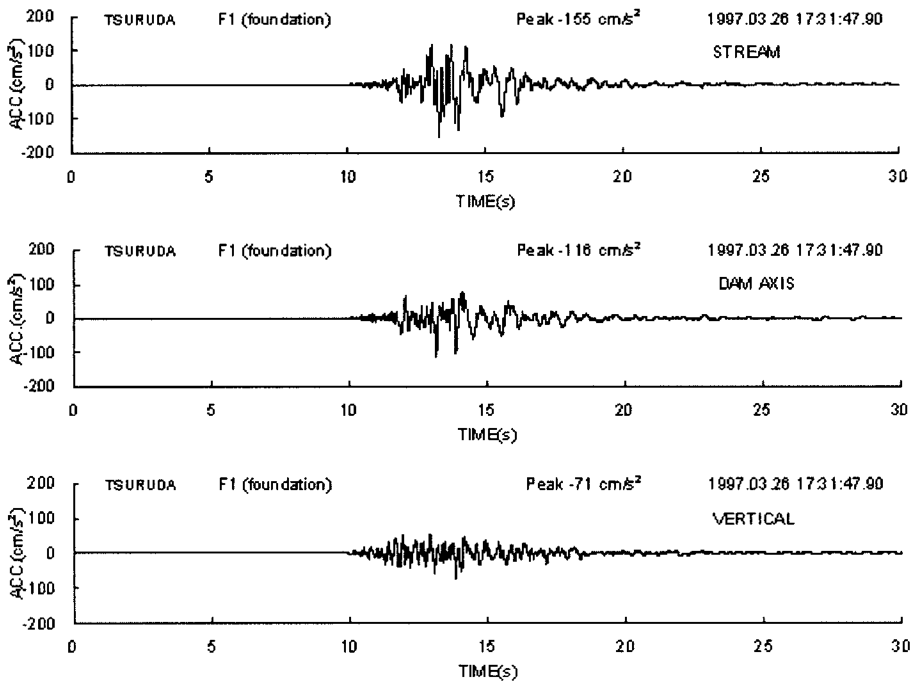

No.20 TSURUDA (1997.03.26 17:31:47.90 NW KAGOSHIMA PREF)

FIGURE 3-2f: Sugesawa Dam – Recorded Motions at Crest (T1) and Foundation (F1)

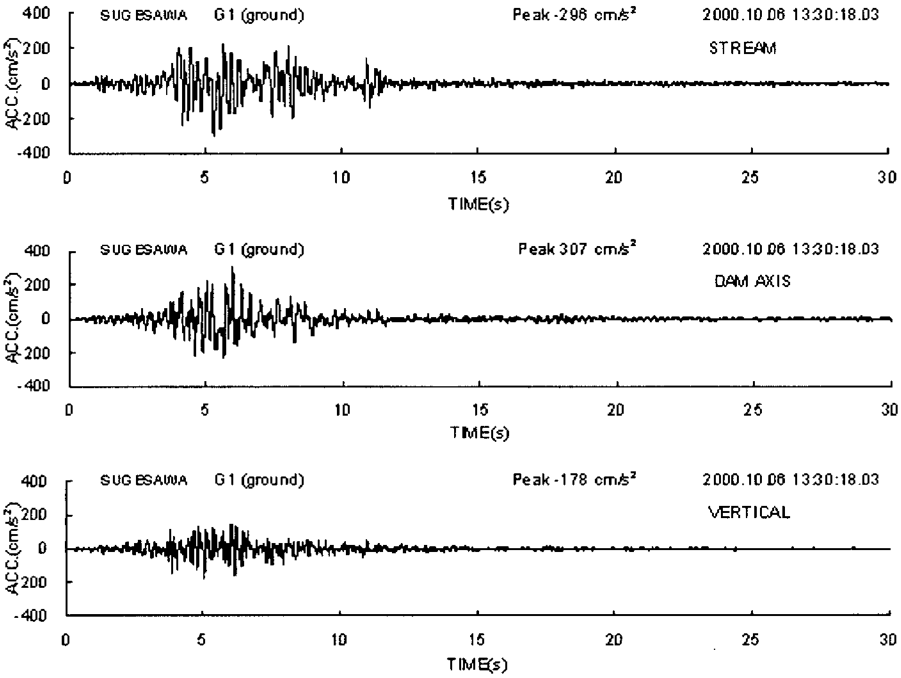

No.25 SUGESAWA (2000.10.06 13:30:18.03 WESTERN TOTTORI PREF)

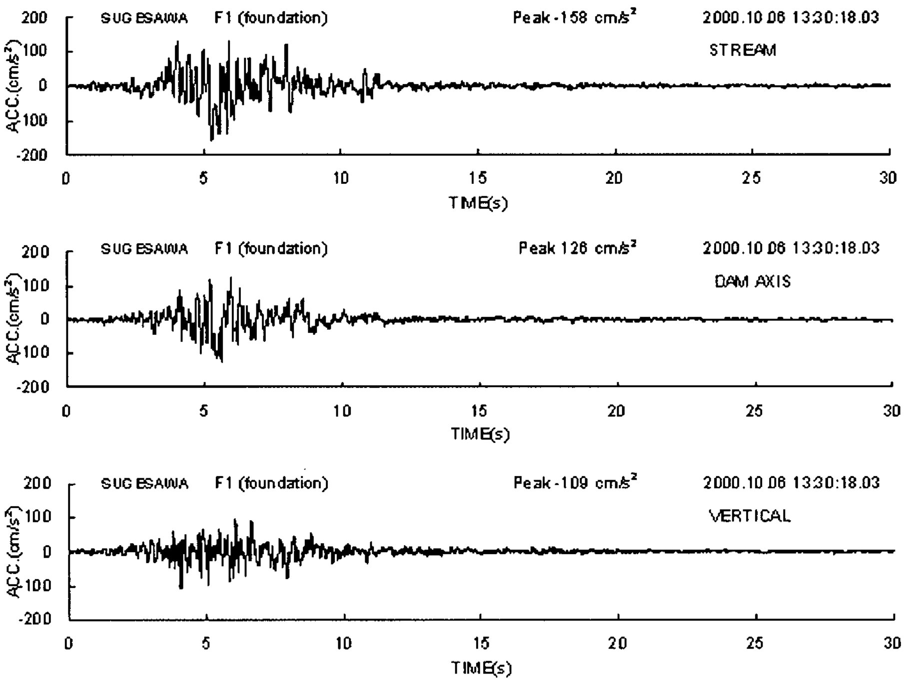

No.26 SUGESAWA (2000.10.06 13:30:18.03 WESTERN TOTTORI PREF)

FIGURE 3-2g: Hitokura Dam – Recorded Motions at Crest (T1) and Foundation (F1)

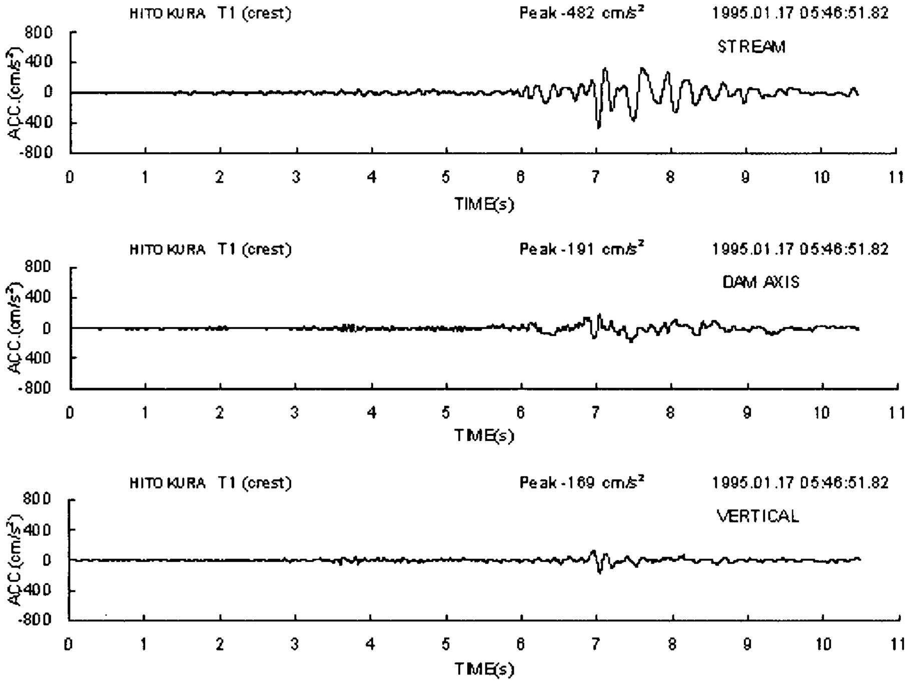

No.13 HITOKURA (1995.01.17 05:46:51.82 AWAJISHIMA ISLAND REGIO)

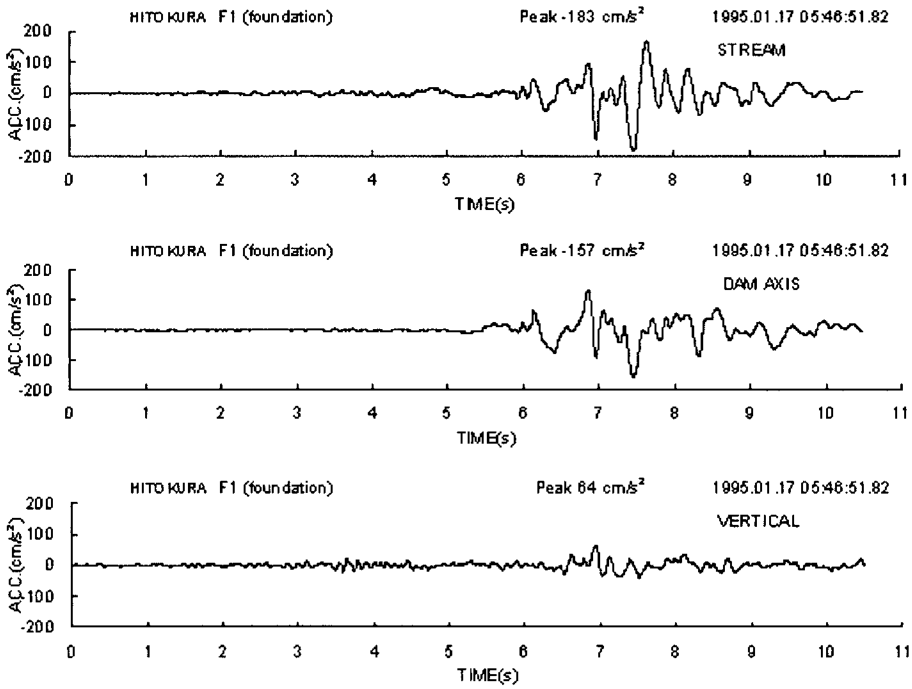

No.14 HITOKURA (1995.01.17 05:46:51.82 AWAJISHIMA ISLAND REGIO)

FIGURE 3-3: SAP Model of 6-Story 3-D Rigid Frame

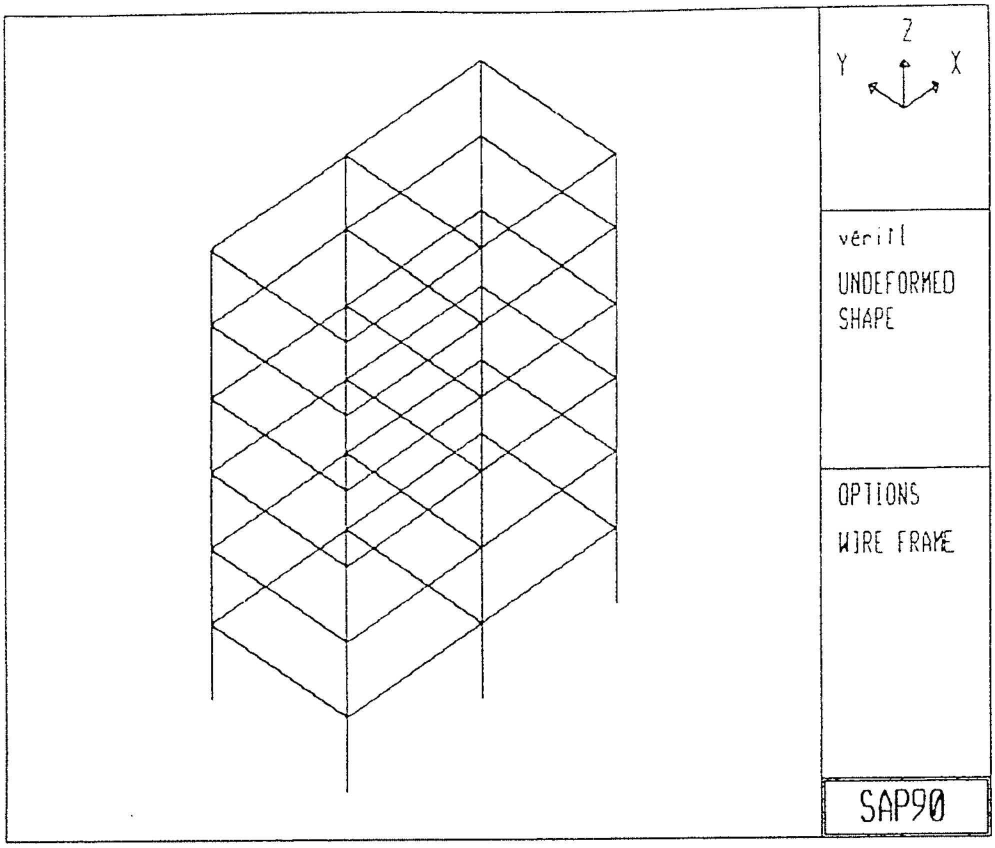

FIGURE 3-4a: Detroit Dam: Comparison of FRF Plots for Various Components of Time History Record

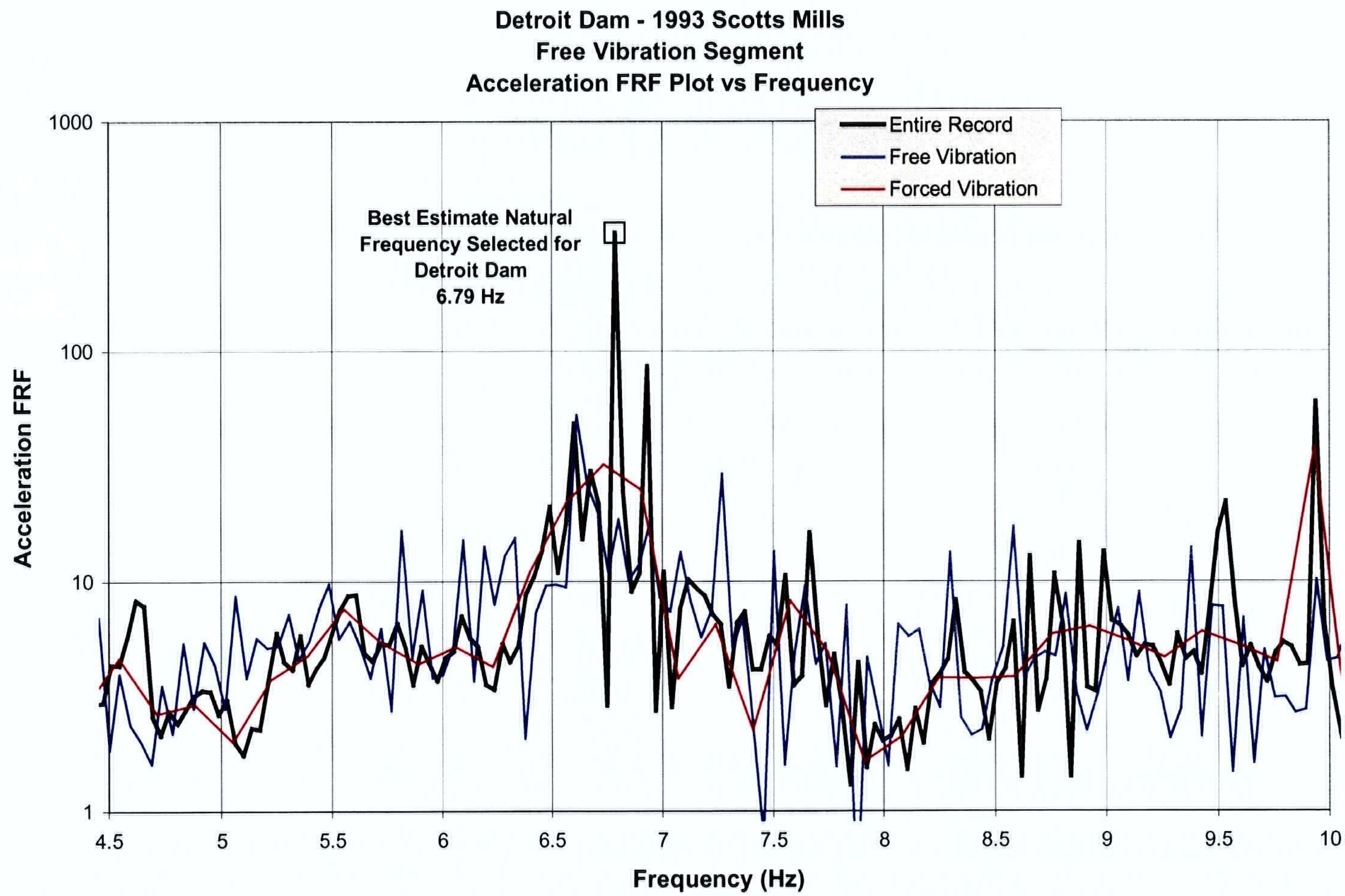

FIGURE 3-4b: Detroit Dam: Comparison of FRF Plots for Various Smoothing Factors (sm)

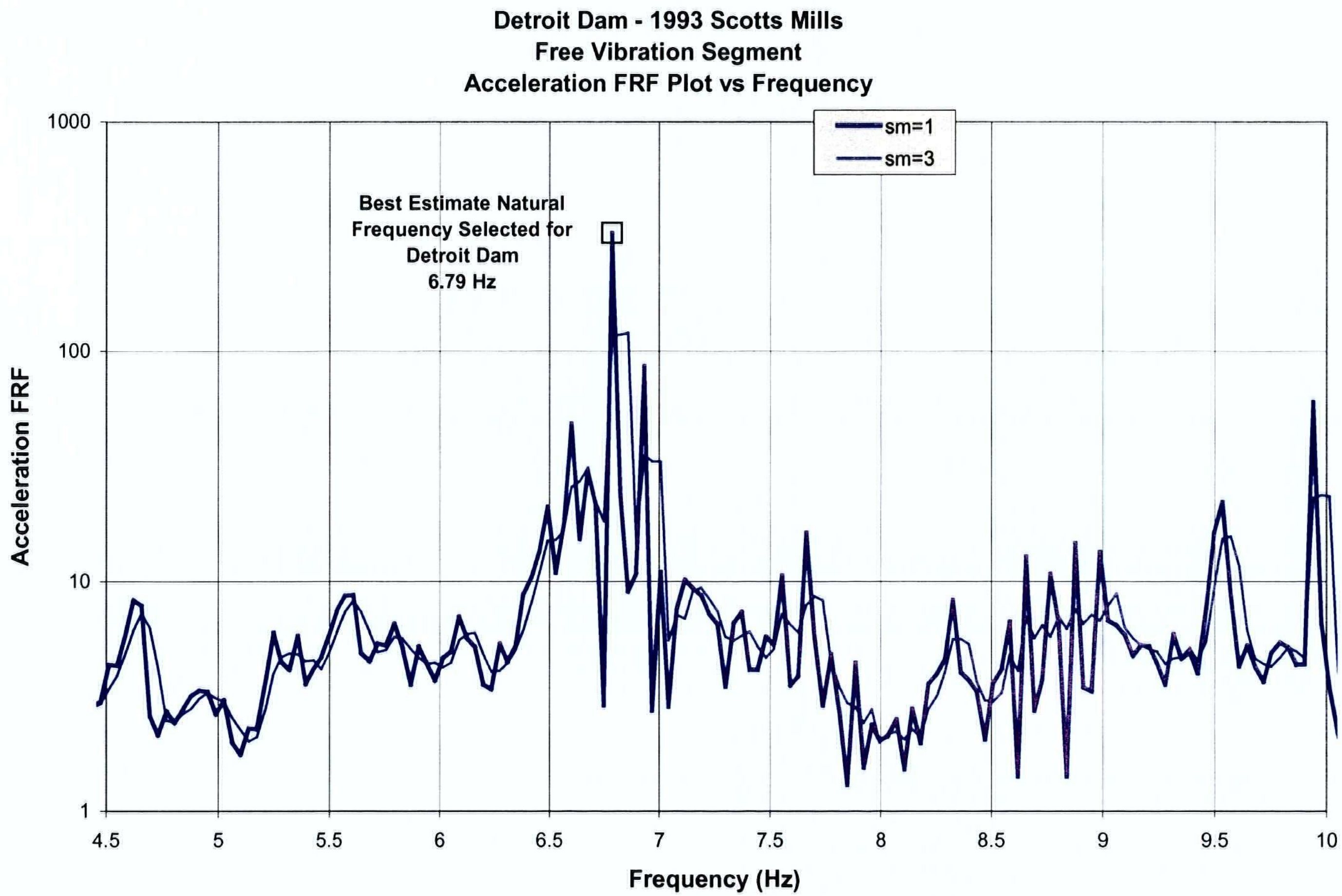

FIGURE 3-5a: Lower Crystal Springs Dam – Crest, Right 1/4 Length Point: Comparison of FRF Plots for Various Components of Time History Record

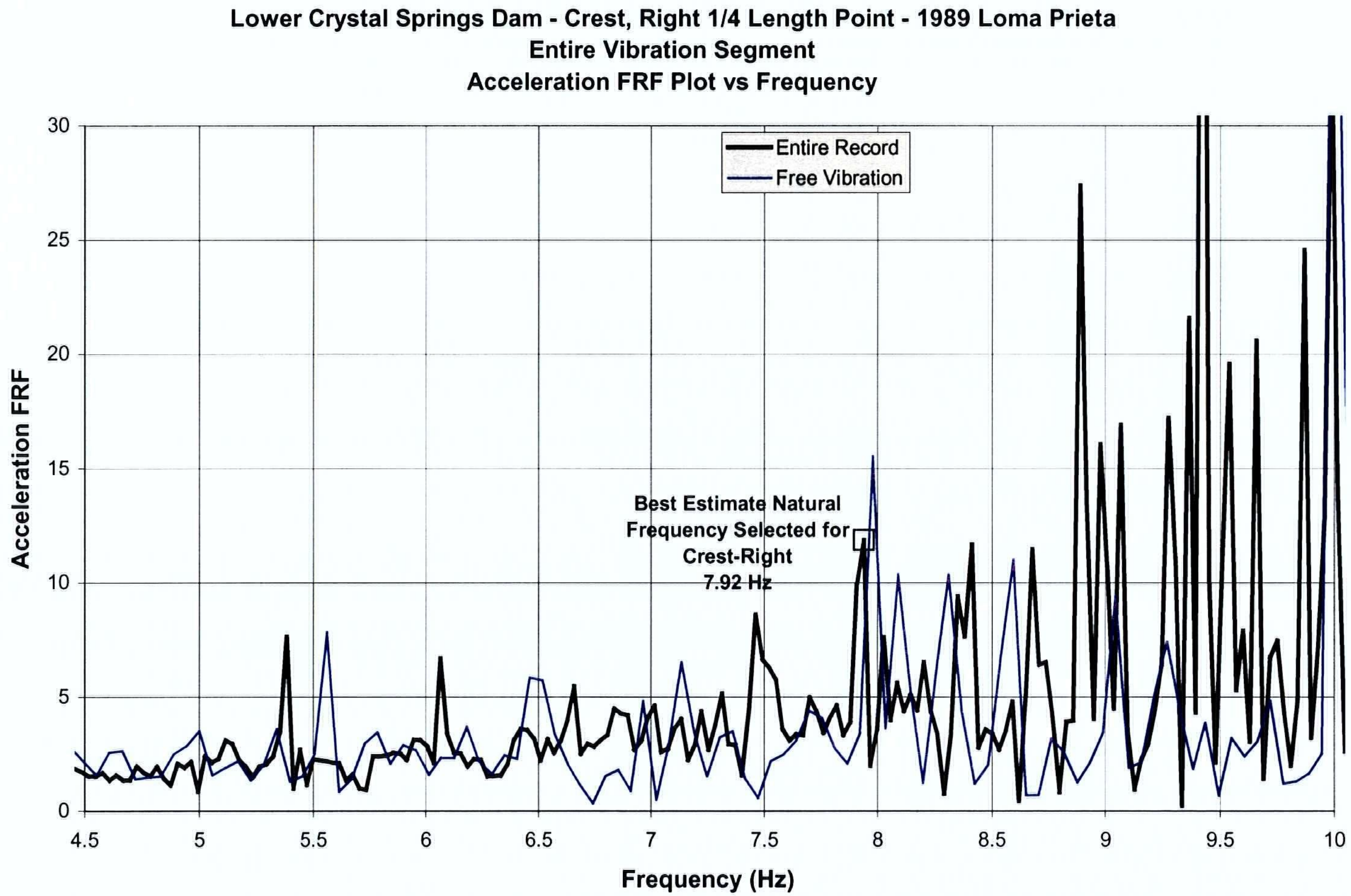

FIGURE 3-5b: Lower Crystal Springs Dam – Crest, Left 1/3 Length Point: Comparison of FRF Plots for Various Components of Time History Record

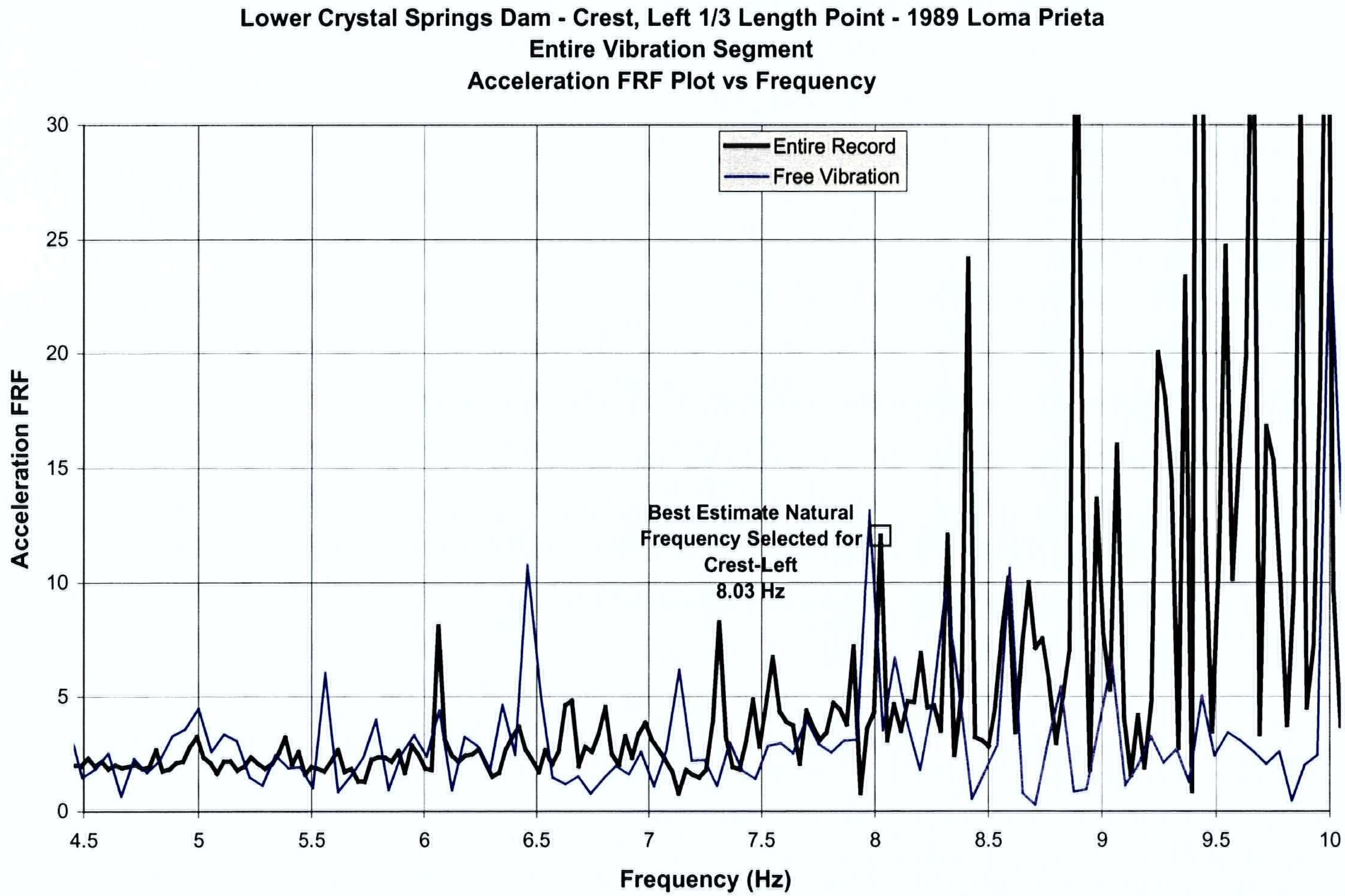

**FIGURE 3-5c: Lower Crystal Springs Dam:
Comparison of FRF Plots for Crest-Right and Crest-Left Time History Record**

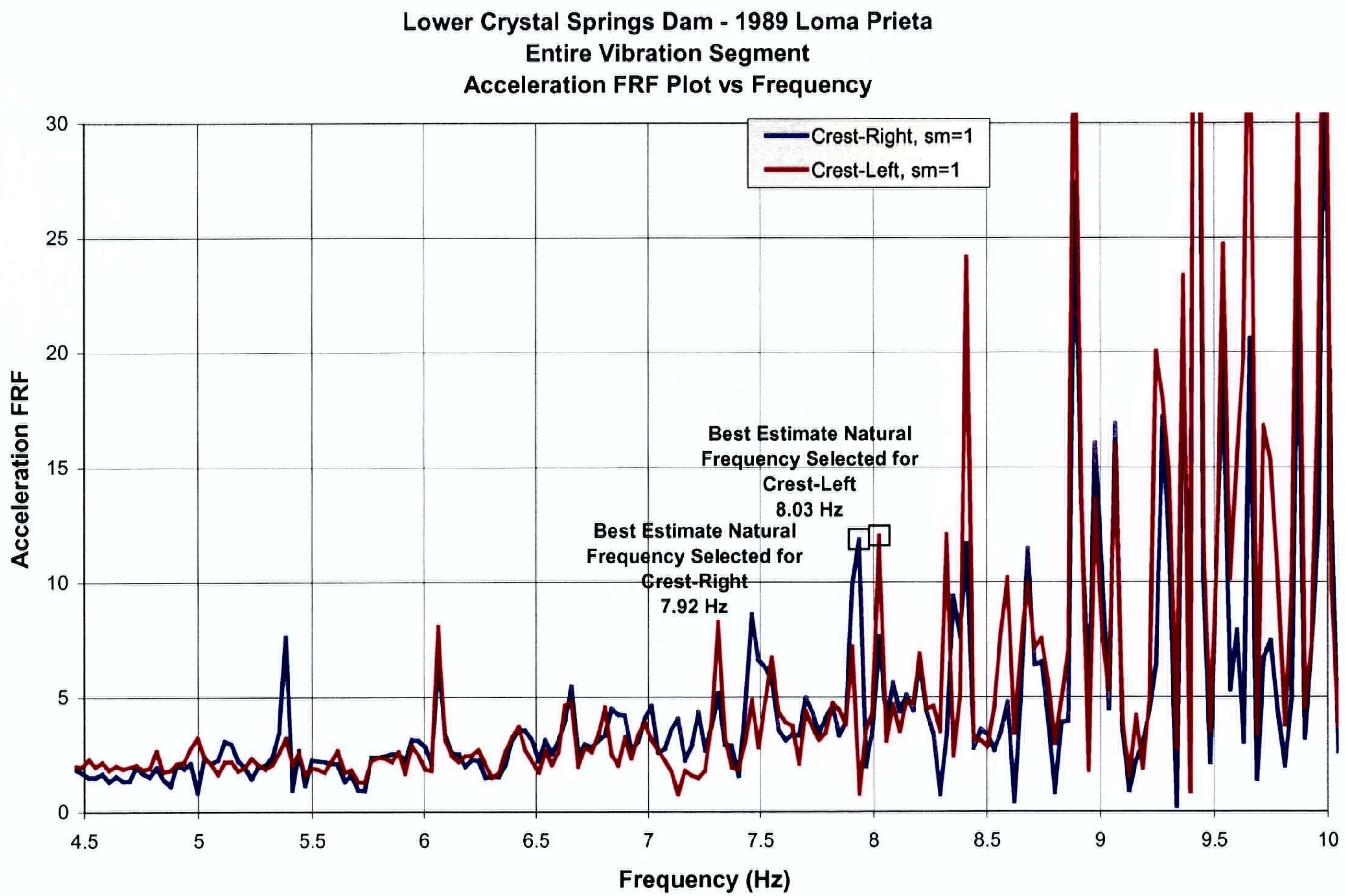

Chapter 4

Shear Key Study

4.0 INTRODUCTION

This is an exploratory study, investigating the process of modeling shear key joints in concrete monolith dams using the LS-DYNA finite element software [S1]. Concrete gravity dams are constructed in a sequence of blocks that are aligned adjacent to one other across the reservoir valley. In the event of an earthquake, significant shear and bending loads are transferred at the interfaces between blocks, as a result of hydrostatic and hydrodynamic loads, inertial loads, etc. As a result, shear keys are often incorporated into these joints to accept this loading to prevent sliding between blocks in the upstream-downstream plane of motion.

In a case study of Ruskin Dam in British Columbia, Canada, the shear transfer loads were determined at the interfaces between blocks. The case study dam consists of 8 monolithic blocks, implying there are 7 interfaces along which vertically-oriented shear keys transfer the majority of the shear load between adjacent blocks. In studies performed by BC Hydro [17], it was determined that if the dam was subjected to an acceleration of 1.27g, the maximum shear transfer along the dam would be approximately 2.0 MPa, which occurs near the left abutment. Failure of the system of shear keys at any interface could result in local slippage, increasing the chance of breach of the dam. Breach of the dam structure could cause severe flooding in the vicinity of the dam and endanger the lives of recreational users in the river below.

In this study, the author will present the process of modeling and testing the shear capacity of the shear keys using the LS-DYNA finite element software.

4.1 BACKGROUND INFORMATION

4.1.1 Load Sharing Study

A load sharing case study of Ruskin Dam was performed by the author in cooperation with the Dam Safety Engineering group at BCHydro in summer 2002, to determine the amount of shear force transferred between dam blocks under various loading conditions in an existing dam in Mission, BC. Figures 4-1a and 4-1b show the full-scale ANSYS 3D finite element model of the dam, used to perform two pushover analyses; one for the Design Basis Earthquake (DBE) peak spectral acceleration of 0.56g and one for the Maximum Design Earthquake (MDE) peak spectral acceleration of 1.27g. The total shear loads were calculated at each interface between adjacent dam blocks and at each interface between dam block and foundation. Figures 4-2a and 4-2b show the results of this study for the DBE and MDE level earthquakes, respectively.

It was found that the maximum shear force transfer occurs at the interface between dam blocks 3 and 4. The maximum shear stress transfer occurs at the interface between dam blocks 7 and 8. This is due mostly to the reduced effective area of the shear keys. The shear stresses transferred by the shear keys at this location are approximately 1.3 MPa for the DBE loading and 2.0 MPa for the MDE loading.

4.1.2 Shear Key Properties

The shear keys in the Ruskin Dam are 5 feet (1.5 m) in width, 1 foot (0.3 m) in depth, and extend along the height of the dam. There is a 1/12 gradation on either side of each key. Figure 4-3 shows a typical layout of shear keys at the cross section of an interface between dam blocks.

4.1.3 Predicted Shear Key Fracture Sequence

Prior to investigating the shear key problem, it is important to understand the mechanics behind shear key failure. In two papers by Kaneko [10, 11], the author presents the theory behind the shear-off fracture sequence in concrete shear keys and provides physical verification from experimental work and finite element analytical work on a shear key model. This is the fracture sequence that is expected to occur when the shear capacity of the system of shear keys is exceeded at any location of the dam. In his comparison study, Kaneko found good agreement between the theoretical fracture sequence and both FEM analysis and experimental work. He concluded that this fracture sequence can be used as a reliable method of predicting the response of shear key joints.

4.1.3.1 Shear Key Fracture Sequence

From previous experimental work by Bakhoum [2] involving shear-off failure of plain or fiber-reinforced concrete shear key joints, two distinct cracking mechanisms have been observed:

1. S crack – a large single curvilinear crack propagating diagonally from the base of the compression interface of the shear keys
2. M cracks – relatively short diagonal multiple cracks, occurring along the predicted shear-off fracture plane.

Figure 4-4a shows the cracking sequence observed this experimental work. This crack pattern has also been observed in various other experimental works and occurs in the following sequence.

1. Dominated by S Crack
2. Transition between S Crack and M Cracks
3. Dominated by M Cracks
4. Failure

Figure 4-4b shows the 4 phases of the cracking sequences for observed and idealized cracking.

Phase 1 – Dominated by S Crack

Upon initial loading, the corner of the shear key undergoes tensile stresses leading to propagation of the S crack. With continued shear loading, the S crack theoretically follows a curvilinear crack path that begins diagonally and curves towards the direction of the shear loading. For modeling purposes, this S crack can be idealized as an inclined linear crack. At a certain lead, an equilibrium is achieved within the system, causing an impedance of the S crack propagation.

Phase 2 – Transition between S Crack and M Cracks

The formation of the S crack changes the load path within the shear key, leading to the development of stress concentrations along the shear key base. This leads to the propagation of short, multiple cracks, or M cracks, along the shear key base. It can be assumed that the propagating M cracks are evenly distributed along the key base. However, due to additional bending stresses, there is a tendency for the propagation of M cracks to be initiated at the back end (furthest from the S crack) of the shear key.

Phase 3 – Dominated by M Cracks

Upon further shear loading, the existing M cracks continue to rotate about the principal stress axis, causing the crack opening displacement and compressive strain of the segments between M cracks to increase continuously.

Phase 4 – Failure

With even further increase of shear loading, the segments between M cracks undergo compressive crushing failure, leading to final failure of the shear key.

4.1.3.2 Verification of Theoretical Fracture Sequence: Physical Experiment

In his physical experiment, Kaneko tested a smaller scale model of a single shear key configuration under unidirectional loading. In total, 15 plain concrete shear keys were tested. The shear keys were oriented such that the load was applied vertically. The shear keys were 76.2 mm wide, 82.6 mm long, and 31.8

mm in depth. There is a 1/2 gradation on either side of each key. The base of the male shear key component was 98.4 mm. Figure 4-5a shows the orientation of the shear keys in the Kaneko experiment.

Figure 4-5b shows the general cracking sequence exhibited by the plain concrete shear key model. This figure shows good agreement with the theoretical cracking sequence in (I) S Crack propagation, (II) transition between S Crack and M Cracks, and (III) complete M Crack propagation.

4.1.3.3 Verification of Theoretical Fracture Sequence: Analytical Experiment

In his finite element analysis experiment, Kaneko tested the single shear key configuration from the physical experiment using the DIANA finite element software (Version not available). The geometry of the shear key male component was modeled with larger square elements for the body section, smaller triangular elements for the elements along the predicted shear failure plane, and quadrilateral elements for the head of the shear key. Figure 4-6a shows the configuration and geometry of the FEM model.

Figure 4-6b shows the cracking pattern of one of the test specimens for different vertical displacements. There is good agreement with the cracking pattern exhibited in the physical experiment and with the theoretical cracking pattern. In Figure 4-6b(a), the S Crack has propagated in the upper side of the shear key base at a vertical displacement of 0.3 mm. In Figure 4-6b(b), the S Crack has fully propagated, and M Crack has initiated at a vertical displacement of 0.4 mm. In Figure 4-6b(c), the M Crack propagation continues as the S Crack propagation has stopped, at a vertical displacement of 0.58 mm.

4.2 METHODOLOGY

Using an existing concrete monolith dam as a basis, a project was undertaken to estimate the capacity of the shear keys at the interfaces between dam blocks. It was initially proposed to conduct a physical experiment to simulate actual conditions of a single shear key subjected to various loading conditions. However, due to budget limitations, this experiment was not realized. An analytical experiment was then proposed, using the LS-DYNA finite element software to model the shear keys under various loading conditions.

The LS-DYNA Finite Element Software was used to generate models of the shear keys and to run analyses on them. In total, 31 models were generated; however, only 11 of these models yielded reasonable analytical results. The models were titled based on order of creation. Starting with the first series of models (3d2701), the title was changed whenever a major change was incorporated into the model. Hereafter, the models will be referred to as follows.

1. Model 1: 3d27-05a
2. Model 2: 3d27-05b
3. Model 3: 3d27-05c
4. Model 4: 3d27-08a
5. Model 5: 3d27-08b
6. Model 6: 3d27-10a
7. Model 7: 3d27-11b
8. Model 8: 3d27-001c

9. Model 9: 3d27-001d
10. Model 10:3d27-001d2
11. Model 11:3d27-001d3

This study was mainly a sensitivity analysis that was performed in order to test the impact of altering various parameters in the model. The purpose of this sensitivity analysis was to refine the model as best as possible before extracting the desired output data. The main parameters investigated in this study were:

1. Geometry
2. Material Models
3. Contact Elements
4. Load Protocols
5. Boundary Conditions

4.2.1 Geometry

Starting with a basic geometry, the first model was developed. The geometry for this model was based on the actual dimensions of the individual shear keys as presented in Section 4.1.2. Due to symmetry of the shear keys, it was only necessary to attempt to induce failure in one of the shear keys. Accordingly, it was decided that only the behavior of the male component was desired. As a result, the female component was initially modeled with a much coarser element mesh than the male component. Figure 4-7a shows the geometry used for models 1-3.

Initially, since it was desired to induce failure in only the male component, the elements in the male component were smaller than those in the female component. The elements in the male component were 3" x 3" (76.2 mm x 76.2 mm) and the elements in the female component were 6" x 6".

There were two major changes in geometry during this study. The first change was implemented in Model 4, as shown in Figure 4-10a. The second change was implemented in Model 5, as shown in Figure 4-11a. These changes were implemented to improve the accuracy of the results and to optimize the speed of the analysis runs.

The first major change in geometry involved reducing the size of the elements, removing a large section of elements, and adding a loading plate. It was decided that to improve the accuracy of the analytical results, a denser element mesh was necessary. As such, the elements in the male component were reduced in size from 3" x 3" (76.2mm x 76.2mm) to 1" x 1" (25.4 mm x 25.4 mm); the elements in the female component were reduced from 6" x 6" (152.4 mm x 152.4 mm) to 1" x 1" (25.4 mm x 25.4 mm). It was also decided to remove a large section of the shear key model, to signify the effective contact width of each shear key. It was also decided to add a loading plate to the front surface of the male component. This was added to ensure that the load was applied evenly along that surface.

The second major change in geometry involved reducing the size of the female component. It was decided that the purpose of the female component was not to undergo failure, but to induce failure in the male component. As such, a 54" (1.37 m) section of elements from the bottom of the female component was removed. To ensure failure would not occur in the female component, the degrees of freedom were constrained from all translation and rotation.

4.2.2 Material Model

Initially, an idealized linear elastic material model was used to represent the concrete material comprising the shear keys. In later versions of the shear key model, various other material models were used to represent the non-linear phase of the shear key response. A rigid material model was used to represent the loading plate, which was assumed to be comprised of steel, to simulate laboratory conditions in a physical experiment.

The initial material model for the male and female shear key components was a linear elastic material with properties based on non-reinforced concrete.

- Mass Density, ρ 2400 kg/m^3
- Young's Modulus, E 25 GPa
- Poisson's Ratio, ν 0.15

Various other material models were tested.

- Concrete Damage: used to model concrete structures experiencing damage under extreme loading
- Soil/Concrete: used to model various soil and concrete materials
- Kinematic Hardening Cap Model: used to model the kinematic hardening cap for concrete subjected to external pressure

However, the use of these material models led to errors in the analysis runs, possible due to insufficient availability of information.

The material model for the loading plate was a rigid material with properties based on structural steel.

- Mass Density, ρ 7830 kg/m^3
- Young's Modulus, E 207 GPa
- Poisson's Ratio, ν 0.28

4.2.3 Contact Elements

Contact elements were introduced into Model 2 and were altered throughout the modeling process. The first type of contact element used in the model allowed for sliding-only behavior between the master and slave elements; the master referring to the moving segment and the slave referring to the passive segment. In Model 3, a surface-to-surface contact element was introduced to model the different behavior at the compression portion of the contact surface. Another surface-to-surface contact surface was introduced for the load plate added in Model 4.

The input parameters for the contact surfaces were extracted from previous experimental work for concrete-to-concrete contact.

- Static Coefficient of Friction, μ_s 0.75
- Dynamic Coefficient of Friction, μ_d 0.70

It was found that the sliding contact surfaces exhibited separation under larger loading. However, since the shear keys are mostly confined from lateral separation due to adjacent dam blocks, this is not a realistic result. As such, the contact surface between the male and female components was changed to surface-to-surface contact elements along the entire surface.

4.2.4 Load Protocols

Initially, it was intended to test three load protocols for the shear key experiment.

- Monotonic Loading
- Cyclic Loading
- Earthquake Loading

However, due to the complexity of the finite element models, this was reduced to just monotonic loading to optimize the run time.

At first, an inertial load protocol was tested on the model, by imposing a linearly increasing acceleration on the male component, while restraining the female component. In the later models, a linearly increasing load protocol was applied to a loading plate on one side of the male component. Table 4-1 below summarizes the load protocols for the later models.

TABLE 4-1: Load Protocols

Model	Start time, t_1 (s)	End time, t_2 (s)	Start Load, P_1 (N)	End Load, P_2 (N)
4 (3d27-08a)	0	20	0	1,000
5 (3d27-08b)	0	20	0	10,000
6 (3d27-10a)	0	20	0	2,000,000
7 (3d27-11b)	0	20	0	20,000,000
8 (3d27-001c)	0	10	0	20,000,000
9 (3d27-001d)	0	10	0	200,000,000
10 (3d27-001d2)	0	10	0	40,000,000
11 (3d27-001d3)	0	10	0	80,000,000

4.2.5 Boundary Conditions

The term "boundary conditions" refers to the constraint conditions of the degrees of freedom for the nodes in the model. The coordinate system used for these models is shown on each figure, with the positive-X direction pointing right, the positive-Y direction pointing up, and the positive-Z direction pointing perpendicular to the plane of the figure. Initially, the exterior nodes of the female component were constrained from all DOFs. The interior nodes of the female component were constrained from Y-translation, Z-translation, X-rotation, and Y-rotation. In the male component, the exterior nodes were constrained from all DOFs except for X-translation and the interior nodes were constrained from Y-translation, Z-translation, X-rotation, and Y-rotation. This was considered to be consistent with the DOF constraints in the proposed physical model.

In Model 4 (see Figure 4-10a), the loading plate was constrained from all DOF's except for X-translation, to ensure that the load imposed on the male component was unidirectional. In Model 5 (see Figure 4-11a), it was decided to constrain all DOFs in the female component, in order to reduce the size of the model and to isolate the failure mechanism to the male component. This set of boundary conditions was used for the models generated thereafter.

4.3 RESULTS

The earliest models (3d27-01 to 3d27-04) were unable to yield results, due to errors or inconsistencies with the analysis program. The first model to produce a valid analysis run was Model 1. This section will discuss the main analysis results of each of the models. Of 31 models generated, only 11 were capable of yielding results.

1. Model 1: 3d27-05a
2. Model 2: 3d27-05b
3. Model 3: 3d27-05c
4. Model 4: 3d27-08a
5. Model 5: 3d27-08b
6. Model 6: 3d27-10a
7. Model 7: 3d27-11b
8. Model 8: 3d27-001c
9. Model 9: 3d27-001d
10. Model 10: 3d27-001d2
11. Model 11: 3d27-001d3

The results from Model 10 (see Figure 4-16a) were the most realistic of those presented in this chapter. The stress patterns developed at the right side of the shear key are representative of those necessary to initiate propagation of the S-crack. However, the magnitudes of both the compressive and tensile stresses (>1000MPa) far exceed the compressive and tensile strengths of structural concrete (25 MPa and 2.5 MPa, respectively). This result is likely due to the material model used in the study.

A linear-elastic material model, with properties based on structural concrete, was used in the models. As part of the sensitivity analysis, various other material models were tested. However, use of more complex models led to instabilities in the model.

Based on the expected cracking pattern of the shear keys presented in Section 4.1.1, the stress patterns that develop around the right of the shear key are reasonable. A large compressive stress concentration coupled with a large tensile stress concentration is representative of fracture conditions in concrete.

4.3.1 Model 1 (3d27-05a)

Figure 4-7a shows Model 1 in its unloaded state. Model 1 consisted of a male component with approximately 76.2 mm x 76.2 mm elements and a female component with approximately 152.4 mm x 152.4 mm elements.

The male and female components were composed of the same elastic material with properties consistent with structural concrete.

- Mass Density, ρ 2400 kg/m^3
- Young's Modulus, E 25 GPa
- Poisson's Ratio, ν 0.15

The male component was subjected to a linear acceleration load curve. From rest, the acceleration increased to a peak of 1g (9.81 m/s^2) at a time of 10 s.

Initially, the exterior nodes of the female component were constrained from all DOFs. The interior nodes of the female component were constrained from Y-translation, Z-translation, X-rotation, and Y-rotation. In the male component, the exterior nodes were constrained from all DOFs except for X-translation and the interior nodes were constrained from Y-translation, Z-translation, X-rotation, and Y-rotation. This was considered to be consistent with the DOF constraints in the proposed physical model.

At a time of about 4.5 seconds, the model became unstable as the male component started to slide past the female component, without generating any internal stresses. Figure 4-7b shows the stress patterns in the male component as it separates from the female component.

4.3.2 Model 2 (3d27-05b)

Figure 4-8 shows Model 2 in its fully loaded state. The main changes introduced in this model were:

- Contact surfaces
- Increased acceleration of male part
- New boundary conditions for degrees of freedom

A sliding-only contact surface was incorporated into this model to represent the static and dynamic friction present at the interface between the male and female components.

- Static Coefficient of Friction, μ_s 0.75
- Dynamic Coefficient of Friction, μ_d 0.70

The applied acceleration was doubled in this model to evaluate how the response would be affected. From rest, the acceleration increased to a peak of 2g (18.62 m/s^2) at a time of 10 s. It was also decided to add a constraint to Y-translation of the interior nodes in order to represent the confining action imposed by the adjacent dam blocks.

Figure 4-8 also shows the internal horizontal stress contours at the maximum loading (t = 10s). The tensile stresses (red) at the left side of the male shear key do not represent expected results. It is believed that this resulted from the contact elements on the left interface of the shear key.

4.3.3 Model 3 (3d27-05c)

Figure 4-9 shows Model 3 in its fully loaded state. The main change introduced in this model was the separation of the sliding contact surface from the compression contact surface. To achieve this, a surface-to-surface contact surface was used to model the compressive surface at the front edge of the shear key. Figure 4-9 also shows the internal horizontal stress contours at the maximum loading (t = 10s). The stress patterns at the right side of the male shear key are more realistic than those of previous models.

4.3.4 Model 4 (3d27-08a)

Figure 4-10a shows Model 4 in its unloaded state. The main changes introduced in this model were:

- New geometry
- Steel plate for application of load
- New load curve
- New contact surface

The first change to the geometry of the model involved reducing the size of the elements. The elements in the male component were reduced from 3" x 3" (76.2 mm x 76.2 mm) to 1" x 1" (25.4 mm x 25.4 mm); the elements in the female component were reduced from 6" x 6" (152.4 mm x 152.4 mm) to 1" x 1" (25.4 mm x 25.4 mm). The second change involved removing a large section of the shear key model. The third change involved addition of a load plate to the left side of the male component.

The purpose of this plate was to accommodate a change from acceleration input to load input. This plate was modeled as a rigid material with properties similar to structural steel.

- Mass Density, ρ 7.83e3 kg/m^3

- Young's Modulus, E 2.07e5 MPa
- Poisson's Ratio, ν 0.28

The elements in the load plate component were 1" x 1" (25.4 mm x 25.4 mm). A surface-to-surface contact surface was used to model the interface between the load plate and the male component. The load plate was constrained from all DOFs except for X-translation, thus concentrating the load in the X-direction along the left surface of the male component.

A linear load curve was used to apply this load, to a maximum of 1000N over 20 seconds. This load was applied to the load plate in the X-direction. Figure 4-10b shows the internal horizontal stress contours at the maximum loading (t = 20s).

4.3.5 Model 5 (3d27-08b)

Figure 4-11a shows Model 5 in its unloaded state. The main changes introduced in this model were:

- New geometry
- Increased load
- New boundary conditions for female segment

In order to focus the attention of the analysis to the failure of the male component, all DOFs in the female component were constrained. As a result, the lower section of the female component was deemed unnecessary and was removed.

The peak load was also increased to 10000N over 20 seconds. Figure 4-11b shows the internal horizontal stress contours at the maximum loading (t = 20 s).

4.3.6 Model 6 (3d27-010a)

Figure 4-12 shows Model 6 in its fully loaded state. The main change in this model was the increase in the load. In an iterative process, the load was increased gradually over 6 models (3d27-09a to 3d27-09f) in search of a failure load. In Model 6, the load was increased to 20 MN over 20 seconds in the positive X direction. Figure 4-12 also shows the internal horizontal stress contours at the maximum loading (t = 20 s). It was predicted that there would be compression stresses at the load plate interface and the compression interface at the right side of the shear key. However, the compression stress was concentrated at a certain point on the load plate interface, indicating there may have been some errors in the geometry.

4.3.7 Model 7 (3d27-011b)

Figure 4-13a shows Model 7 in its fully loaded state. In this model, the geometry was reconstructed in order to ensure there were no errors that could affect the results. A linearly increasing load of 20 MN over 10 seconds was applied to the left side of the male component. Figure 4-13a also shows the internal horizontal stress contours just prior to the model experiencing instability at t = 5 s. There is a visible difference from the previous model, as the stress patterns are more evenly distributed along both the interface of the load plate and at the compression interface of the shear key. The peak tensile and compressive stresses at the right of the male shear key exceed 100 MPa.

Figure 4-13b shows the model undergoing instability at t = 6s. The failure results in the load plate separating from the male component. A potential cause of this failure was the constraints applied to the load plate.

4.3.8 Model 8 (3d27-001c)

Figure 4-14a shows Model 8 in its fully loaded state. In this model additional constraints were added to the load plate, in order to prevent instability at higher loads. As a result, the model could be loaded to the maximum load (20 MN) without any failure or instability. Figure 4-14a also shows the internal horizontal stress contours at the maximum loading (t = 10 s). The resulting stress patterns are similar to those of the previous model, with the peak tensile and compressive stresses at the right of the male shear key exceeding 500 MPa.

Figure 4-14b shows a close-up diagram of the stress patterns at the area of expected S-crack propagation. One interesting observation from this figure is the discontinuity at the base of the shear key, where some overlap occurs between the male and female components. A potential reason for this overlap is the nature of the contact elements used at this interface.

4.3.9 Model 9 (3d27-001d)

In this model, the load protocol was increased to a linearly increasing load of 200 MN over 10 seconds. The purpose of increasing the load by so much was to identify a failure load. Figure 4-15 shows the internal horizontal stress contours at the maximum loading before failure (t = 1.5 s). The resulting stress patterns are similar to those of the previous model, with the peak tensile and compressive stresses at the right of the male shear key exceeding 800 MPa.

4.3.10 Model 10 (3d27-001d2)

Figure 4-16a shows Model 10 in its fully loaded state. The main change in this model was a reduction in load to 20% of that used in the previous model (40 MN) over 10 seconds. This was decided because the previous model experienced failure at approximately 40 MN load. Figure 4-16a also shows the internal horizontal stress contours at the maximum loading before failure (t = 8.5 s). The peak tensile and compressive stresses at the right of the male shear key exceed 1000 MPa.

Figure 4-16b shows a close-up of the stress patterns at the right of the male shear key. Again, there is visible overlap at the contact surface at the base of the shear key.

4.3.11 Model 11 (3d27-001d3)

Figure 4-17a shows Model 11 in its fully loaded state. The main changes introduced in this model were:

- Increased load
- Changed contact surface to prevent separation

In this model, surface-to-surface contact elements replaced the sliding-only contact elements at the base of the shear key. To account for the expected increase in capacity, the load protocol was also increased to 80 MN over 10 seconds. Figure 4-17a also shows the internal horizontal stress contours at the maximum loading (t = 10s).

Figure 4-17b shows a close-up of the stress patterns at the right of the male shear key. The peak tensile and compressive stresses at the right of the male shear key are in the range of approximately 600 MPa. This is a reasonable result, as a large portion of the load is transferred to the contact elements at the base of the shear key. This reduction of stresses caused by the behavior at the base of the shear key might not be representative of actual conditions.

4.4 SUMMARY

In this exploratory study, a parametric sensitivity analysis involving finite-element modeling of shear keys was carried out. The LS-DYNA finite element software was used to model and to run analyses on the models. The shear keys of an existing dam in Mission, BC, served as the basis for this study.

4.4.1 Summary of Sensitivity Analysis

Five main parameters were the focus of the sensitivity analysis:

1. Geometry
2. Material Models
3. Contact Elements
4. Load Protocols
5. Boundary Conditions

4.4.1.1 Geometry

The geometry for the first model (See Figure 4-7a) was based on the actual dimensions of the individual shear keys as presented in Section 4.1.2. There were two major changes in geometry during this study. The first change was implemented in Model 4 (See Figure 4-10a), and involved reducing the size of the elements, removing a large section of elements, and adding a loading plate. The second change was implemented in Model 5 (See Figure 4-11a), and involved reducing the size of the female component. These changes were implemented to improve the accuracy of the results and to optimize the speed of the analysis runs.

4.4.1.2 Material Model

Initially, an idealized linear elastic material model was used to represent the concrete material comprising the male and female shear key components.

In later versions of the shear key model, various other material models were tested.

- Concrete Damage: used to model concrete structures experiencing damage under extreme loading
- Soil/Concrete: used to model various soil and concrete materials
- Kinematic Hardening Cap: used to model the kinematic hardening cap for concrete subjected to external pressure

However, the use of these material models led to errors in the analysis runs, and were not successfully used. A rigid material model was used to represent the loading plate, which was assumed to be comprised of structural steel, to simulate laboratory conditions in a physical experiment.

4.4.1.3 Contact Elements

The first type of contact element used was for sliding-only behavior between the master and slave elements in Model 2. In Model 3, a surface-to-surface contact element was introduced to model the different behavior at the compression portion of the contact surface. It was later found that the sliding contact surfaces exhibited separation under larger loading. However, since the shear keys are mostly confined from lateral separation due to adjacent dam blocks, this is not a reasonable result. As such, the contact surface between the male and female components was changed to surface-to-surface contact elements along the entire surface. Another surface-to-surface contact surface was introduced for the load plate added in Model 4.

4.4.1.4 Load Protocols

Initially, it was intended to test three load protocols for the shear key experiment.

- Monotonic Loading
- Cyclic Loading
- Earthquake Loading

However, due to the complexity of the finite element models, this was reduced to monotonic loading only to optimize the run time.

At first, an inertial load protocol was applied to the model, by imposing a linearly increasing acceleration on the mass of the male component, while restraining the female component. In the later models, a linearly increasing load protocol was applied to a loading plate on one side of the male component.

4.4.1.5 Boundary Conditions

The boundary constraints were initially set so that the male component would be free to move only in the X-translation direction only and the female component would be fixed. The interior nodes of the male component were also free to rotate about the Z axis to consider the internal strains due to loading.

The loading plate (added in Models 4 to 11) was free to move only in X-translation, to ensure that the load imposed on the male component was unidirectional. In Model 5 (see Figure 4-11a), it was decided to constrain all DOFs in the female component, in order to reduce the size of the model and to isolate the failure mechanism to the male component. This set of boundary conditions was used for the models generated thereafter.

4.4.2 Analysis Results

Figures 4-7 to 4-17 show the LS-DYNA analytical output for Models 1 to 11. In the earlier models (Models 1-7), the stress patterns at the right side of the male component were inconsistent with those presented the shear key study by Kaneko as mentioned in Section 4.1.3. In the more refined models (Models 8 to 11), the stress patterns at the right side of the male component indicate a large coupling of compressive and tensile stresses. These stress patterns showed good agreement with those presented by Kaneko, and were indicative of the cracking sequence from his experimental work. The large tensile stress concentration would be necessary to initiate propagation of the S-Crack. Once this cracking has occurred, the stress will be transferred to the predicted failure plane, along which M crack propagation, and eventual shear fracture will occur.

4.5 CONCLUSIONS

The main purposes of this study were to examine stress patterns that develop in shear keys under applied loading and to evaluate the structural stability of these shear keys. The following can be concluded from this study:

4.5.1 Regarding the Sensitivity Analysis

- The sensitivity analysis was successfully carried out, as various material and geometric parameters were tested in order to refine the model.
- The geometry of the latest model exhibited a close representation of the actual geometry of the shear keys. By adding the load plate to the left side of the model, it was possible to apply a uniform load representative of a typical monotonic load protocol.
- Various material models were tested during this study. However, the more complex material models produced incoherent results. As a result, a linear-elastic concrete material model was used throughout the study.
- Two types of contact elements were used to represent the sliding surface between the male and female components. Optimal results were obtained by using a combination of sliding-only contact elements along the horizontal surfaces of the interface and surface-to-surface contact elements along the slanted compression surface of the interface.
- A monotonic load protocol was used throughout the study. The peak load was gradually increased for the various models.

- The optimal configuration of nodal constraints was obtained for one of the intermediate models. In the stationary female component, all nodes were constrained from all DOFs. In the male component, the exterior nodes were constrained from all DOFs except for translation in the X-direction (the primary plane of motion); the interior nodes were constrained from all DOF's except for translation in the X-direction, and rotation in the Z-direction.

4.5.2 Regarding the Analytical Results

- The results from Model 10 (see Figure 4-16b) seemed to be the most realistic of all the models.
- The stress patterns that develop in the shear keys under applied horizontal load are reasonable for loading prior to initial propagation of the S-Crack.
- The S-Crack dominant stage of the expected cracking pattern in the shear keys presented by Bakhoum (1991) was successfully modeled in this study.

4.6 RECOMMENDATIONS

Some recommendations for future work on this topic are:

1. Further investigation into the non-linear and post-cracking behavior of the shear keys, by utilizing some of the more complex material models in the LS-DYNA library. This may also be carried out by introducing cracks into the geometry of the shear key model where cracking is expected to occur for the various stages of the expected cracking pattern.
2. Further investigation into some of the other contact element types available in the LS-DYNA library. One of the potential sources of error in the results was the consistency of the contact surfaces.
3. Expanding the analysis to included cyclic loading and earthquake loading.
4. Use of another finite-element software program to provide alternative results for comparison purposes.
5. Realization of a physical experiment to compliment the analytical results.

FIGURE 4-1a: ANSYS FEM Model of Ruskin Dam: Isometric View

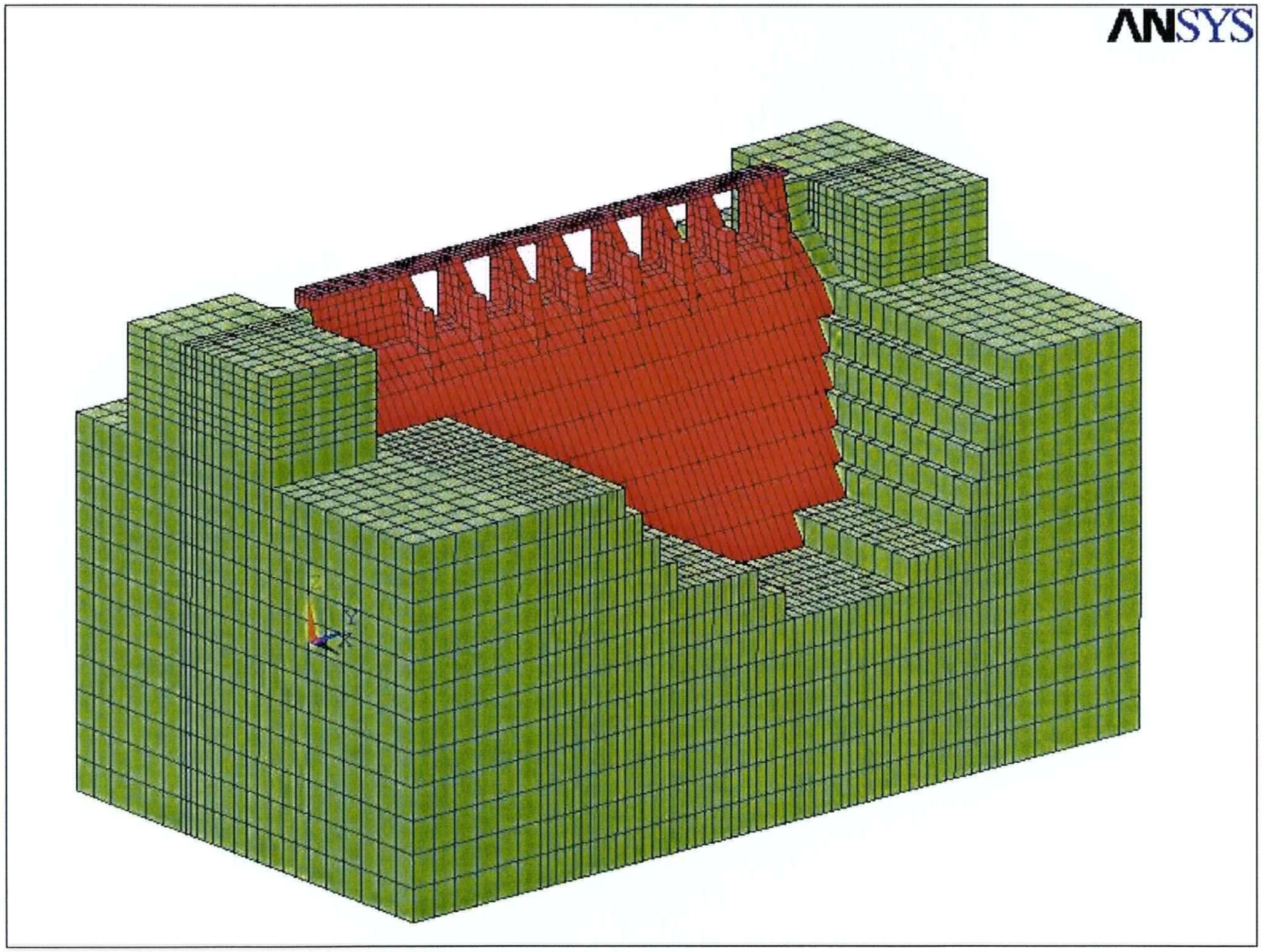

FIGURE 4-1b: ANSYS FEM Model of Ruskin Dam: Plan View

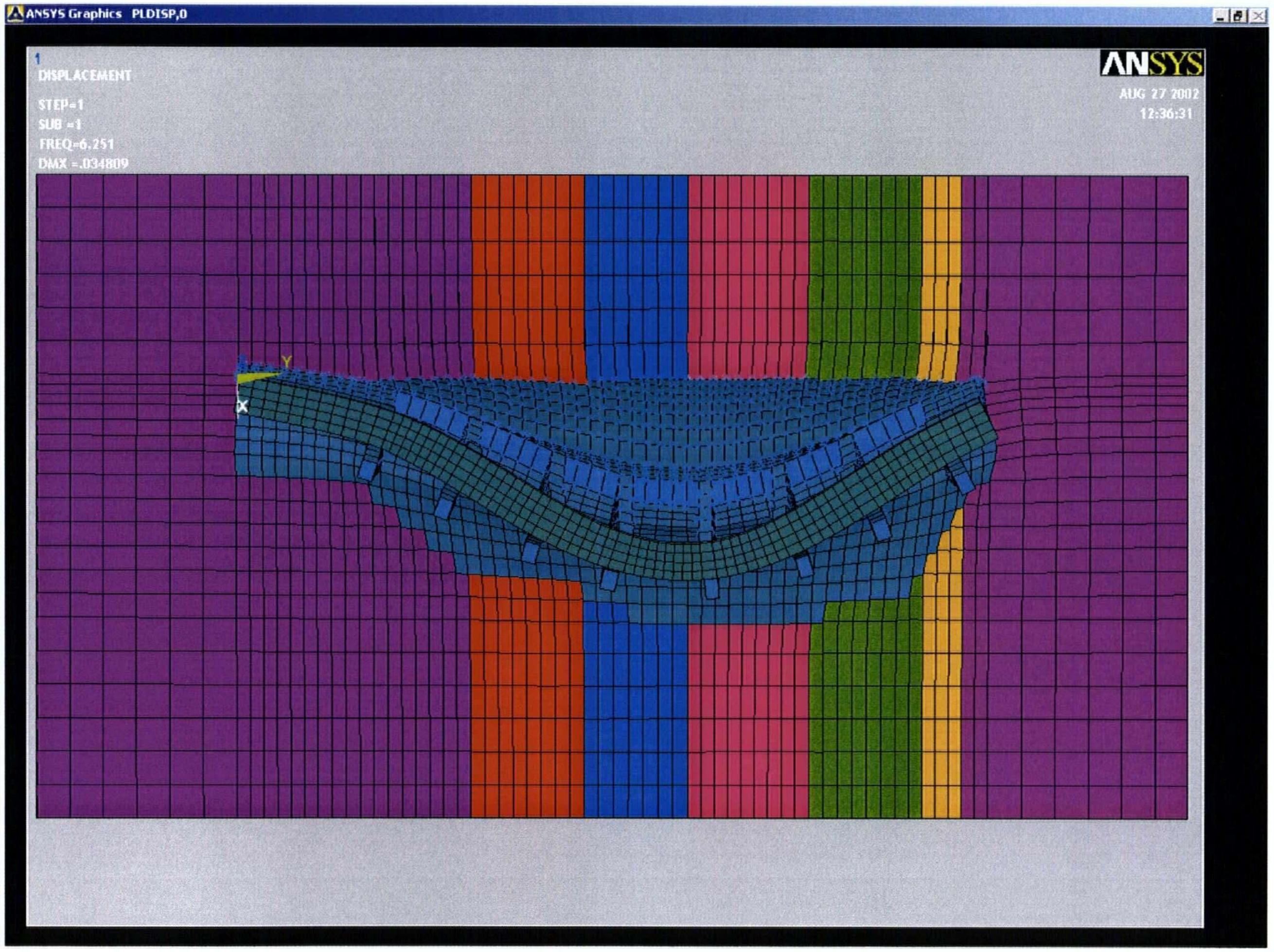

FIGURE 4-2a: Load Sharing Summary: 0.56g

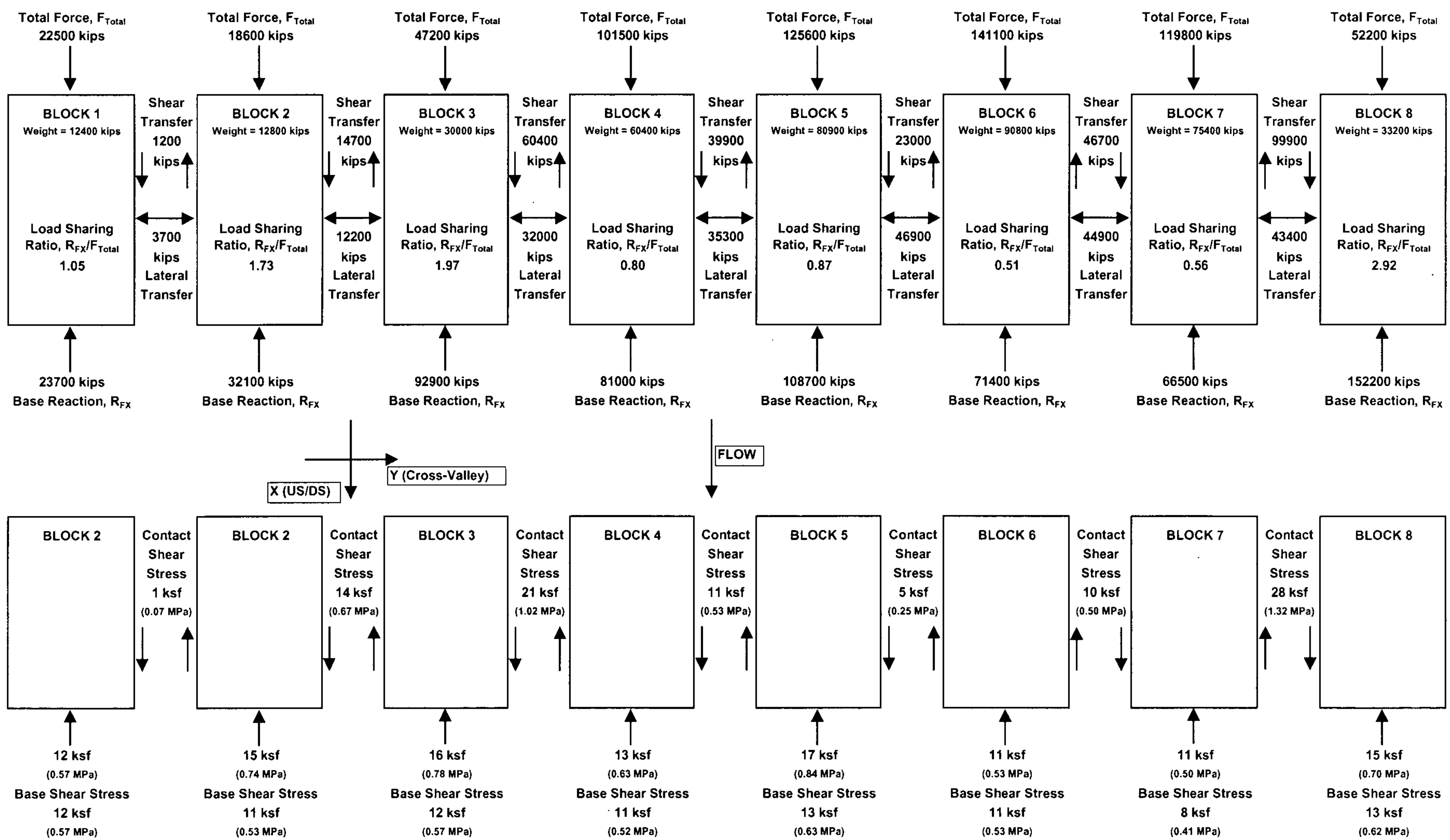

Note:

1 Shear Stresses at Construction Joints calculated using 40% of the total area, to account for the portion of the shear keys contributing to the shear strength

2 Base Shear Stresses calculated using actual areas (top) and ANSYS model areas (bottom)

FIGURE 4-2b: Load Sharing Summary: 1.27g

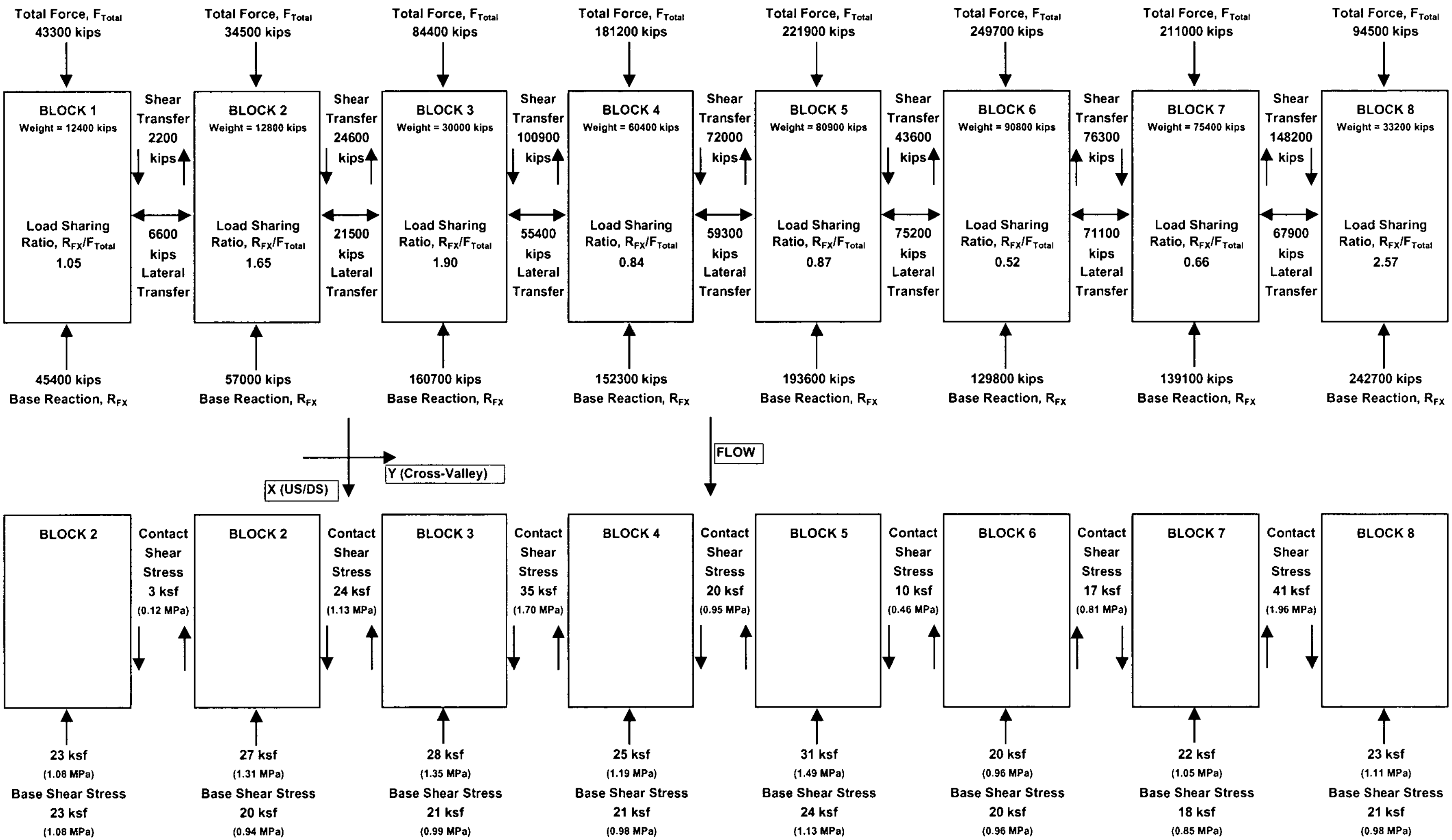

Note:
1 Shear Stresses at Construction Joints calculated using 40% of the total area, to account for the portion of the shear keys contributing to the shear strength
2 Base Shear Stresses calculated using actual areas (top) and ANSYS model areas (bottom)

FIGURE 4-3: Typical Cross-Section of an Interface between Blocks

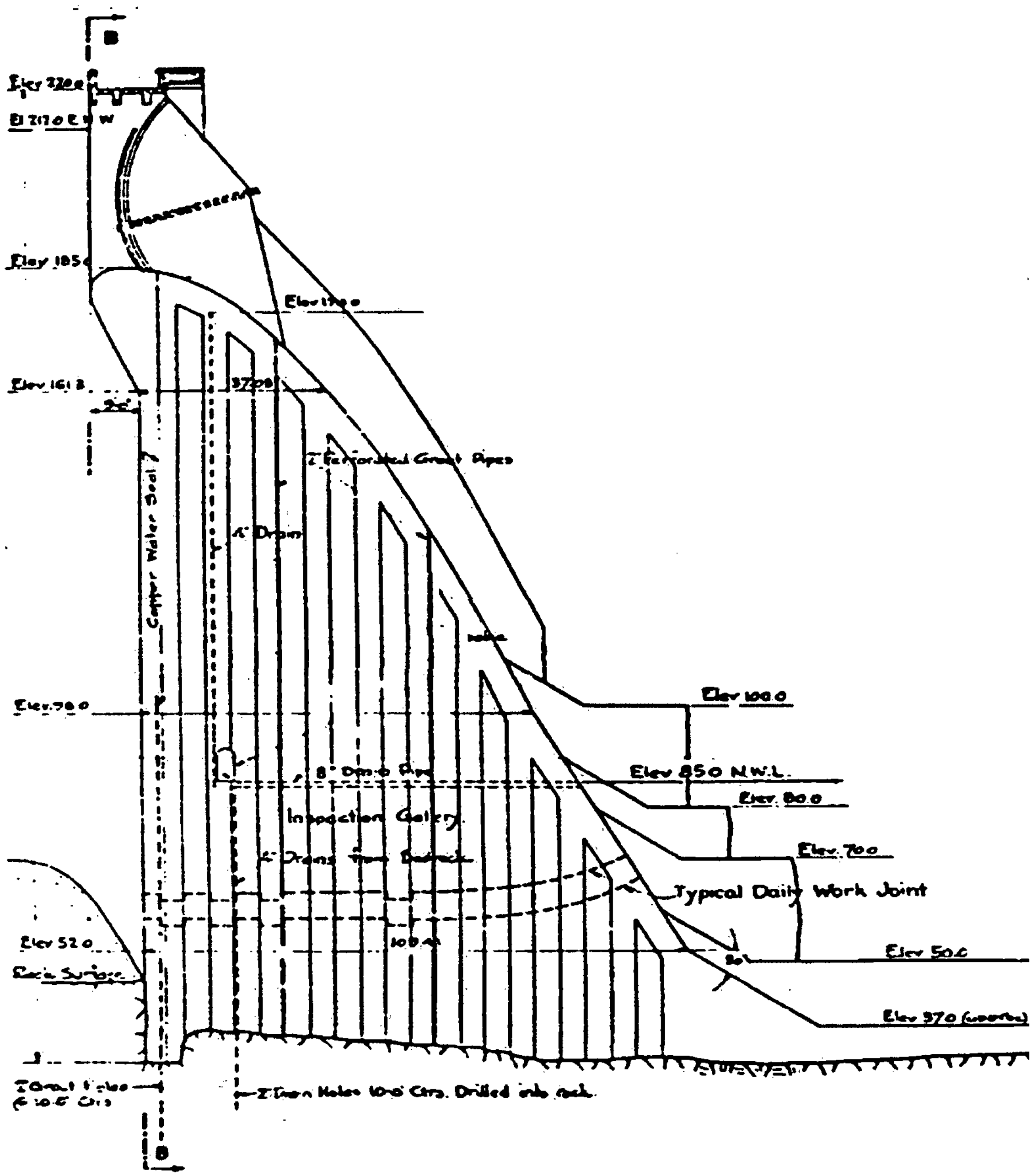

FIGURE 4-4a: Shear Key Cracking Sequence

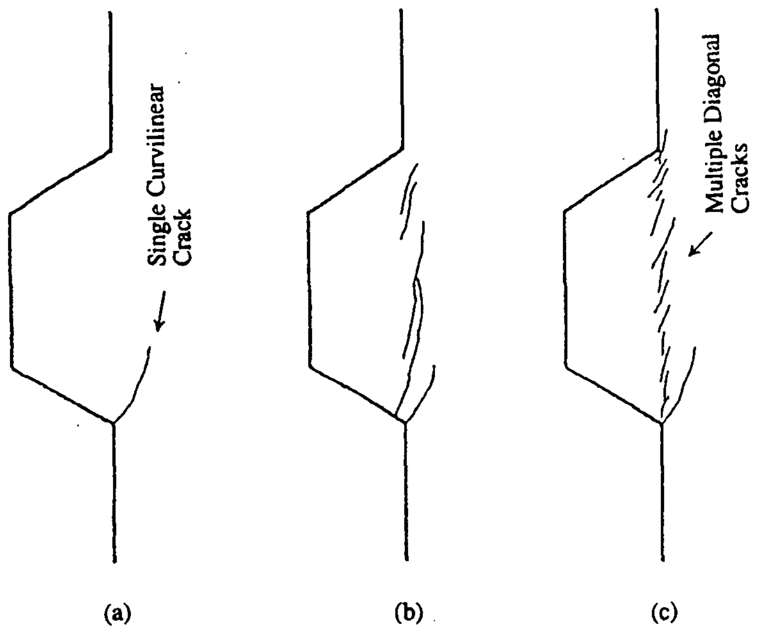

FIGURE 4-4b: Shear-off Fracture Sequence of (a) Observed Cracks; (b) Idealized Cracks

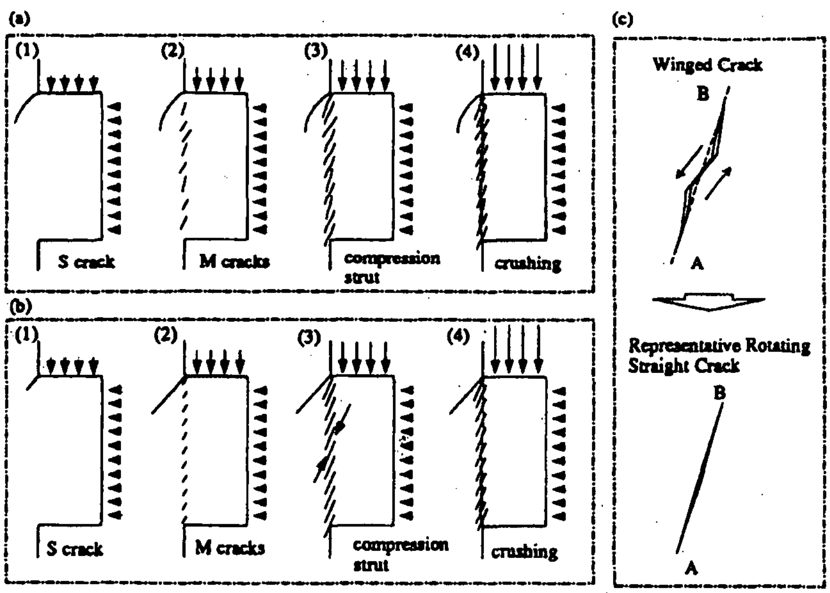

FIGURE 4-5a: Kaneko Physical Experiment: Orientation of Shear Keys

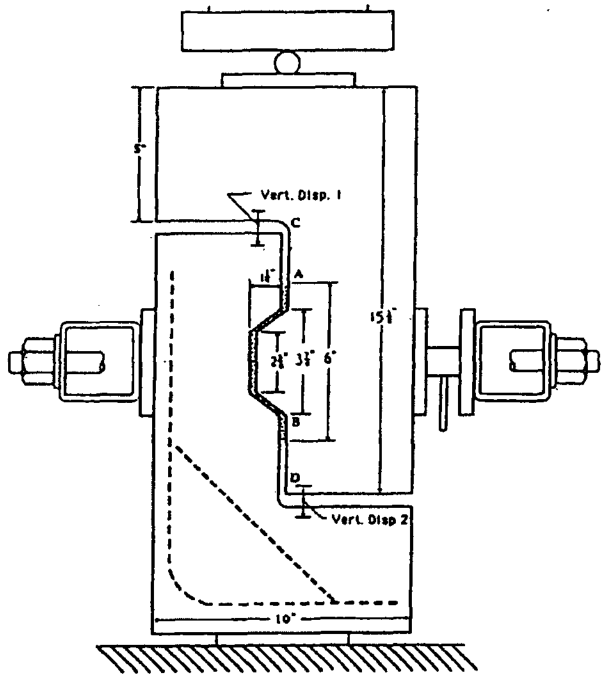

FIGURE 4-5b: Kaneko Physical Experiment: Observed Cracking Pattern

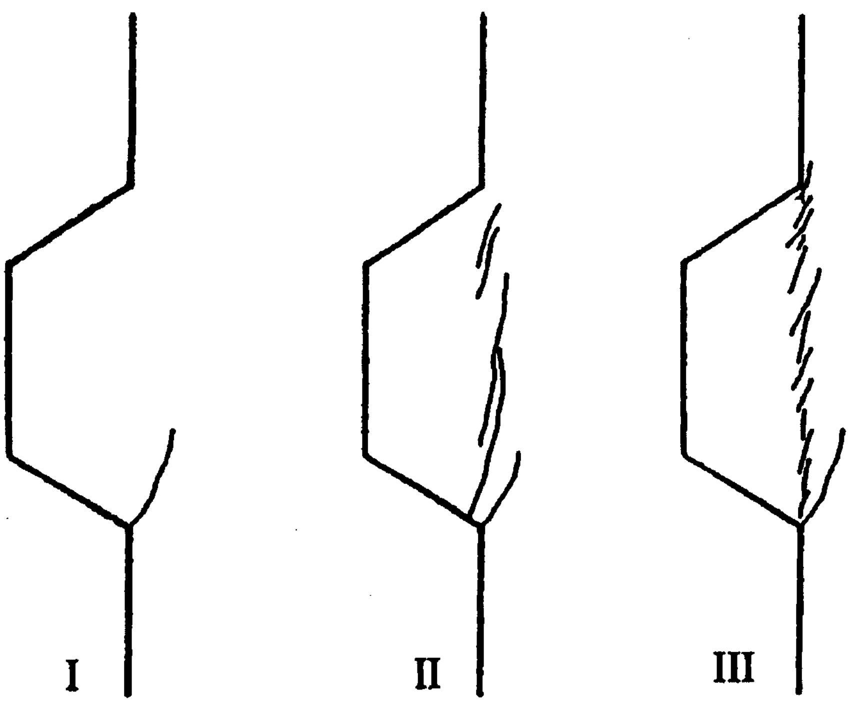

FIGURE 4-6a: Kaneko FEM Experiment: Orientation of Shear Keys

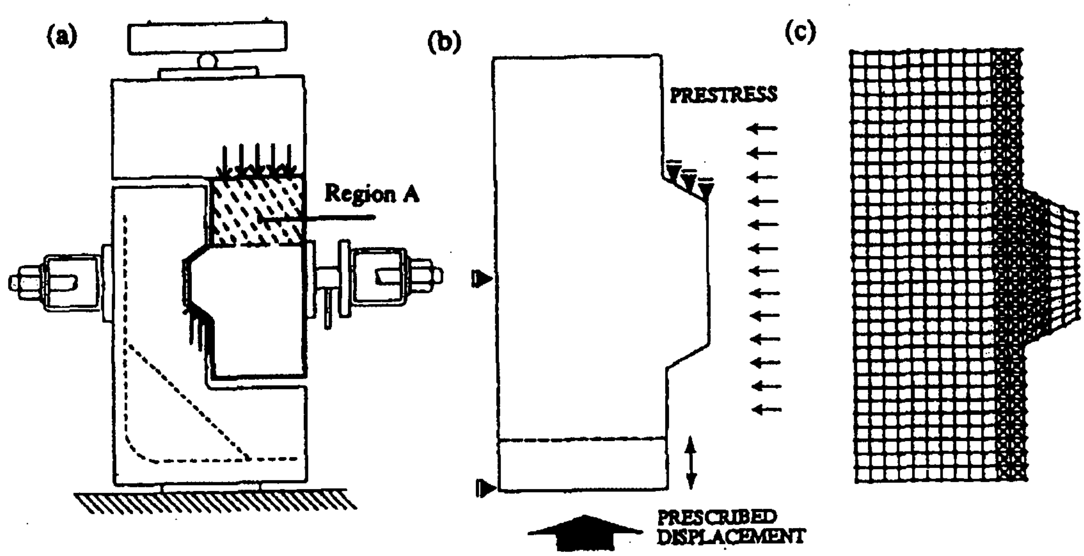

FIGURE 4-6b: Kaneko FEM Experiment: Observed Cracking Pattern for Vertical Displacement of (a) 0.3 mm, (b) 0.4 mm, (c) 0.58 mm

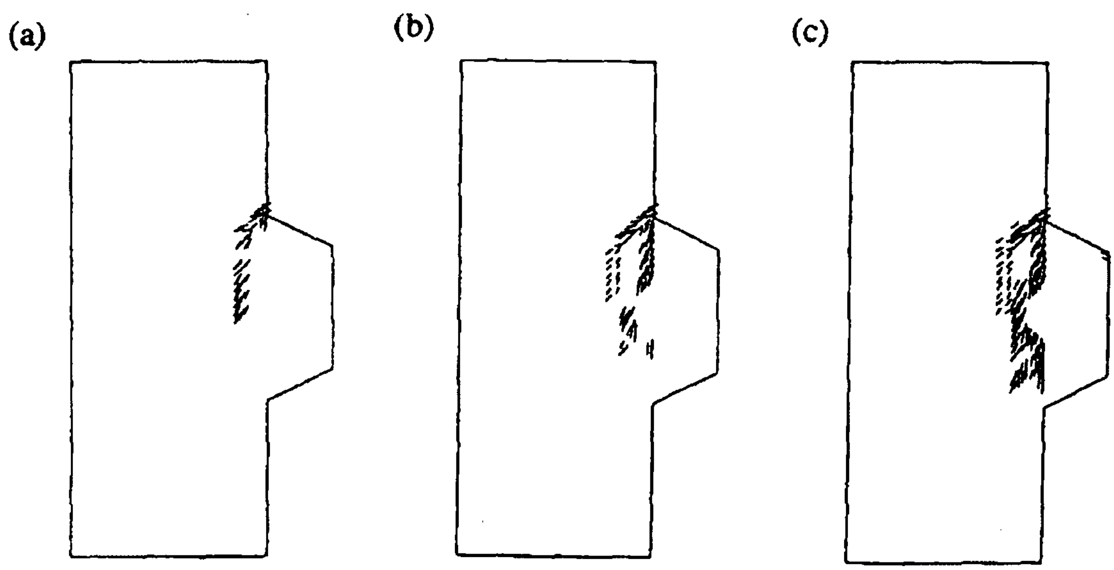

FIGURE 4-7a: Model 1, t = 0 s

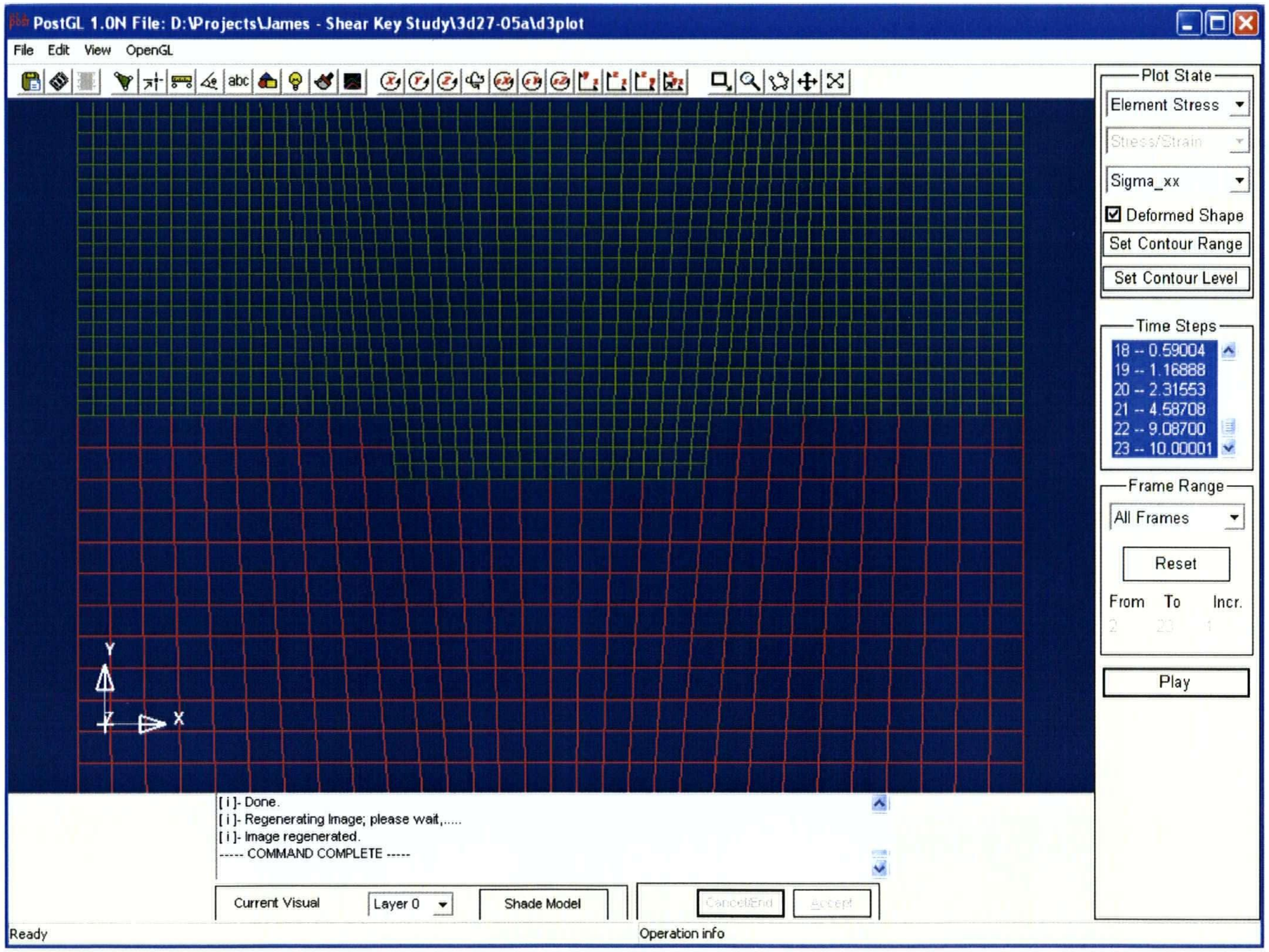

FIGURE 4-7b: Model 1, t = 4.6 s

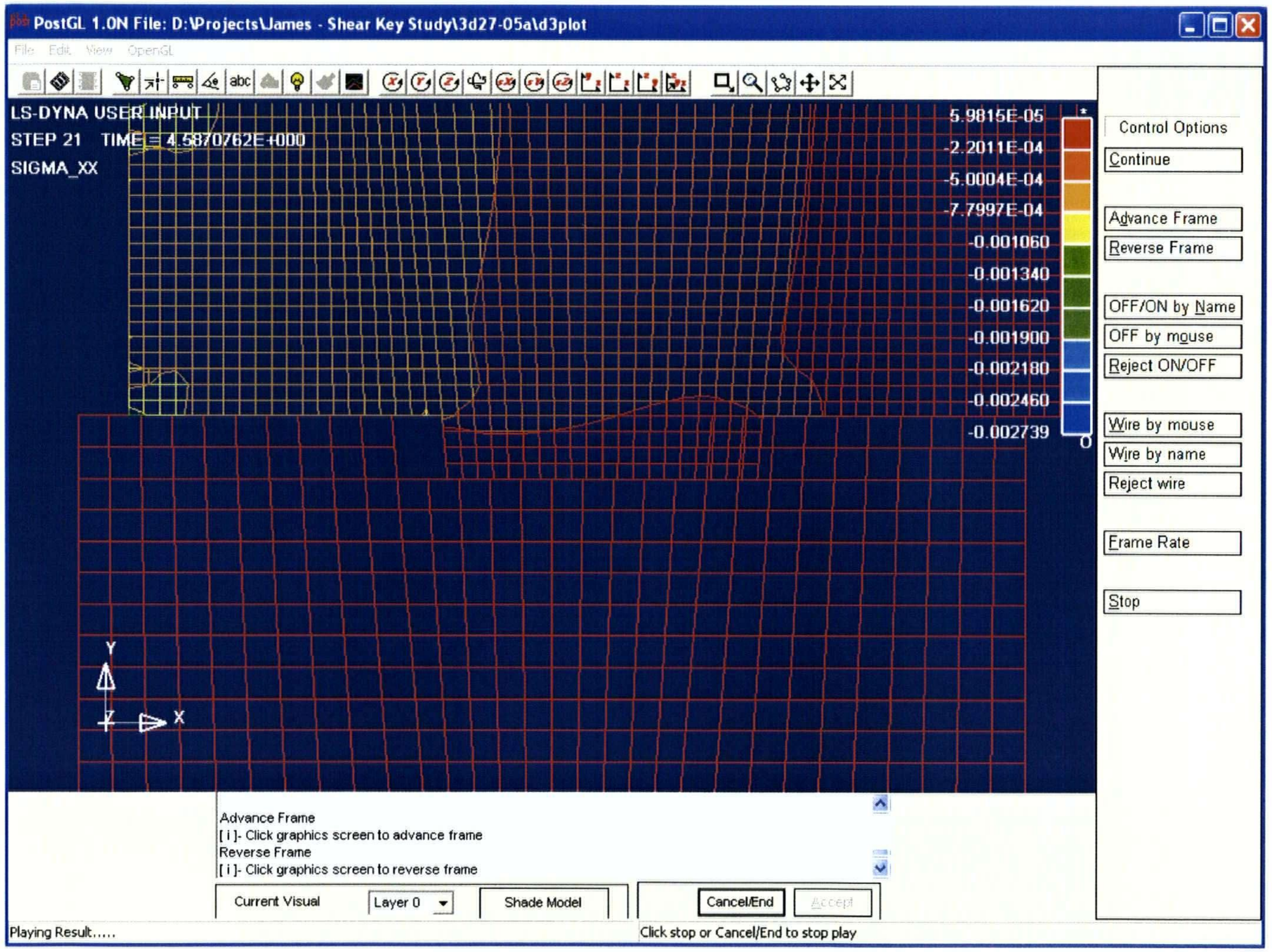

FIGURE 4-8: Model 2, t = 10 s

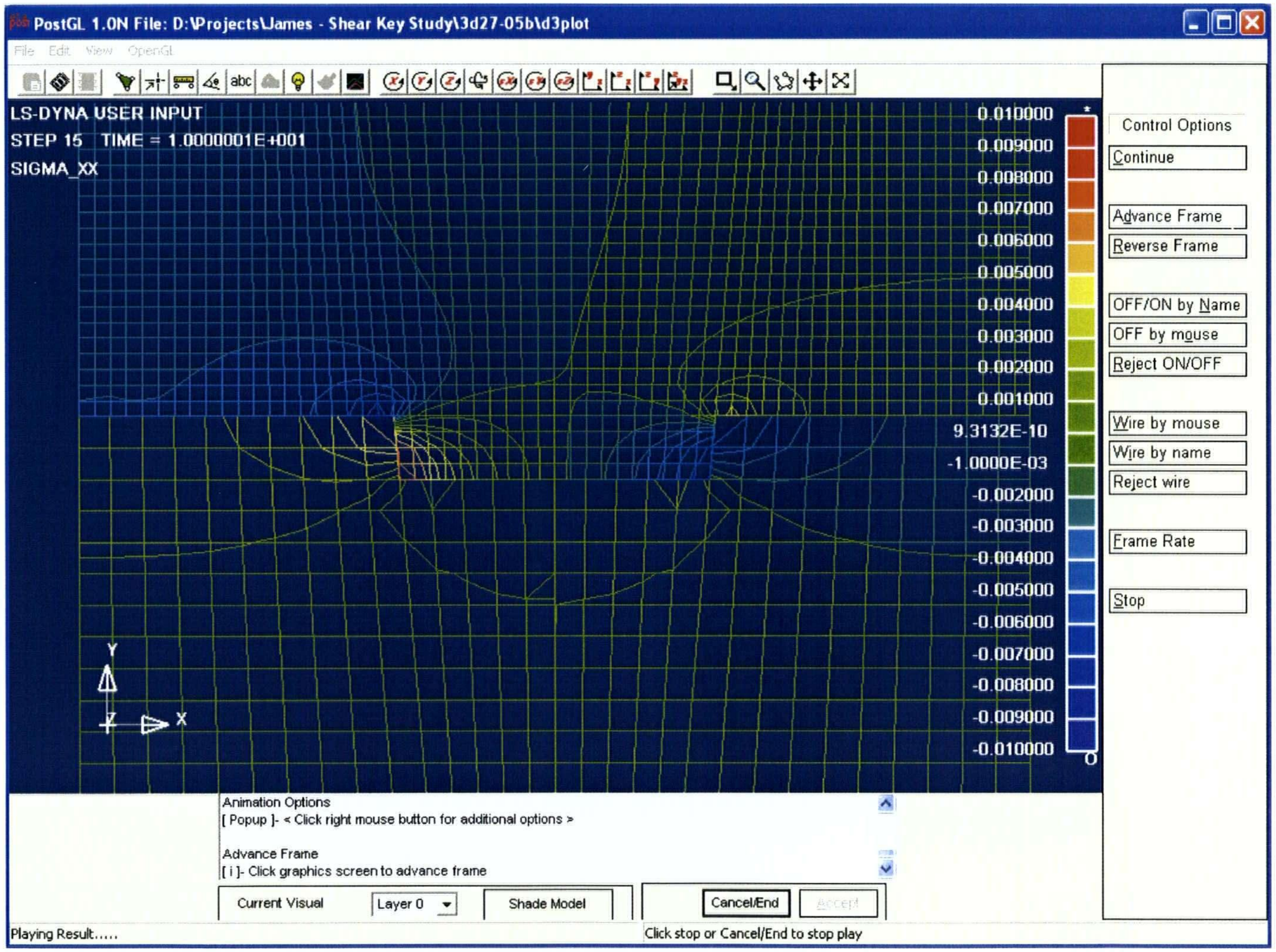

FIGURE 4-9: Model 3, t = 10 s

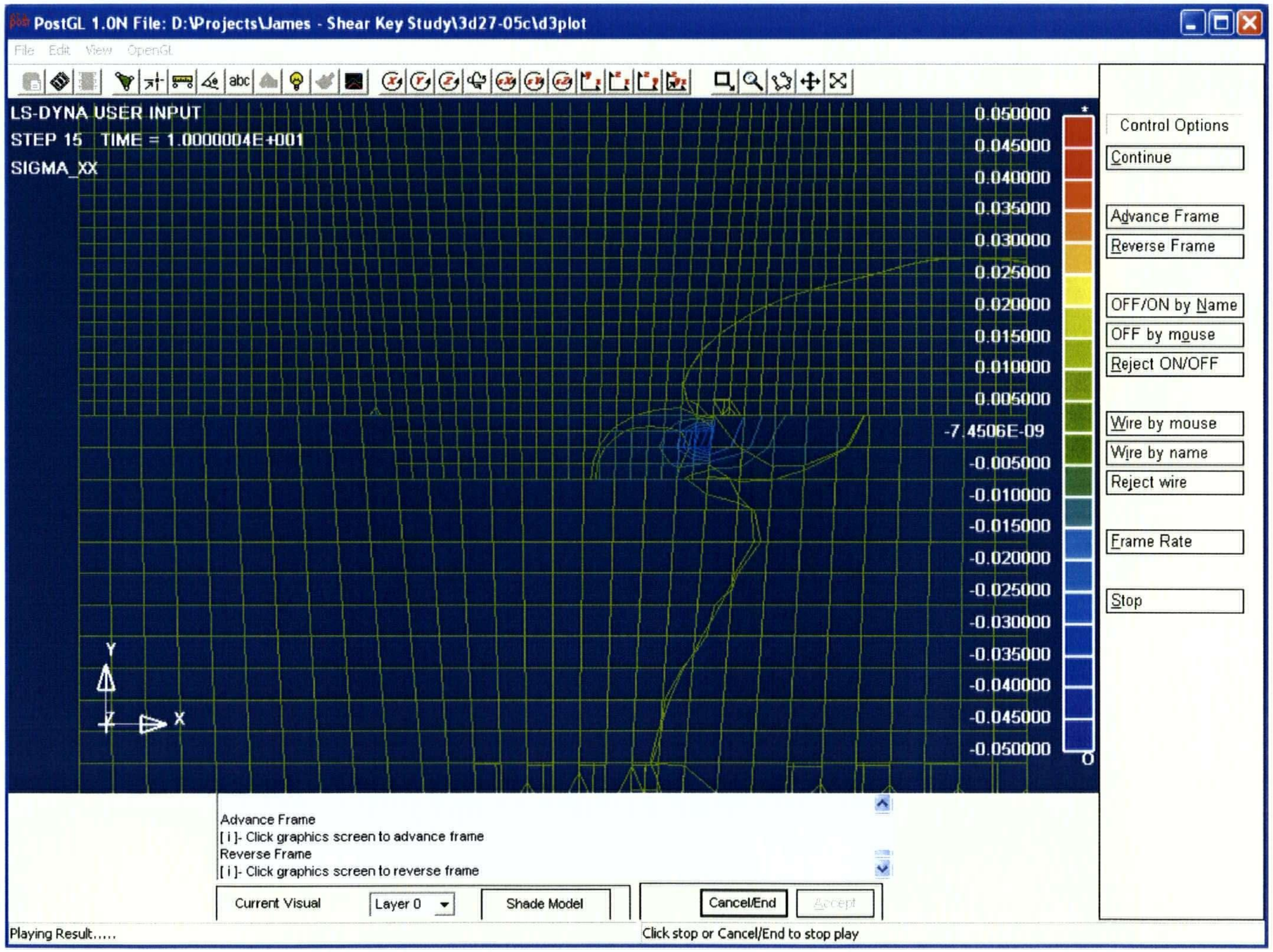

FIGURE 4-10a: Model 4, t = 0 s

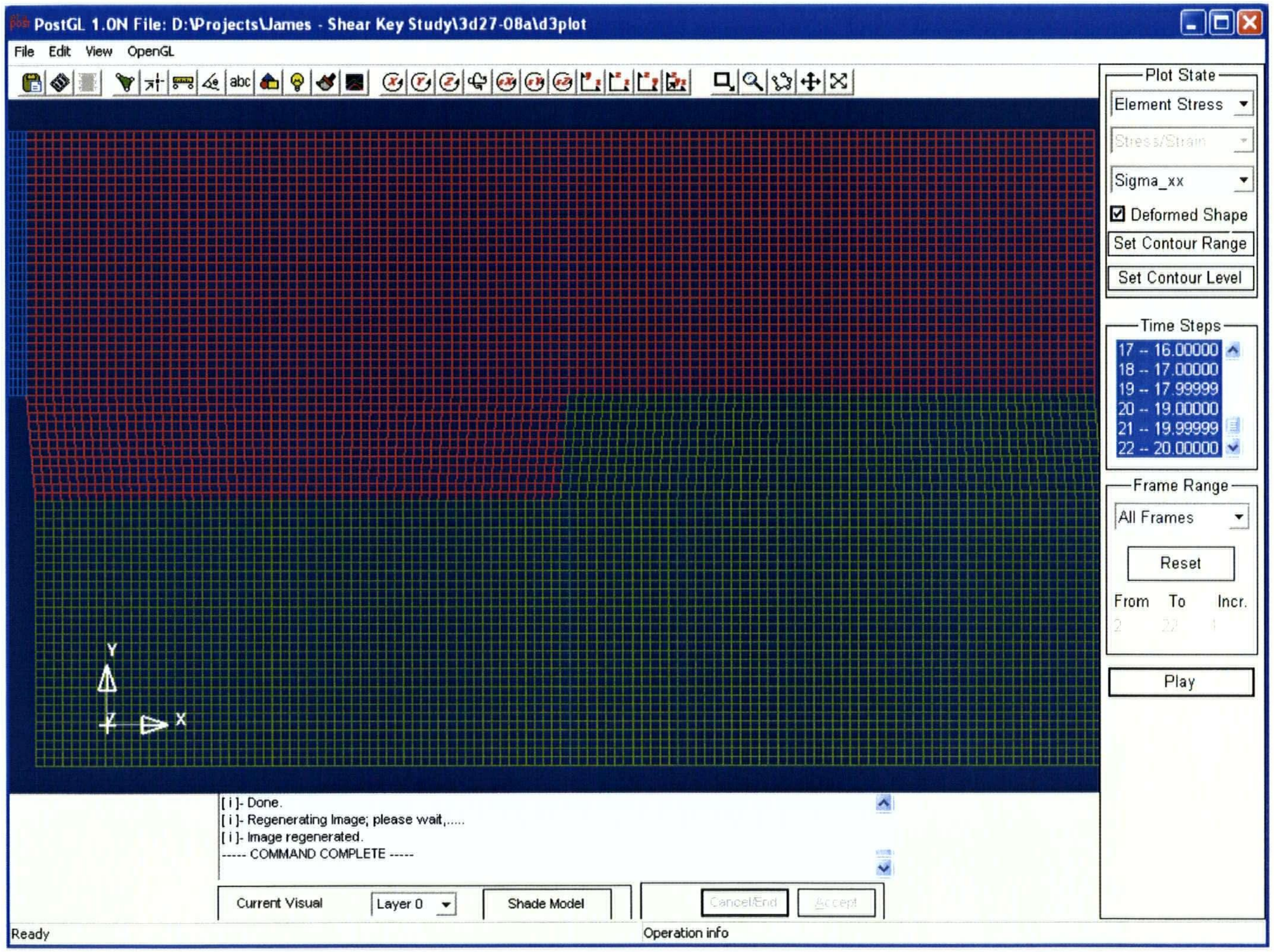

FIGURE 4-10b: Model 4, t = 10 s

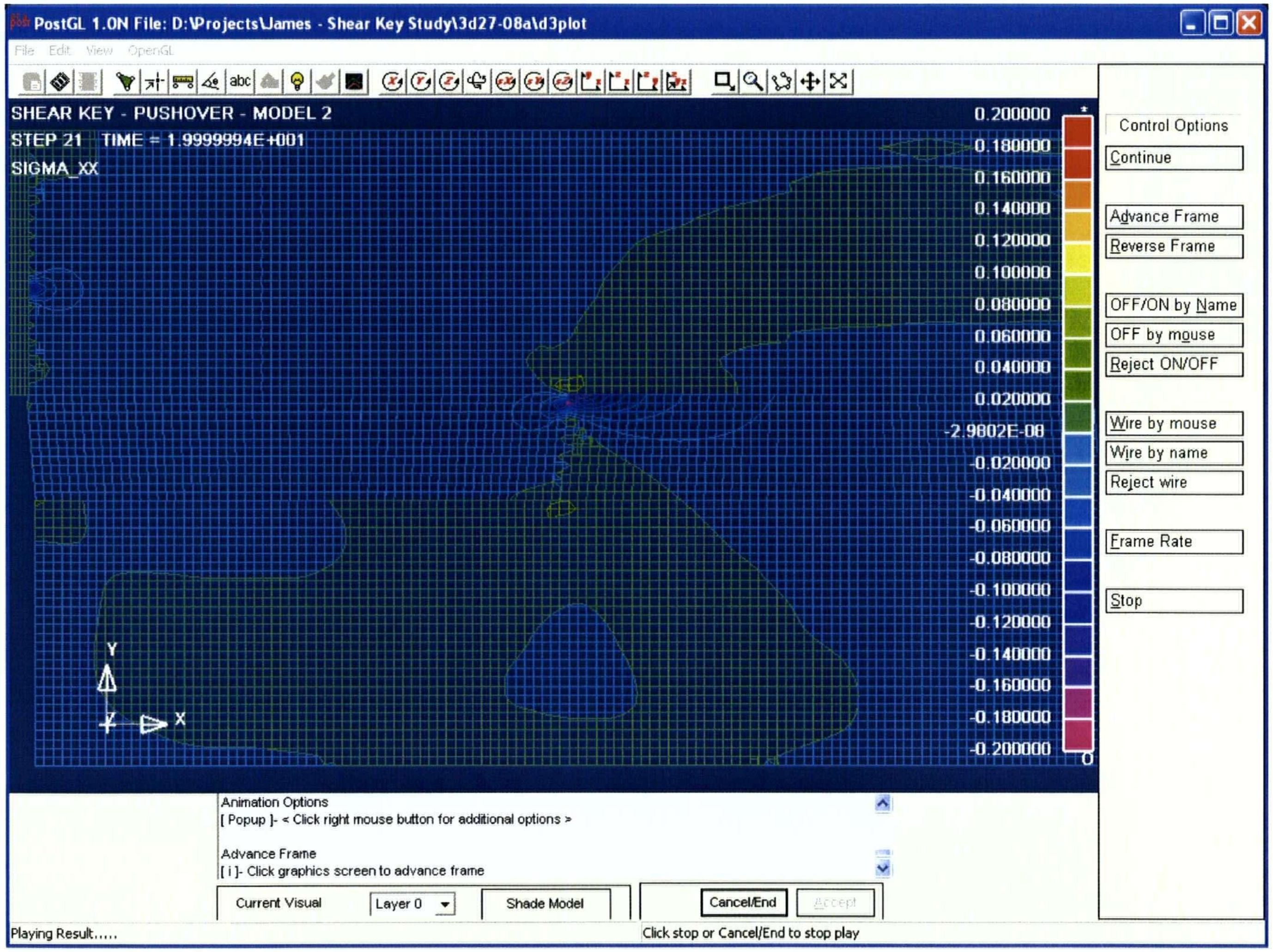

FIGURE 4-11a: Model 5, t = 0 s

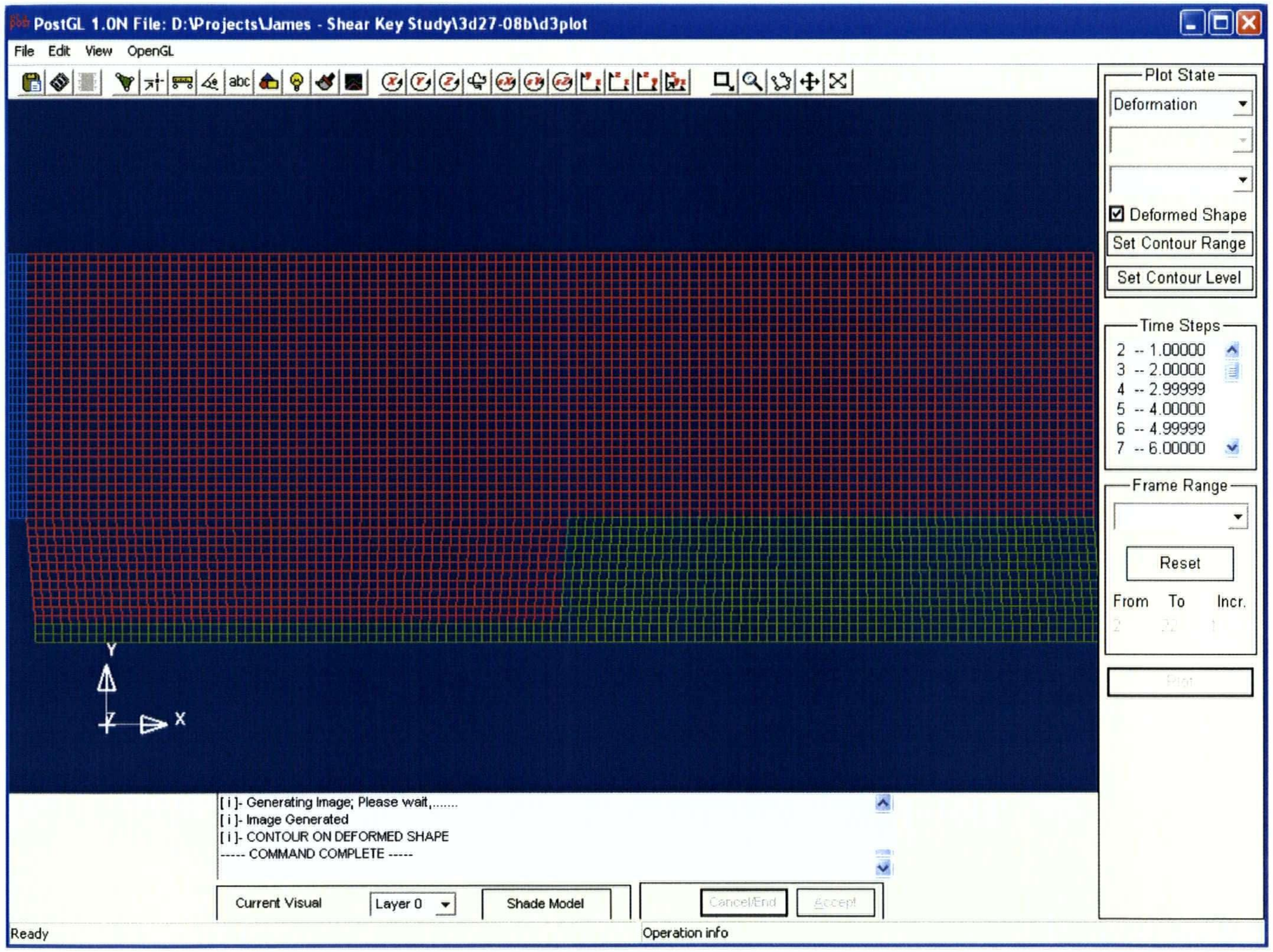

FIGURE 4-11b: Model 5, t = 10 s

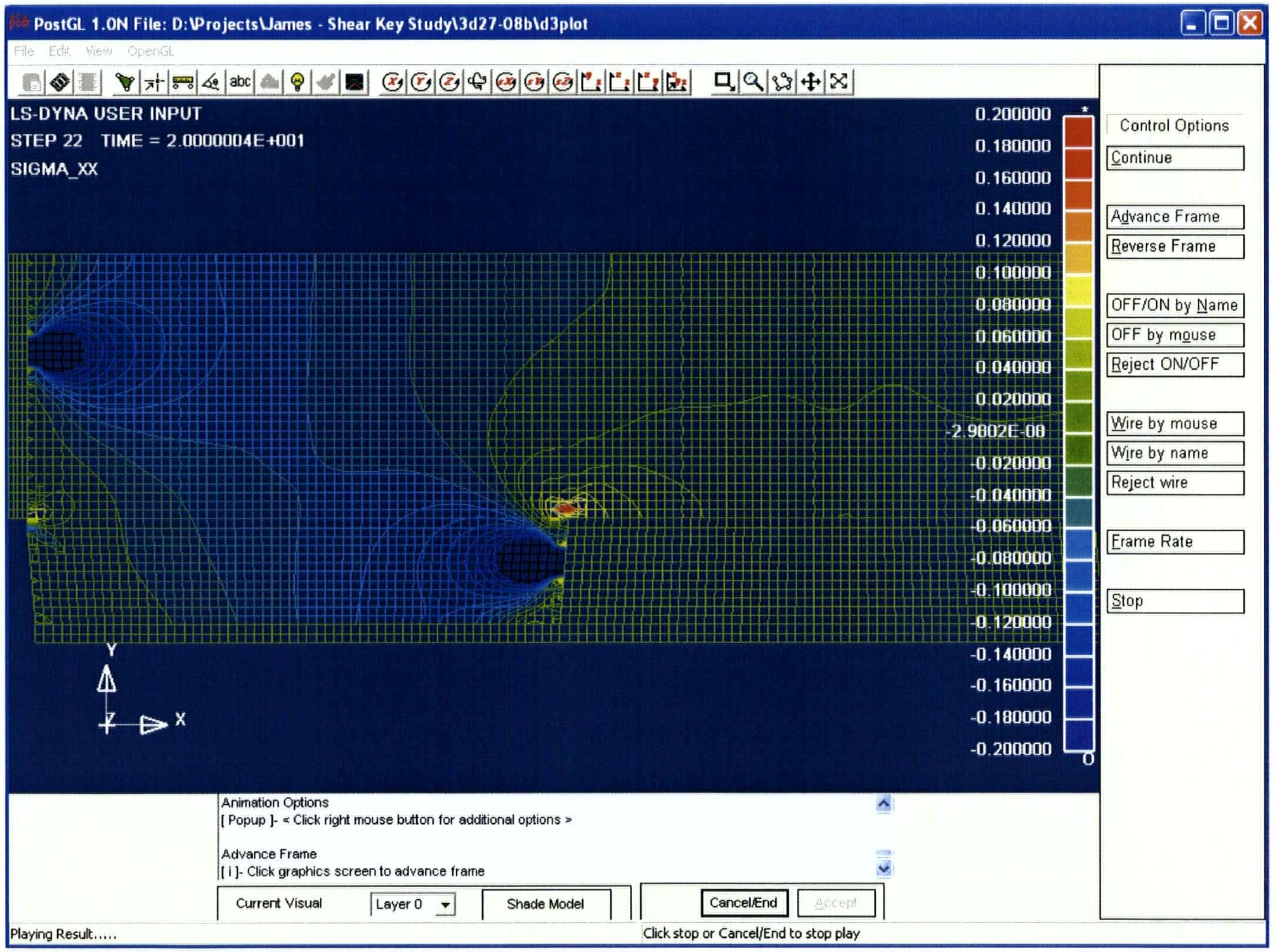

FIGURE 4-12: Model 6, t = 20 s

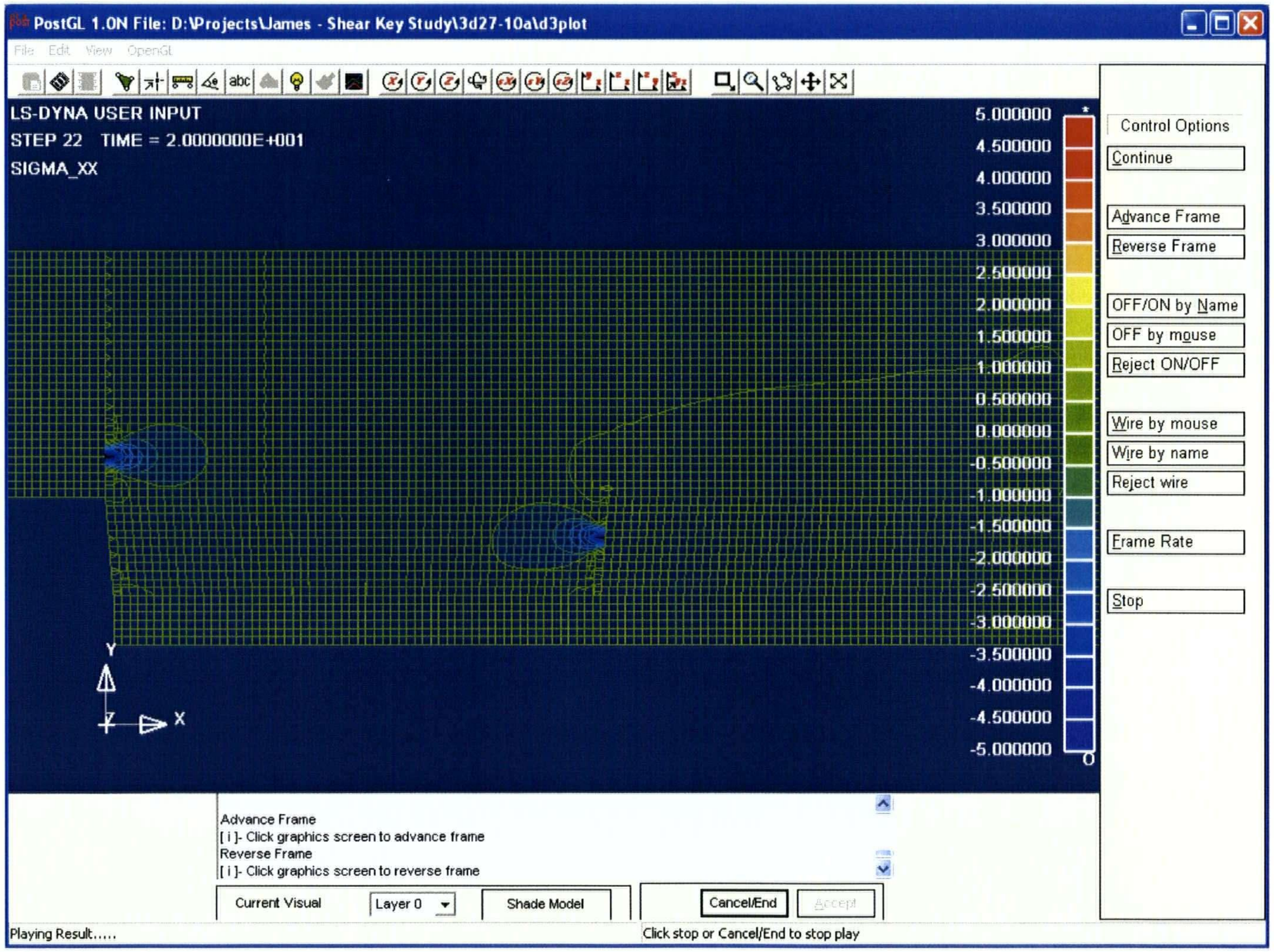

FIGURE 4-13a: Model 7, t = 5 s

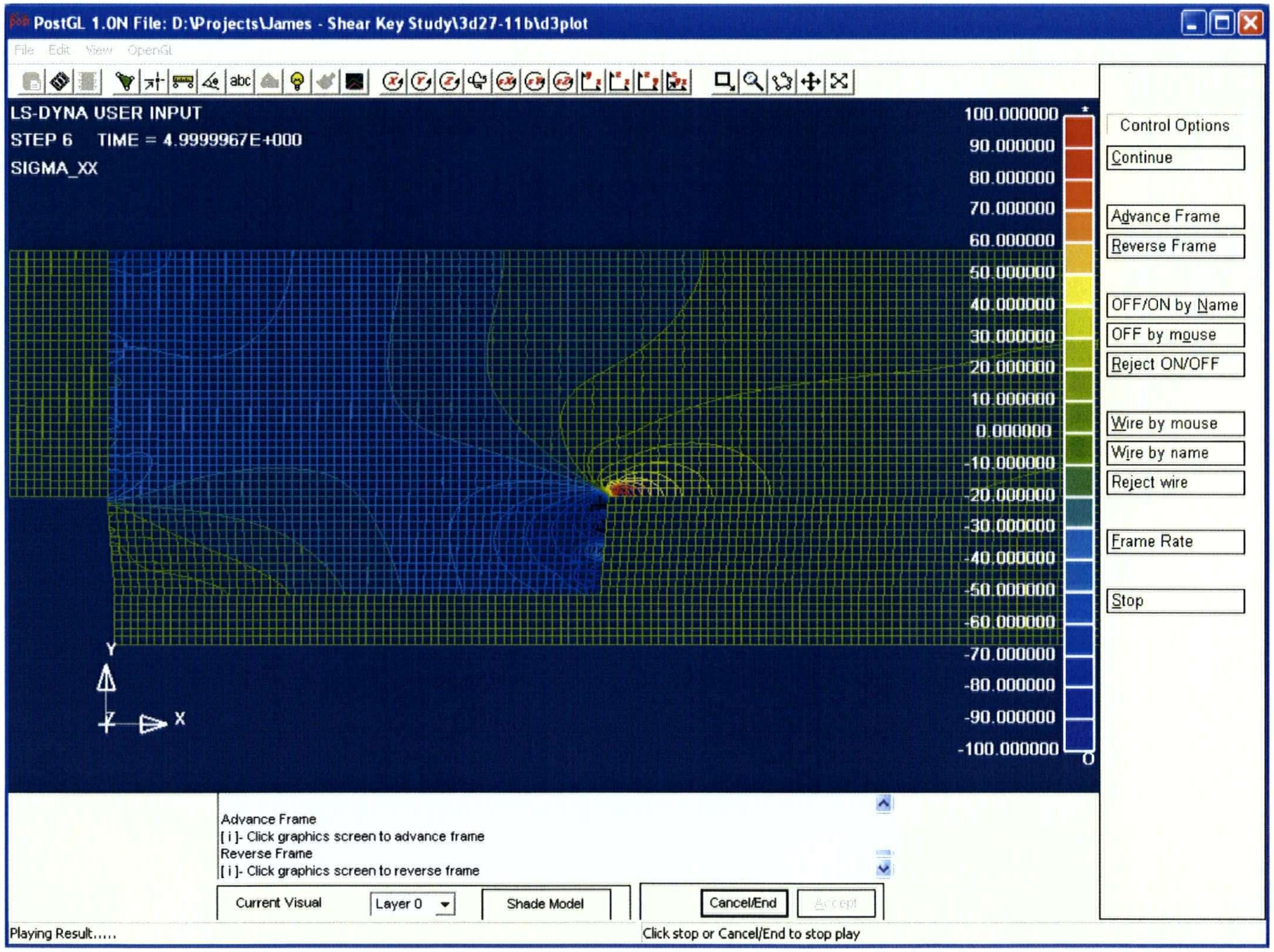

FIGURE 4-13b: Model 7, t = 6 s

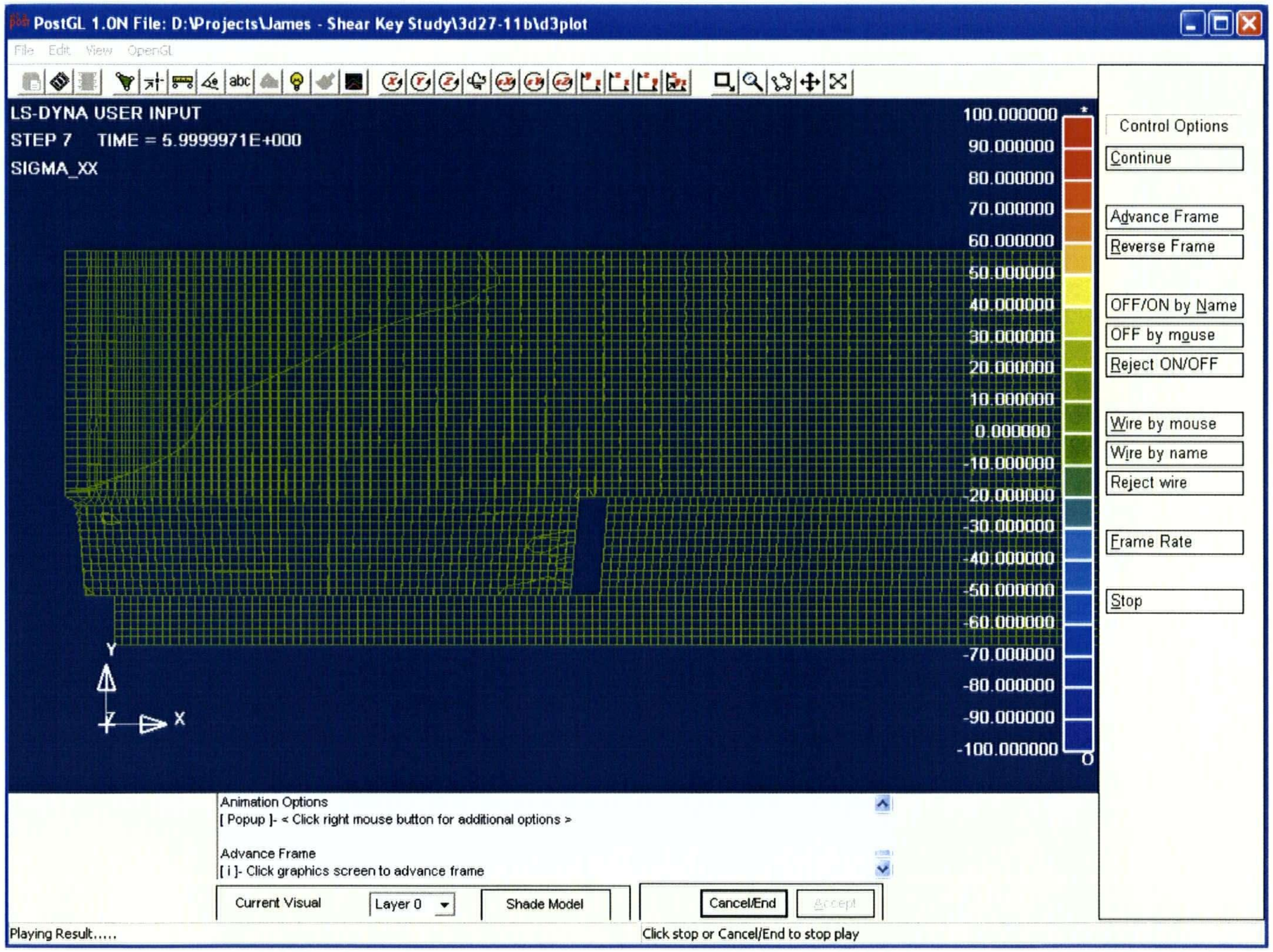

FIGURE 4-14a: Model 8, t = 10 s

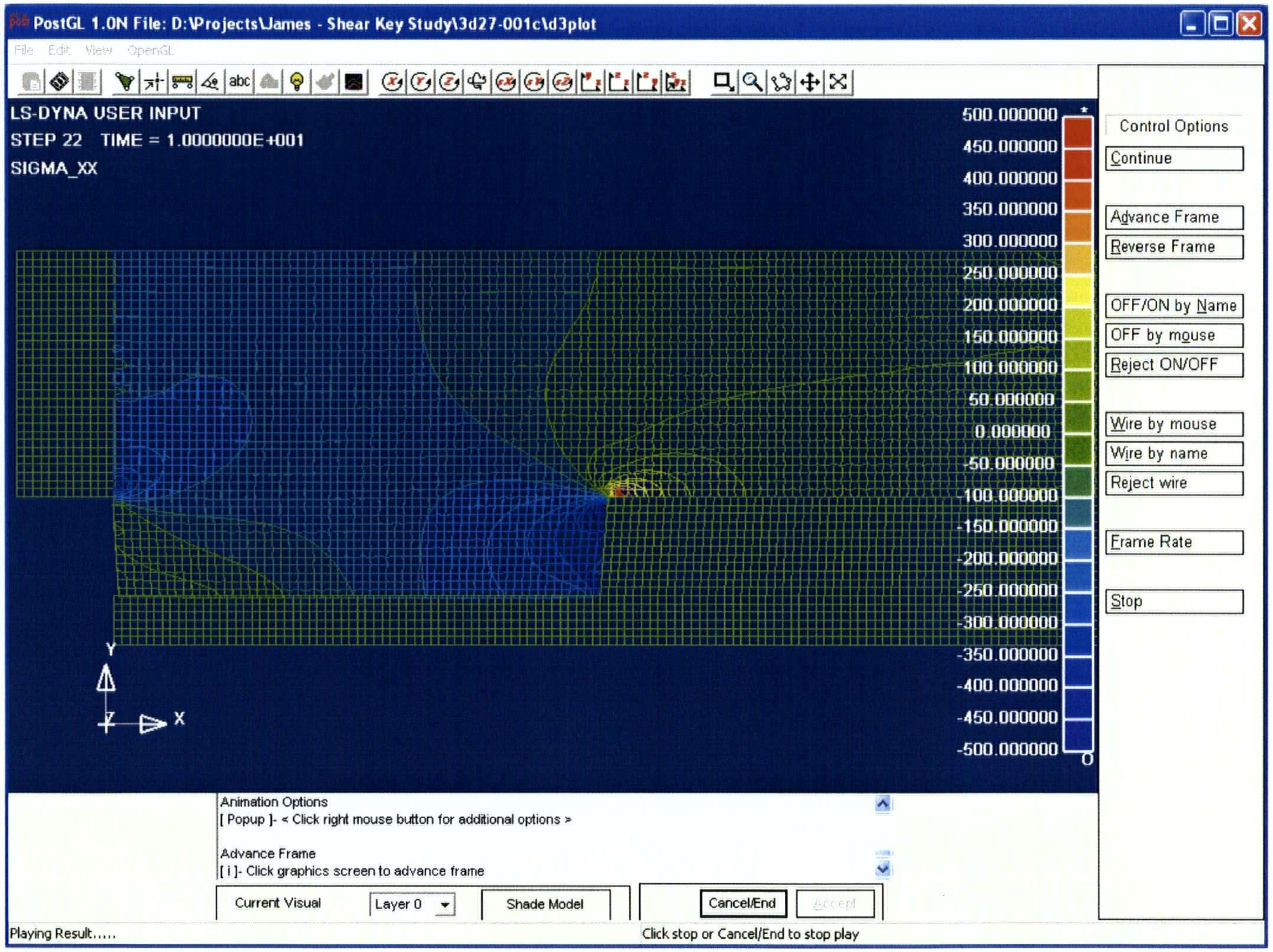

FIGURE 4-14b: Model 8 at Location of Stress Concentration, t = 10 s

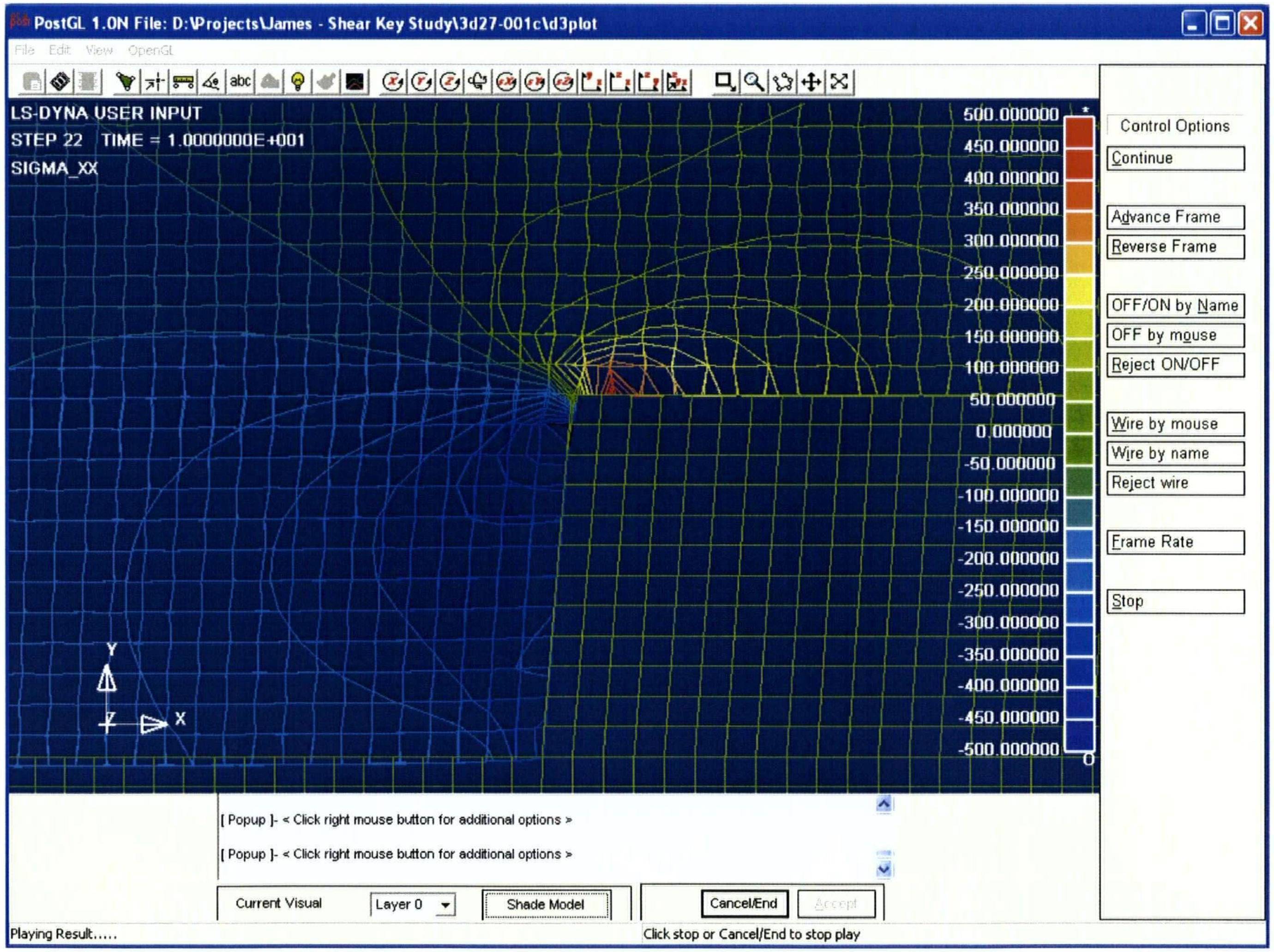

FIGURE 4-15: Model 9, t = 1.5 s

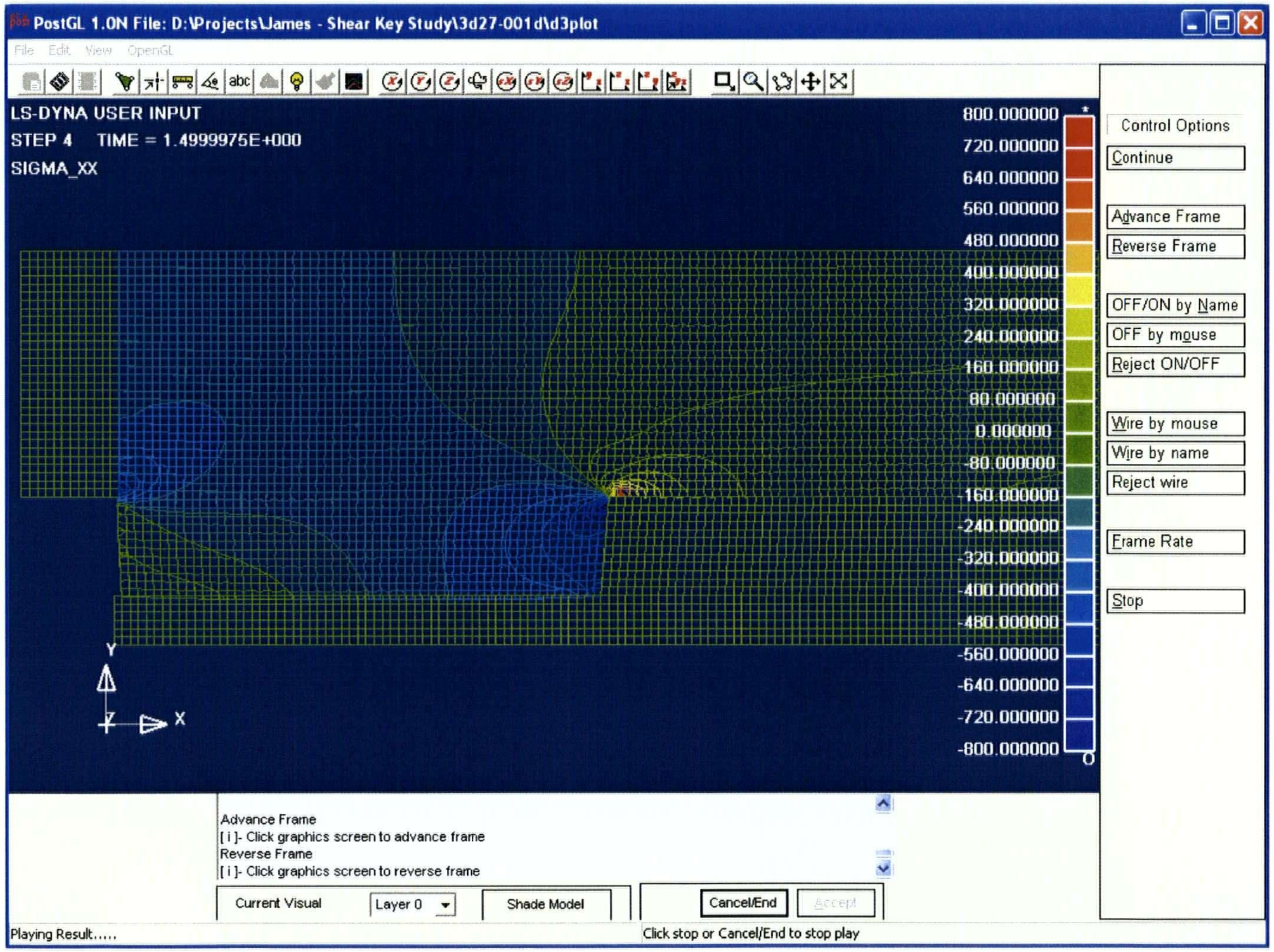

FIGURE 4-16a: Model 10, t = 8.5 s

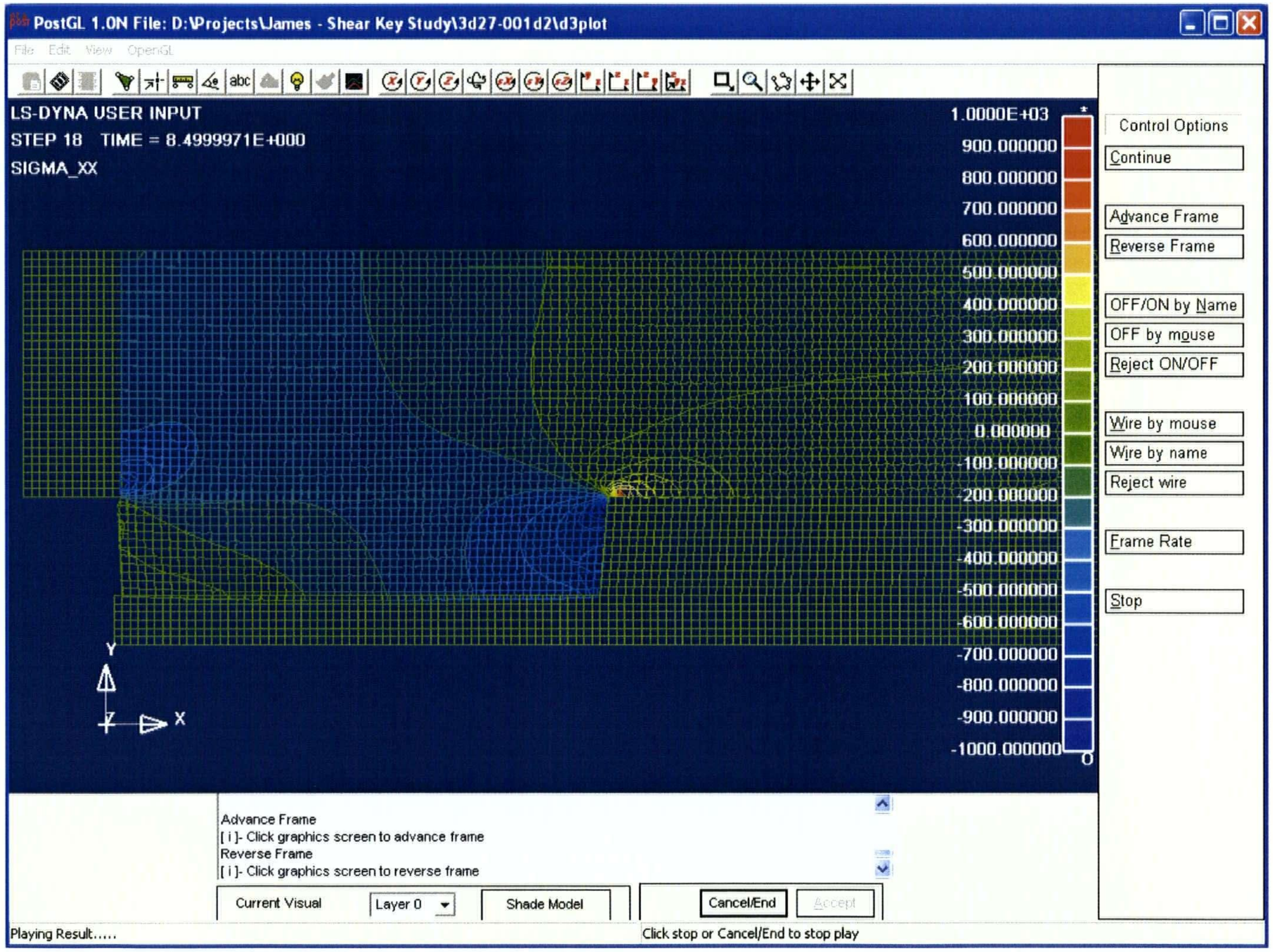

FIGURE 4-16b: Model 10 at Location of Stress Concentration, t = 8.5 s

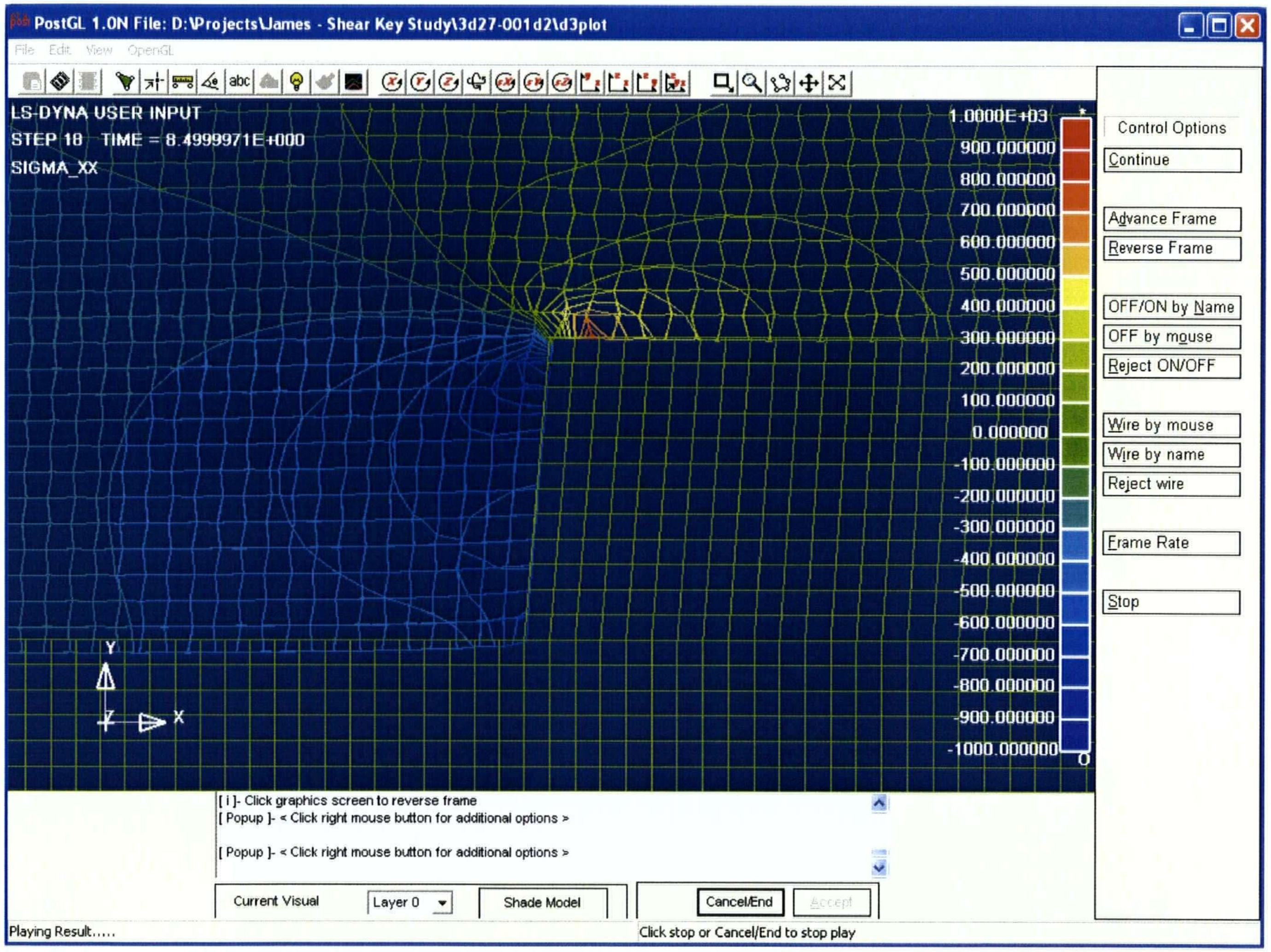

FIGURE 4-17a: Model 11, t = 10 s

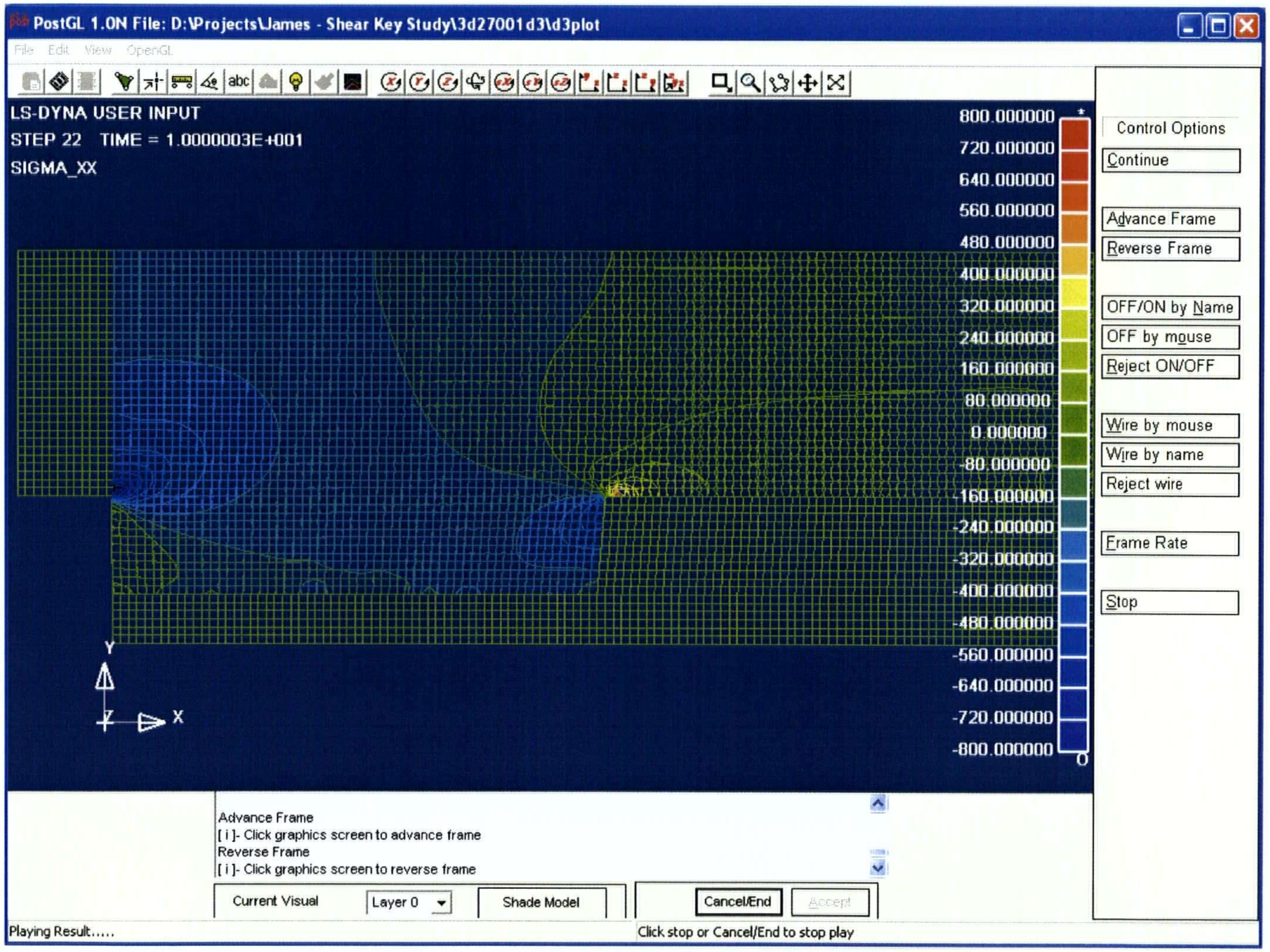

FIGURE 4-17b: Model 11 at Location of Stress Concentration, t = 10 s

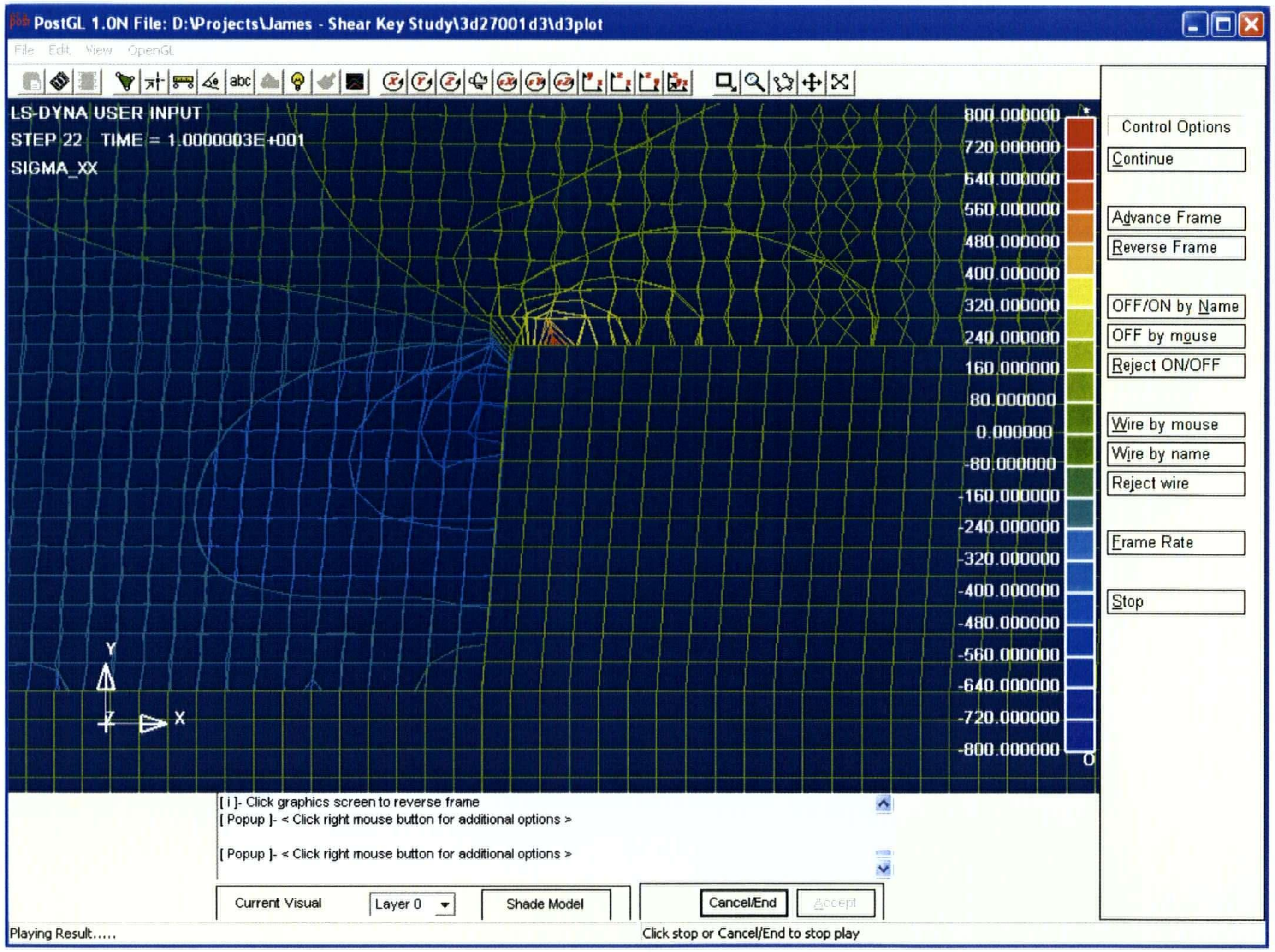

Chapter 5

Conclusions

5.0 CONCLUSIONS

Three independent studies regarding dam safety were presented in this thesis. This chapter presents a summary of the main conclusions from each of these three main studies. More thorough conclusions for each study are presented at the ends of Chapters 2 – 4 of this thesis.

5.1 Dam-Gate Hydrodynamic Interaction Study

A modal analysis of a 2DOF simplified model representing a portion of a gravity dam structure was successfully carried out. The main purposes of this study were to evaluate the effect of dam-gate interaction on the hydrodynamic loads and to evaluate the effect of varying the natural frequency of the gate. The main conclusions from this study are as follows.

- The method presented by Kolkman is useful for considering the dam-gate-reservoir interaction in the formulation of hydrodynamic loads. Conversely, the methods presented by Westergaard and Zangar do not consider the relative response of the gate to the dam. The hydrodynamic loads formulated by the Kolkman method are consistent with those formulated by the Zangar method. This was verified by formulating the hydrodynamic loads for the case of an infinitely rigid dam structure.

- The hydrodynamic load for the extreme gate rigidity case was equal to that computed for the Kolkman Rigid Gate case.
- The peak hydrodynamic load occurred at resonance, when the gate frequency was equal to the dam frequency $(f_g \cong f_d)$.
- As the frequency was shifted towards extreme flexibility, the hydrodynamic load asymptotically approached a value less than that computed for the Kolkman Rigid Gate case.
- For the case of the actual gate frequency $(f_g \cong 7.4Hz)$, the total hydrodynamic load was approximately the average of the Amplified Zangar and the Rigid-Gate Kolkman hydrodynamic loads.
- Most importantly, it is possible to decrease the hydrodynamic loads on the gates by decreasing the natural frequency of the gate to beyond the natural frequency of the dam; ie. by increasing the flexibility of the gate system.

5.2 Damping Study

An analytical study involving the Half-Power Bandwidth method of estimating damping in concrete gravity dams was performed successfully. The objectives of this study were to test this method of evaluating structural damping and to recommend a reasonable estimate of structural damping in concrete gravity dams. The main conclusions from this study are as follows.

- The damping values were found to be much lower than expected (less than 2%) and therefore, unrepresentative of the actual damping present in the concrete gravity dams analyzed in this study.

- The main problem was the identification of natural frequencies, or peaks in the FRF plots, since the only peaks selected for analysis were tall, sharp peaks, representative of components of the structure with little or no damping. Alternatively, the shorter, broader peaks did not extend past the upper envelope of the FRF plots, and therefore were not easily identifiable.

5.3 Shear Key Study

An analytical study involving the finite-element modeling of a shear key system was performed. The main purposes of this study were to examine stress patterns that develop in shear keys under applied loading and to evaluate the structural stability of these shear keys. The main conclusions from this study are as follows.

- The stress patterns that develop in the shear keys under applied horizontal load are reasonable for loading prior to initial propagation of the S-Crack.
- The maximum shear stress on the shear keys subjected to MDE loading is 2.0MPa, which is less than the tensile strength of concrete. If the tensile strength of concrete (about 4.0 - 5.0 MPa) governs the resistance to failure, this provides a safety factor for the shear keys of approximately 2,

provided that the shear stress is distributed evenly across the shear keys at the interface between blocks.

Chapter 6

Recommendations

6.0 RECOMMENDATIONS

This chapter presents a summary of the recommendations from each of these three main studies.

6.1 Dam-Gate Hydrodynamic Interaction Study

1. Analysis using a more detailed full-scale 3-D model of a dam, to account for load sharing between dam blocks and the 3-D effects on the hydrodynamic loads.
2. More detailed computational analysis by means of Finite-Element Analysis software. This would entail an expansion of the 2DOF model to a more complex MDOF model.

6.2 Damping Study

1. Investigation into other methods of calculating or approximating damping for complex structural systems (MDOF).
2. More detailed numerical analysis to allow for easier identification of natural frequencies in the FRF plots. It is possible that a more extensive analytical filtration of the raw data is necessary to allow for acquisition of the desired results.
3. Complementary structural analysis (Finite Element Modeling) to provide

additional verification of the damping formulation methods. This would require creating a 3D model given some initial damping value, applying a ground motion, analyzing the responses of the base and crest locations, plotting the FRF, identifying possible natural frequencies, estimating the damping, and comparing the resulting damping with the damping initially entered in the model.

6.3 Shear Key Study

1. Further investigation into the non-linear and post-cracking behavior of the shear keys, by utilizing some of the more complex material models in the LS-DYNA library. This may also be carried out by introducing cracks into the geometry of the shear key model where cracking is expected to occur for the various stages of the expected cracking pattern.
2. Further investigation into some of the other contact element types available in the LS-DYNA library. One of the potential sources of error in the results was the consistency of the contact surfaces.
3. Expanding the analysis to included cyclic loading and earthquake loading.
4. Use of another finite-element software program to provide alternative results for comparison purposes.
5. Realization of a physical experiment to complement the analytical results.

References

LITERATURE

1. Aslam, M., Wilson, E., Button, M., Ahlgren, C., "Earthquake Analysis of Radial Gates/Dam Including Fluid-Structure Interaction", Third US-Japan Workshop on Advanced Research on Earthquake Engineering for Dams, 2002. pp. 311-323.

2. Bakhoum, M. M., "Shear Behavior and Design of Joints in Precast Concrete Segmental Bridges", PhD Thesis, Massachusetts Institute of Technology, Cambridge, Mass. 1991.

3. Bakhtavar, M.S., "Seismic Behavior and Computer Modeling of Low-Rise Steel Frame Structures", MASc Thesis, The University of British Columbia, 2000.

4. Chopra, A. K., "Dynamics of Structures: Theory and Application to Earthquake Engineering", Second Edition, Prentice Hall, Upper Saddle River, NJ, 2000.

5. Chopra, A. K., Tan, H., "Simplified Earthquake Analysis of Gated Spillway Monoliths of Concrete Gravity Dams", US Army Corps of

Engineers Structures Laboratory, Waterways Experimental Station, Technical Report SL-89-4, March 1989.

6. Di Paola, M., Zingales, M., "Stochastic Seismic Analysis of Hydrodynamic Pressure in Dam Reservoir Systems", Earthquake Engineering and Structural Dynamics, Vol. 32, 2003. pp. 165-172.

7. Fenves, G., Chopra, A.K., "Simplified Analysis for the Earthquake Resistant Design of Concrete Gravity Dams", Report No. UBC/EERC-85-10, Earthquake Engineering Research Centre, University of California, Berkeley, June 1986.

8. Hall, J.F. 1988. "The dynamic and earthquake behaviour of concrete dams: review of experimental behaviour and observational evidence." Soil Dynamics and Earthquake Engineering, 1988.

9. Heere, R., "Durability of Shotcrete Rehabilitation Treatments of B.C. Hydro Dams", Masters of Applied Science Thesis, 1995. pp. 80-87.

10. Kaneko, Y., et al. (1993). "Fracture mechanics approach for failure of concrete shear key. I: Theory." J. of Eng. Mech., 4, pp. 681-700, ASCE.

11. Kaneko, Y., et al. (1993). "Fracture mechanics approach for failure of concrete shear key. II: Verification." J. of Eng. Mech., 4, pp. 701-719, ASCE.

12. Kolkman, P. A., "A Simple Scheme for Calculating the Added Mass of Hydraulic Gates", Journal of Fluids and Structures Vol. 2, 1988. pp. 339-353.

13. Kuo, J. S., "Fluid-Structure Interactions: Added Mass Computations for Incompressible Fluid", Earthquake Engineering Research Center, No. UCB/EERC-82/09, August 1982.

14. Okamoto, S., "Introduction to Earthquake Engineering", New York; Wiley, 1979.

15. Westergaard, H. M., "Water Pressure on Dams During Earthquakes", Transactions, ASCE, Vol. 98, 1933.

16. Zangar, C. N., "Hydrodynamic Pressures on Dams Due to Horizontal Earthquake Effects", Engineering Monograph No. 11, U.S. Bureau of Reclamation, May 1952.

17. Private Communication with BCHydro

SOFTWARE

S1. LS-DYNA, Keyword User's Manual Version 970, Livermore Software Technology Corporation, 2003.

S2. "The ME'scope", 1998, Operating Manual Version 4.0, Vibrant Technology, Jamestown, CA.

S3. SAP90 Users Manual, Wilson, A., Habibullah, A., Computers & Structures Inc., Berkeley, CA, 1989

Appendix A

2DOF Modal Analysis Worksheet

Figure 2-4 shows the Excel worksheet used to carry out the 2DOF modal analysis calculations. This section will explain the calculations carried out in this worksheet.

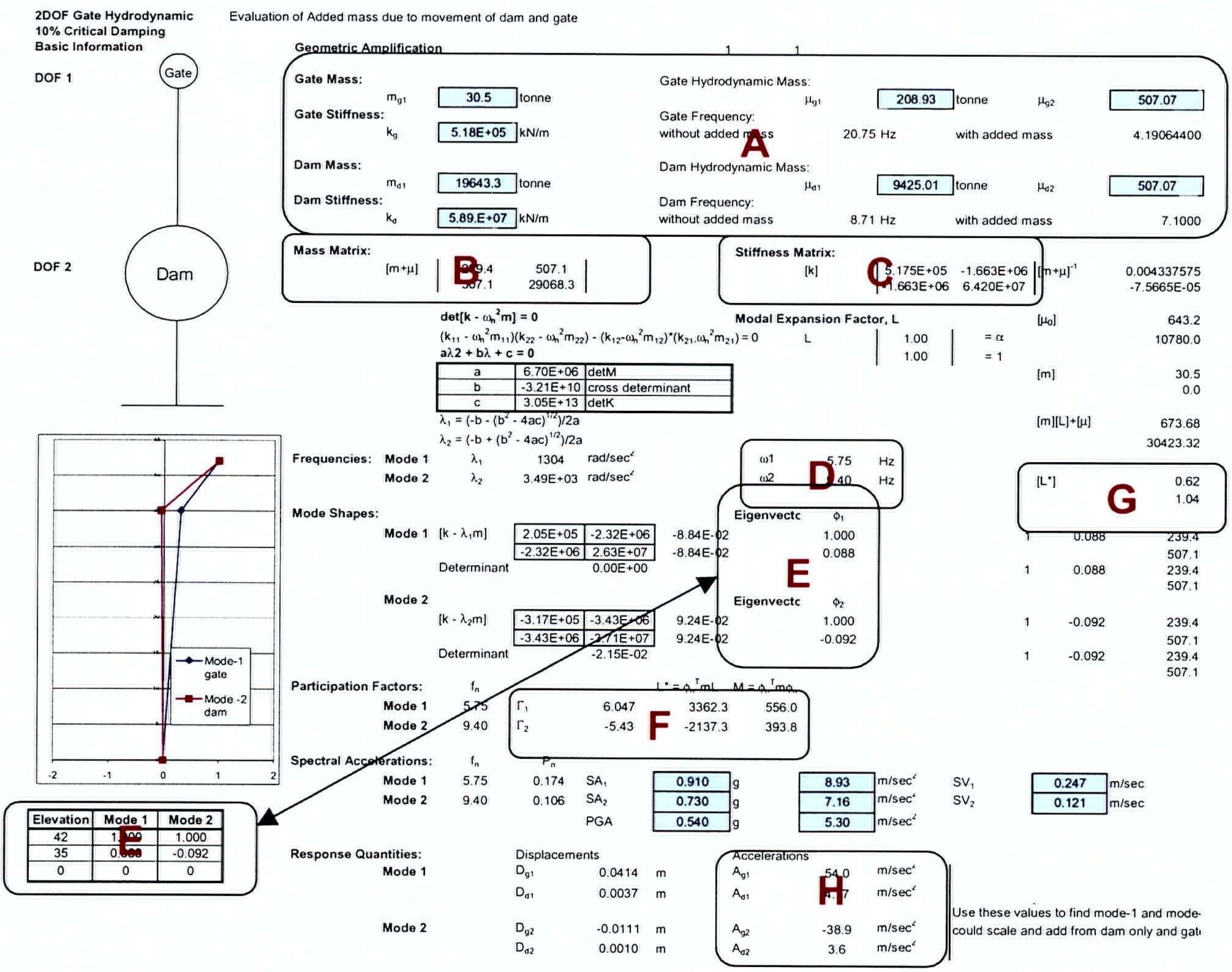

A Defining the Mass and Stiffness Parameters

The first step was to determine the basic mass and stiffness parameters of the dam and gate. The mass of the dam and gate, m_{d1}, m_{g1}, were obtained from structural information of Ruskin Dam. The hydrodynamic added mass terms, μ_{d1}, μ_{d2}, μ_{g1}, μ_{g2}, were determined from the Kolkman spreadsheet, given the acceleration output in part H. The gate stiffness, k_g, was obtained from a complimentary study performed by BCHydro. The dam stiffness, k_d, was calculated as follows, given the dam frequency of 7.1Hz.

$$f_d = \frac{1}{2\pi}\sqrt{\frac{k_d}{m_{d1} + \mu_{d1} + \mu_{d2}}} = 7.1Hz$$

$$k_d = [2\pi(7.1Hz)]^2 (19643 + 9425 + 507) = 58.9 \times 10^6 \, kN/m$$

B Setting up the Mass Matrix

As stated in Section 2.2.2.5, the mass matrix used in the 2DOF modal analysis, $[m*]$, consists of a structural mass component, $[m]$, and a hydrodynamic mass component, $[\mu]$. The composite mass matrix consistent with the worksheet has the form:

$$m* = \begin{bmatrix} m_g & 0 \\ 0 & \alpha^2 \tilde{m}_d \end{bmatrix} + \begin{bmatrix} \mu_{g2} & \mu_{d2} \\ \mu_{g1} & \mu_{d1} \end{bmatrix} = \begin{bmatrix} m_g + \mu_{g2} & \mu_{d2} \\ \mu_{g1} & \alpha^2 \tilde{m}_d + \mu_{d1} \end{bmatrix}$$

C Setting up the Stiffness Matrix

As stated in Section 2.2.2.5, the stiffness matrix used in the 2DOF modal analysis, $[k*]$, has the form:

$$k = \begin{bmatrix} k_g & -\alpha k_g \\ -\alpha k_g & \alpha^2 \tilde{k}_d * \end{bmatrix}$$

D Determining the Natural Frequencies

Given the mass and stiffness matrices, the next step is to solve the characteristic equation of the system.

$$\det[[k]-[\lambda][m*]]=0 \qquad (2-27)$$

Solve the eigenvalues, λ_1 and λ_2, which can be used to calculate the natural frequencies for the two modes of the system.

$$\omega_1 = \frac{\sqrt{\lambda_1}}{2\pi}$$

$$\omega_2 = \frac{\sqrt{\lambda_2}}{2\pi}$$

E Determining the Natural Frequencies

Replace the eigenvalues, λ_1 and λ_2, back into the formal solution to solve the eigenvectors:

$$[[k]-\lambda_1[m*]]\phi_1 = 0 \qquad (2-28a)$$

$$[[k]-\lambda_2[m*]]\phi_2 = 0 \qquad (2-28b)$$

Where ϕ_1 and ϕ_2 are the eigenvectors representing the mode shapes for modes 1 and 2, respectively.

F Determining the Participation Factors

Given the eigenvectors, the next step is to calculate the modal participation factors:

$$\Gamma_1 = \frac{\phi_1^T m * L *}{\phi_1^T m * \phi_1} \qquad (2-29a)$$

$$\Gamma_2 = \frac{\phi_2^T m * L *}{\phi_2^T m * \phi_2} \qquad (2-29b)$$

G Determining the Modal Expansion Factor

The calculation of the new modal expansion factor is explained in Section 2.2.2.5.

Given the equation of motion for the basic mass matrix,

$$[m][\ddot{u}] + [k][u] = -[m][L]\ddot{u}_0 - F_{ext} \qquad (2-23b)$$

The next step is to formulate an equation of motion for the composite mass matrix, $[m*]$

$$[m*][\ddot{u}] + [k][u] = -[m*][L*]\ddot{u}_0 \qquad (2-29)$$

Where:

$$[m*][L*] = [m][L] + \begin{bmatrix} \int P_0 \psi_1 dz \\ \int P_0 \psi_2 dz \end{bmatrix} \xrightarrow{solving} [L*] = [m*]^{-1}\left[[m][L] + \begin{bmatrix} \mu_{01} \\ \mu_{02} \end{bmatrix}\right] \qquad (2-30)$$

H Calculating the Output Accelerations

Then, given the spectral accelerations from the UHRS, the modal accelerations for the two degrees of freedom can be computed:

$$[A_1] = SA_1 \Gamma_1 [\phi_1] \qquad (2-30a)$$

$$[A_2] = SA_2 \Gamma_2 [\phi_2] \qquad (2-30b)$$

Appendix B

MathCAD Numerical Analysis Worksheet

Frequency Domain Analysis of Dam Records (Accelerations)

Description of Test Article Record: DTA := "Detroit Dam, Oregon - 1993 Scotts Mill - USDS"

Description of this dataset: header := "Detroit Dam, Oregon - 1993 Scotts Mill - Acceleration Data"

Define dataset of ambient vibration records to be processed: Data Units: data_units := "milli-Volts"

Directory of files: dir := ""

Sub-directories: test := "\rtf files\"

Name of file with test data : DATA := "detroit dam - 93sm - acc"

Test Data File: TDF := concat(dir, concat(test, concat(DATA, ".rtf")))

Verify path and filename:

TDF = "\rtf files\detroit dam - 93sm - acc.rtf"

Output Data File: ODF := concat(dir, concat(test, concat(DATA, "sc.prn")))

Read file and get size of array in the file and set time increment: AVD := READPRN(TDF)

Sampling rate used: sr := 200 which corresponds to: $\Delta := sr^{-1}$ ==> $\Delta = 0.005$

Nr := rows(AVD) ==> Total number of points: Nr = 6309

C := cols(AVD) ==> Total number of channels: C = 9

$j := 0..C-1$ $i := 0..Nr-1$

The duration of each record is: $T := \Delta\cdot(Nr-1)$ which gives $T = 31.54$

Find largest value recorded: $Colm_j := \max\left(\overrightarrow{\left|AVD^{\langle j\rangle}\right|}\right)$ ==> max(Colm) = 161

Column with Base Displacement: bac := 6

Store record and remove linear trends: $BA := \text{detrend}\left(AVD^{\langle bac\rangle}\right)$

Column with Remote Displacement: rac := 3

Store record and remove linear trends: $RA := \text{detrend}\left(AVD^{\langle rac\rangle}\right)$

Display the entire records:

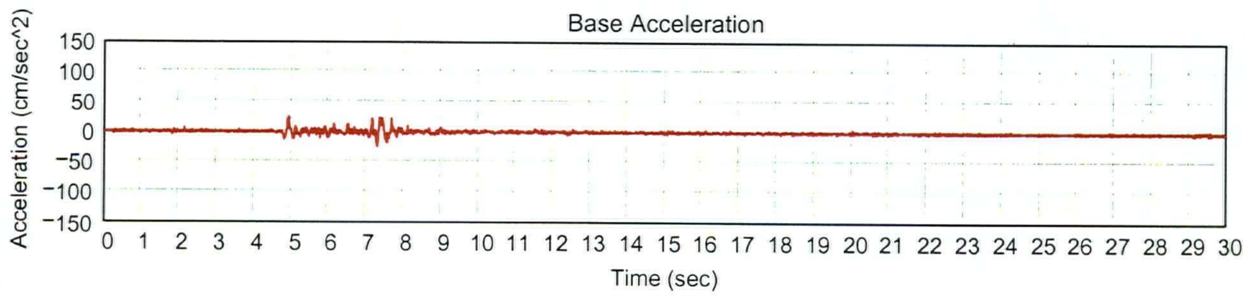

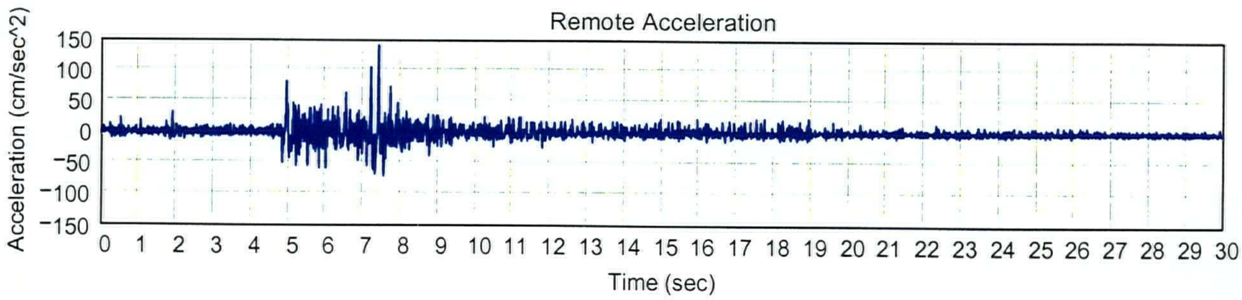

Date: 02/06/2005

Select portion of records that will be processed:

Starting Time of Interval: $T1 := 0$ Ending Time of Interval: $T2 := T$

$Ts := T2 - T1 \qquad N1 := \frac{Ts}{\Delta} + 1 \quad ==> \quad N1 = 6309 \qquad r := 0 .. N1 - 1$

Extract Segments from Records and remove linear trends: $N0 := \frac{T1}{\Delta} \quad ==> \quad N0 = 0$

$BAS_r := BA_{r+N0}$ $BAS := \mathrm{detrend}(BAS)$ and $RAS_r := RA_{r+N0}$ $RAS := \mathrm{detrend}(RAS)$

which have a duration of $Ts = 31.54$

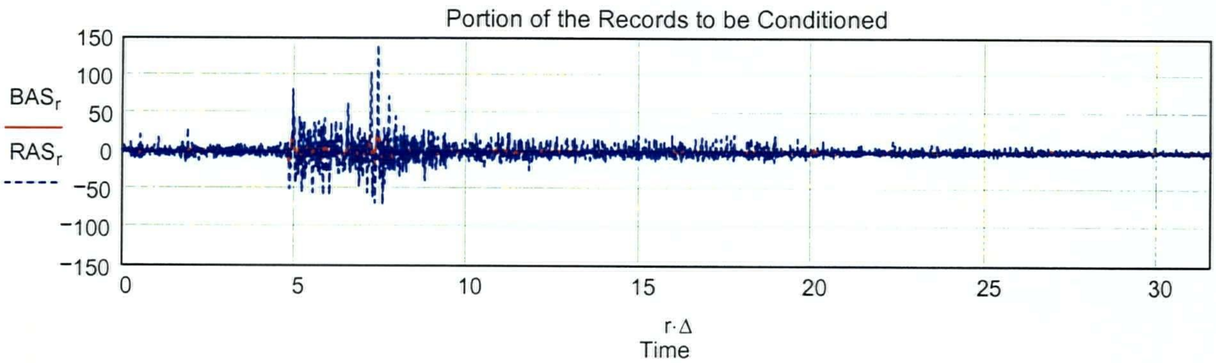

Compute Power Spectrum for each signal and display it:

No. of overlapping segments (>2): $nos := 2$ Overlapping factor (0<of<1): $of := .99$ Smooth factor: $sm := 1$

$PSBA := \mathrm{movavg}(\mathrm{pspectrum}(BAS, nos, of), sm) \qquad PSRA := \mathrm{movavg}(\mathrm{pspectrum}(RAS, nos, of), sm)$

$\mathrm{length}(PSBA) = 6245 \qquad k := 0 .. 0.50 \cdot \mathrm{length}(PSBA) \qquad \Delta f := [(\mathrm{length}(PSBA) - 1) \cdot \Delta]^{-1}$

$\Delta f = 0.032031$

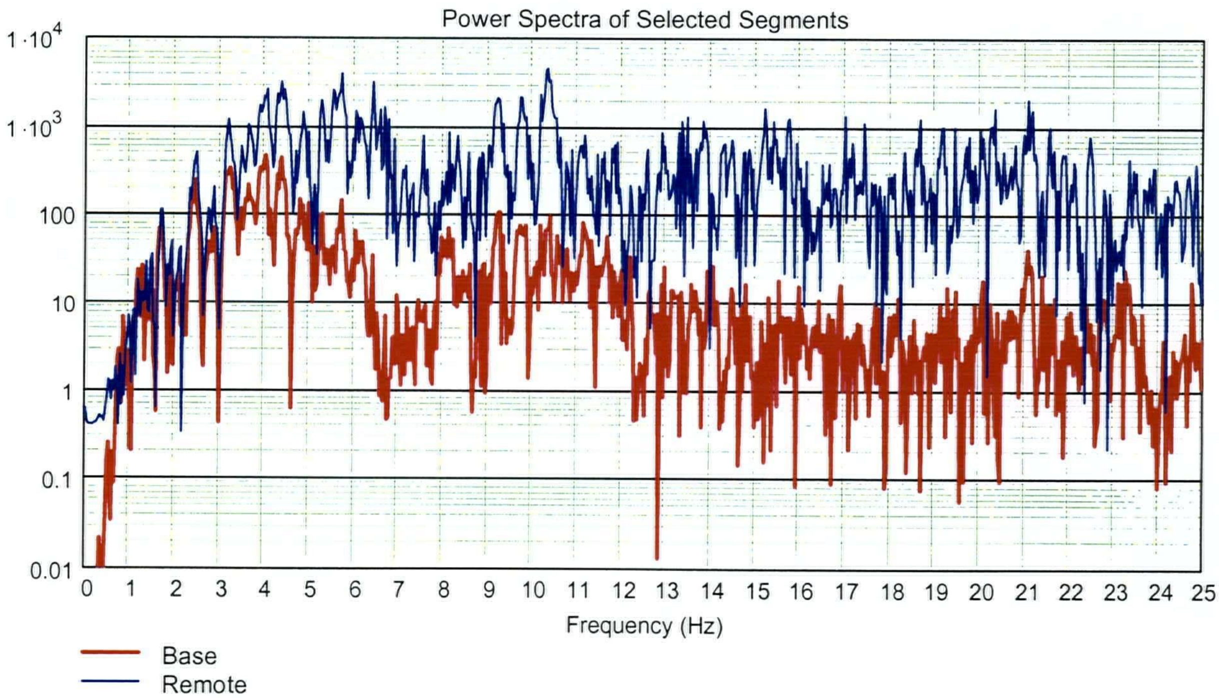

Set bandpass filter:

We'll use a bandpass filter with NB coefficients, designed with a Hanning window, and select the right cutoff frequencies.

Choose a window: setwindow(4) = 4 (this is a Hanning window) Choose the number of coefficients: NB := 40

Choose low-frequency cutoff: FL := .01 ==> f1 := FL·Δ Choose high-frequency cutoff: FH := 25 ==> f2 := FH·Δ

Find FIR filter coefficients fir := bandpass(f1 , f2 , NB)

Filter the quantized signals using the response function, then compute their PS:

BASf := response(BAS , fir , N1) and PSBAf := movavg(pspectrum(BASf , nos , of) , sm)

RASf := response(RAS , fir , N1) and PSRAf := movavg(pspectrum(RASf , nos , of) , sm)

Plot the filtered and the original signals: $BASf_{N1} := 0$ $(RASf)_{N1} := 0$ length(BASf) = 6310

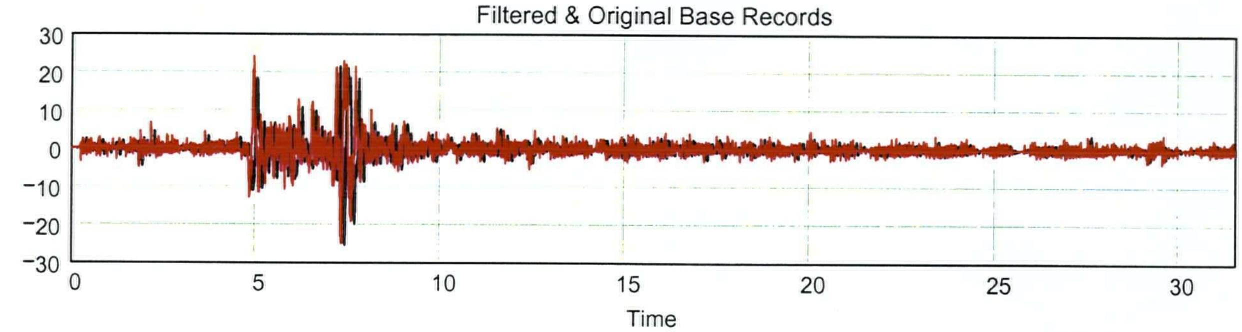

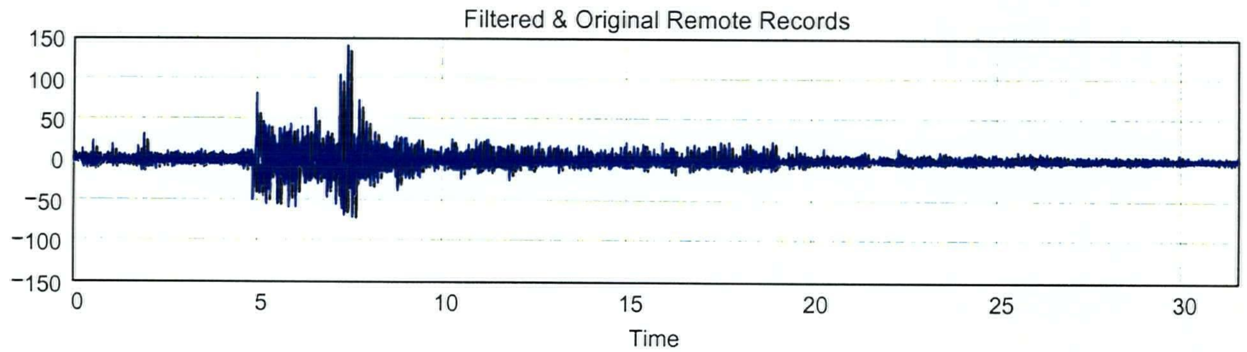

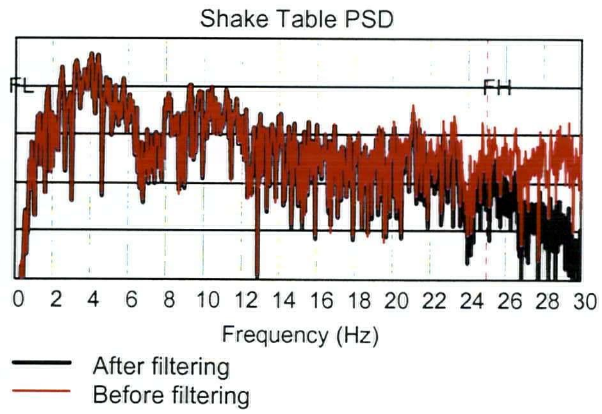

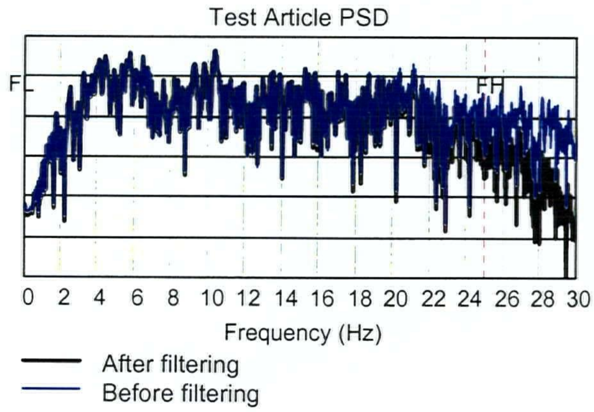

Compute FRF, Phase Angle, Coherence and Cross-Spectrum: X := BASf Y := RASf

Spectral Ratios Subroutine Calculations:

Delete some arrays:

$table := 0$ $PSBAf := 0$
$PSRAf := 0$

Calculate continuous 2-sided Auto Spectra and Cross Spectrum for X and Y:

$Gxx := pspectrum(X, nos, of) \cdot \frac{Ts}{\pi}$ $Gyy := pspectrum(Y, nos, of) \cdot \frac{Ts}{\pi}$ $Gxy := cspectrum(X, Y, nos, of) \cdot \frac{Ts}{\pi}$

Calculate Transfer Function, CHxy, Coherence, COxy, and Phase Angle, ϕ, :

$Hxy := mag\left(\overrightarrow{\frac{Gxy}{Gxx}}\right)$ $Hxy_0 := 0$ $FRF := movavg(Hxy, sm)$ $FRF_0 := 0$

$COHxy := coherence(X, Y, nos, of)$ $CO := movavg(COHxy, sm)$

$PH := phase(Gxy) \cdot \frac{180}{\pi}$ $\phi := movavg(PH, sm)$ $\phi_0 := 0$

$SNR1 := snr(X, Y, nos, of)$ $SN1 := SNR1$ $SN1_0 := 0$ $SNR := movavg(SNR1, sm)$

$XS := movavg\left(mag\left(\overrightarrow{Gxy}\right), sm\right)$

$length(FRF) = 6246$ $j := 0 .. 0.50 \cdot length(FRF)$ $\Delta f := [(length(FRF) - 1) \cdot \Delta]^{-1}$ ==> $\Delta f = 0.032026$

RESULTS FOR ANALYSIS OF DATA FOR:

DTA = "Detroit Dam, Oregon - 1993 Scotts Mill - USDS"

from dataset: TDF = "\rtf files\detroit dam - 93sm - acc.rtf"

Frequency range (in Hz) to be displayed (F0=minimum, FH=maximum): F0 := 0 FH := 10